PROBING PRESSURE-INDUCED STRUCTURAL DYNAMICS IN XENOTIME RARE EARTH ORTHOPHOSPHATES VIA *IN SITU* DIFFRACTION AND SPECTROSCOPY

by

Jai Sharma

A thesis submitted to the Faculty and the Board of Trustees of the Colorado School of Mines in partial fulfillment of the requirements for the degree of Doctor of Philosophy (Materials Science).

Golden, Colorado

Date _____

Signed: _____

Jai Sharma

Signed: _____

Dr. Corinne E. Packard
Thesis Advisor

Golden, Colorado

Date _____

Signed: _____

Dr. Eric Toberer
Professor and Program Head
Materials Science Program

ABSTRACT

Rare earth orthophosphate ($REPO_4$) ceramics have attracted decades-long interest in research fields ranging from geoscience to structural composites to photonics. While these fields have historically been largely separate, their growing convergence brings added relevance to $REPO_4$ phase transformations, the influence of stress state on transformation, and transformation detection methods.

This dissertation employs *in situ* diamond anvil cell (DAC) synchrotron x-ray diffraction (XRD) to shed light on the activation conditions of the xenotime-monazite transformation in $DyPO_4$ and $TbPO_4$. First, the transformation onset pressure (P_{onset}) of $DyPO_4$ (measured under hydrostatic conditions) shows Raman spectroscopy-based P_{onset} values are significant over-estimations, and $REPO_4$ P_{onset} does not decrease linearly with RE ionic radius. Experiments also reveal the shear-sensitivity of this transformation as shear reduces P_{onset} significantly in $TbPO_4$ and $DyPO_4$ and widens the xenotime-monazite phase coexistence range in $TbPO_4$. In addition, XRD indicates a high-pressure, post-monazite phase (likely of the scheelite structure) exists across a wider range of xenotime $REPO_4$s than was previously known. These findings show $REPO_4$ transformation can offer enhanced plasticity and toughening in ceramic matrix composites at lower pressures and over wider pressure ranges than expected. Long phase coexistence pressure ranges across all XRD experiments also point toward this transformation being diffusional rather than martensitic.

This dissertation also shows direct-excitation photoluminescence (PL) spectroscopy can be utilized to detect the xenotime-monazite phase transformation. PL experiments yield $TbPO_4$ transformation onset and end pressures consistent with synchrotron XRD results. In addition, PL spectra of recovered $TbPO_4$ samples can offer insight into stress history, including history of transformation.

TABLE OF CONTENTS

LIST OF FIGURES

LIST OF TABLES

LIST OF SYMBOLS

Final pressure . . . . . P_{final}

Initial pressure . . . . . $P_{initial}$

Monazite β lattice parameter . . . . . β_M

Monazite a lattice parameter . . . . . a_M

Monazite b lattice parameter . . . . . b_M

Monazite c lattice parameter . . . . . c_M

Monazite zero-pressure bulk modulus . . . . . $B_{0,M}$

Monazite zero-pressure volume . . . . . $V_{0,M}$

Pressure . . . . . P

Pressure derivative of bulk modulus . . . . . B'$_0$

Scattering vector magnitude . . . . . Q

Transformation onset pressure . . . . . P_{onset}

Volume V

Wavelength . . . . . λ

Weighted chi square statistic . . . . . χ^2_w

Xenotime a lattice parameter . . . . . a_X

Xenotime c lattice parameter . . . . . c_X

Xenotime zero-pressure bulk modulus . . . . . $B_{0,X}$

Xenotime zero-pressure volume . . . . . $V_{0,X}$

Zero-pressure bulk modulus . . . . . B_0

Zero-pressure volume . . . . . V_0

LIST OF ABBREVIATIONS

1:1:4 stoichiometry with 4 oxygen ions . . . . . ABO_4

Ceramic matrix composite . . . . . CMC

Cerium orthophosphate . . . . . $CePO_4$

Cesium chloride . . . . . CsCl

Diamond anvil cell . . . . . DAC

Dysprosium orthophosphate . . . . . $DyPO_4$

Energy-dispersive x-ray spectroscopy . . . . . EDS

Equation of State . . . . . EOS

Erbium orthophosphate . . . . . $ErPO_4$

Europium earth orthophosphate . . . . . $EuPO_4$

Full width at half-maximum . . . . . FWHM

Gadolinium orthophosphate . . . . . $GdPO_4$

Gold . . . . . Au

High-pressure potassium chloride phase B2-KCl

Holmium orthophosphate . . . . . $HoPO_4$

Infrared . . . . . IR

Lanthanum orthophosphate . . . . . $LaPO_4$

Low-pressure potassium chloride phase B1-KCl

Lutetium orthophosphate . . . . . $LuPO_4$

MEW . . . . . 16:3:1 methanol-ethanol-water mixture

Neodymium earth orthophosphate . . . . . $NdPO_4$

Phosphate . . . . . PO_4

Photoluminescence spectroscopy . . . . . PL

Potassium chloride . . . . . KCl

Praseodymium orthophosphate . . . . . $PrPO_4$

Pressure-transmitting medium . . . . . PTM

Promethium orthophosphate . . . . . $PmPO_4$

Raman spectroscopy . . . . . RS

Rare earth . . . . . RE

Rare earth orthophosphate . . . . . $REPO_4$

Samarium orthophosphate . . . . . $SmPO_4$

Scandium orthophosphate . . . . . $ScPO_4$

Scanning electron microscopy . . . . . SEM

Scheelite-type phase of terbium orthophosphate . . . . . $S(TbPO_4)$

Terbium orthophosphate . . . . . $TbPO_4$

Thulium orthophosphate . . . . . $TmPO_4$

Transmission electron microscopy . . . . . TEM

Trivalent rare earth ion . . . . . RE^{3+}

Ultraviolet . . . . . UV

Vacuum-Ultraviolet . . . . . VUV

X-ray diffraction . . . . . XRD

Ytterbium orthophosphate . . . . . $YbPO_4$

Yttrium orthophosphate . . . . . YPO_4

ACKNOWLEDGMENTS

It took a village to complete this research. First, I would like to thank my advisor, Dr. Corinne Packard, for her invaluable support and guidance through it all. I would also like to acknowledge the Colorado Center for Advanced Ceramics, the Metallurgical and Materials Engineering Department, the National Science Foundation, and the National Defense Science and Engineering Graduate Fellowship Program, which have provided financial and material support for this research. In addition, I truly appreciate the insightful conversations and contributions from my committee members, Dr. Ivar Reimanis, Dr. Jeramy Zimmerman, and Dr. Geoff Brennecka. Moreover, I'd like to thank Dr. Bianca Haberl, Dr. Reinhard Boehler, Dr. Jesse Smith, Dr. Martin Kunz, Dr. Tom Duffy, and John Copley for their expertise and assistance with high-pressure instrumentation and experiments at Oak Ridge National Lab, Argonne National Lab, Berkeley National Lab, and Princeton University. Furthermore, I would like to thank the members of the Packard Research Group and fellow Hill Hall ceramists for their camaraderie in the trenches. Finally, I would like to thank my family for their support in getting me to this point.

Vous savez qui vous êtes.

CHAPTER 1
INTRODUCTION

This chapter introduces the crystal structures and high-pressure phase behavior of rare earth orthophosphates, the state of the field, and motivating factors for this research.

1.1 Rare Earth Orthophosphates

Rare earth orthophosphates ($REPO_4$s) are highly refractory and insoluble ceramics relevant to various research fields ranging from geoscience to optics to structural composites [1]. Much of the world's RE elements come from naturally-occurring xenotime and monazite minerals, whose properties and formation are of great relevance in geochronology and mining [2]. Highly pure $REPO_4$s have also been synthesized and precisely doped for optical applications including lasers and scintillators [3, 4]. More recently, $REPO_4$s have garnered interest as potential fiber coatings for oxide-oxide ceramic matrix composites (CMCs) used in aerospace components subject to extreme conditions [5, 6]. The pressure-induced phase transformation of certain compositions has been shown to enhance CMC performance, and exploiting this transformation requires understanding polymorphism in $REPO_4$s [7].

In equilibrium at atmospheric pressure, a phase boundary exists in the middle of the lanthanide series. Heavier compositions (RE = Tb-Lu, Sc, and Y) adopt the xenotime (tetragonal, $I4_1/amd$, Z=4) structure, while lighter compositions (RE = La-Gd) adopt the monazite (monoclinic, $P2_1/n$, Z=4) structure [9]. Figure 1.1 illustrates the phase boundary as well as the phases' crystal and molecular structures.

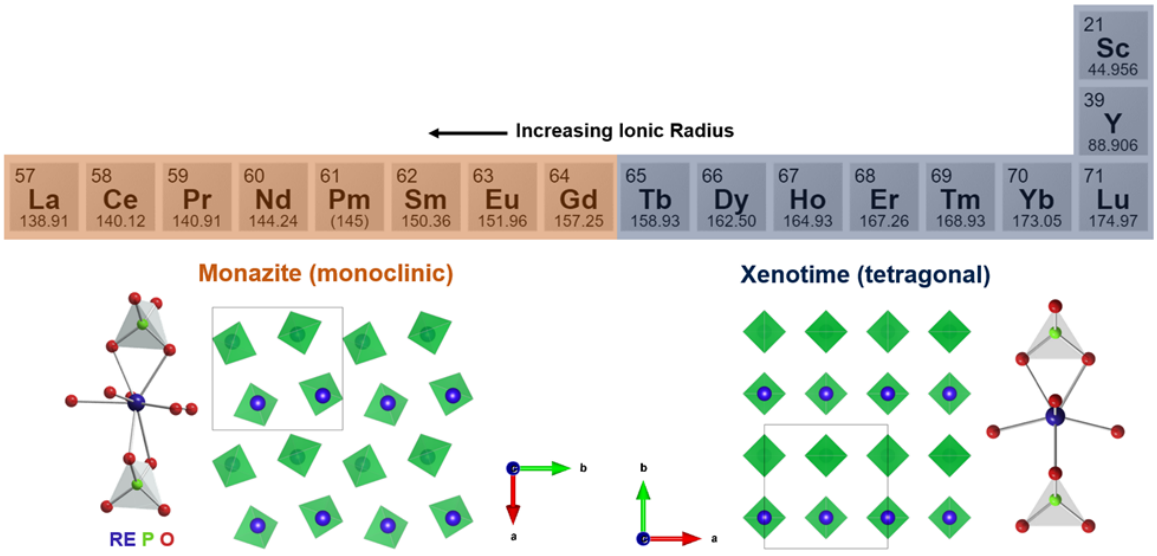

Figure 1.1 The $REPO_4$ monazite-xenotime phase boundary shown with the phases' [001] crystal structure views and molecular structures. In the crystal views, violet spheres, green tetrahedra, and rectangles represent RE^{3+} cations, PO_4 groups, and unit cells, respectively. Molecular structures are adapted from Heuser et al. [8].

At high pressures, most xenotime compositions (RE = Tb-Tm, Y) transform into monazite. This transformation involves an increase in the number of RE-O bonds (8 to 9) for every RE atom in the structure, a loss in RE site symmetry (D_{2d} to C_1), and a volume loss of ~5%. The transformation mechanism is currently understood as follows: under compression, RE-O bonds are distorted to the point of reconfiguration, while the PO_4 tetrahedra are effectively rigid [10, 11]. Not all single-RE xenotime compositions transform to monazite; Zhang et al. reported that $YbPO_4$, $LuPO_4$, and $ScPO_4$ transformation to the scheelite (tetragonal, $I4_1/a$) structure [12, 13].

1.2 State of the Field and Motivation

This section covers the state of the mechanical, optical, and mechano-optical fields of $REPO_4$ literature and motivates the work presented in this dissertation.

1.2.1 Mechanical Studies of Rare Earth Orthophosphates

Pioneering research by Drs. Peter E. Morgan and David B. Marshall showed $LaPO_4$ (monazite) to be a promising fiber coating in alumina-alumina ceramic matrix composites (CMCs) [5, 14]. While several materials (e.g., graphite, hexagonal boron nitride) can provide a weak interface with alumina, $LaPO_4$ (among other $REPO_4$s) has the advantage of phase stability and oxidation-resistance at temperatures as high as 1750°C in air [14]. In more recent years, the polymorphism of $REPO_4$s has drawn interest toward xenotime compositions in which the transformation to monazite offers the possibility of additional plasticity and toughening mechanisms. Hay et al. showed fiber coatings made of $DyPO_4$ (as well as other transforming xenotimes) can deflect or arrest cracks (see Figure 1.2) and result in lower fiber push-out stresses than non-transforming, monazite $LaPO_4$ coatings [15].

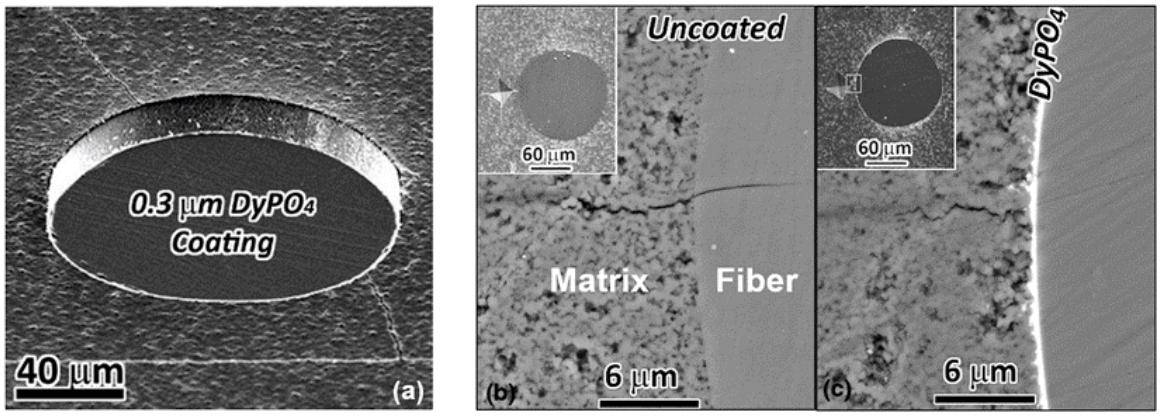

Figure 1.2 $DyPO_4$ fiber coating in oxide-oxide CMC. Adapted from Hay et al. [15]. (a) $DyPO_4$-coated fiber pushed out with crack deflected around fiber. Matrix-fiber interface showing (b) crack propagation without $DyPO_4$ coating and (c) crack arrest with $DyPO_4$ coating. Insets show indents used to initiate cracks.

A key characteristic in selecting xenotime candidates is a low xenotime → monazite transformation onset pressure (P_{onset}). Xenotimes closer to the phase boundary are desirable in this respect, and P_{onset} has long been assumed to decrease linearly with increasing RE^{3+} ionic radius (see Figure 1.3) [7, 16].

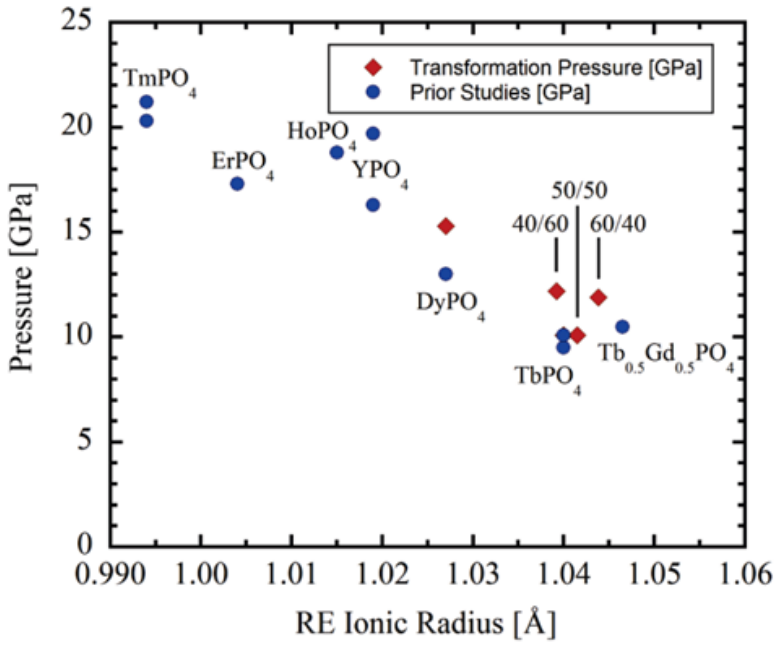

Figure 1.3 Previously compiled xenotime → monazite P_{onset} values adapted from Musselman [16]. Red diamonds are RS-based values reported by Musselman, while blue circles are from prior RS and XRD studies. This plot also includes $Gd_xDy_{1-x}PO_4$ compositions, which are labeled using the following convention: x/1-x.

Determining P_{onset} for xenotime compositions has involved *in situ* diamond anvil cell (DAC) Raman spectroscopy (RS) and synchrotron x-ray diffraction (XRD) experiments. In their RS study, Tatsi et al. reported the high-pressure polymorph of $TbPO_4$ was likely monazite based on comparison to Raman spectra of known monazites [17]. López-Solano et al. later confirmed the monazite phase of $TbPO_4$ in their XRD study and provided detailed structural information including an equation of state (EOS) for both phases [18]. In their single-crystal XRD work, Gomis et al. showed $HoPO_4$ and $TmPO_4$ transform to the monazite structure and gave elastic constants and an EOS for both materials in the xenotime phase [19]. In their synchrotron XRD study, Lacomba-Perales et al. showed the xenotime-monazite transformation in $ErPO_4$ and YPO_4 and gave an EOS for both phases [11].

At the start of this work, similar insight into the pressure-induced phase transformation of xenotime $DyPO_4$ had yet to be published. Musselman et al. and Stavrou et al. used *in*

situ RS to report $DyPO_4$ P_{onset} values of 15.3(9) GPa and 13 GPa, respectively [20, 21]. These authors describe emergent Raman peaks at these pressures as consistent with Raman peaks of monazite $TbPO_4$. Stavrou et al. further claim that monazite $DyPO_4$ transforms to scheelite at higher pressures (∼30 GPa), yet the evidence to support this claim has yet to be published [21]. Heuser et al. reported crystallographic details of monazite $DyPO_4$ but as a metastable phase synthesized at 1 atm [8]. Although these studies mark important first steps, crystallographic proof of the $DyPO_4$ xenotime-monazite phase transformation, a subsequent re-assessment of compositional P_{onset} trends, and greater understanding of transformation kinetics are critical for advancing the $REPO_4$ literature.

Furthermore, extreme environment applications like CMC fiber coatings involve complex stress states, so understanding the effect of shear on transformation is key in screening material candidates. In fact, Hay et al. observe (via *ex situ* transmission electron microscopy) monazite grains in xenotime $TbPO_4$ subject to indentation and in other xenotime compositions subject to fiber push-out tests [7, 15]. However, *in situ* experimental corroboration of transformation in those xenotime compositions is precluded by the use of hydrostatic media in prior DAC experiments, which show transformation at pressures much higher than those expected in Hay et al.'s tests [7, 17, 18]. Deviatoric stress is expected to lower the xenotime-monazite P_{onset} since shear disrupts local symmetry and promotes bond breakage, effectively reducing the barrier to the RE-O bond reconfiguration that occurs during phase transformation [7]. Surveying the literature reveals the impact of shear on $REPO_4$ phase transformation has yet to be systematically investigated. Lacomba-Perales et al. noted shear appeared to promote earlier transformation in YPO_4, but this conclusion was based on a cursory comparison of their findings to a prior YPO_4 study done by others [11]. The closest comparison point available is a systematic study conducted on another ABO_4 compound, orthorhombic $BaSO_4$, by Santamaría-Pérez et al. [22]. These researchers used fluid PTMs with differing hydrostatic limits and found less hydrostatic conditions trigger earlier $BaSO_4$ transformation and widen the pressure range

of phase coexistence. Moreover, assessing the shear-dependence of phase transformations in multiple xenotime $REPO_4$ compositions is critical given the known RE-dependence of the stability of $REPO_4$ phases [9, 23, 24].

1.2.2 Photoluminescence (PL) Studies of Trivalent Rare Earth Ions

$REPO_4$s and other materials containing trivalent rare earth ions (RE^{3+}) are prevalent in optical research and applications. The 4f intraconfigurational energy levels of RE^{3+}s yield sharp, characteristic PL emissions that are often in the visible region [25]. These levels represent ionic (not electronic) states, and each level represents a unique configuration of the 4f orbitals. The high degree of level-splitting in RE^{3+}s (as shown in Figure 1.4) is primarily caused by electron-electron repulsion ($\sim 10^4$ cm^{-1}) and spin-orbital coupling ($\sim 10^3$ cm^{-1}) [26]. The relative positions of these levels were determined by the Cold War era scientist, Dr. G. H. Dieke, whose samples were RE^{3+}-doped $LaCl_3$ [27]. Nevertheless, a Dieke diagram can be used to identify RE^{3+} 4f-4f emission bands in $REPO_4$s because host-dependent crystal field effects are relatively weak ($\sim 10^2$ cm^{-1}) [28].

.

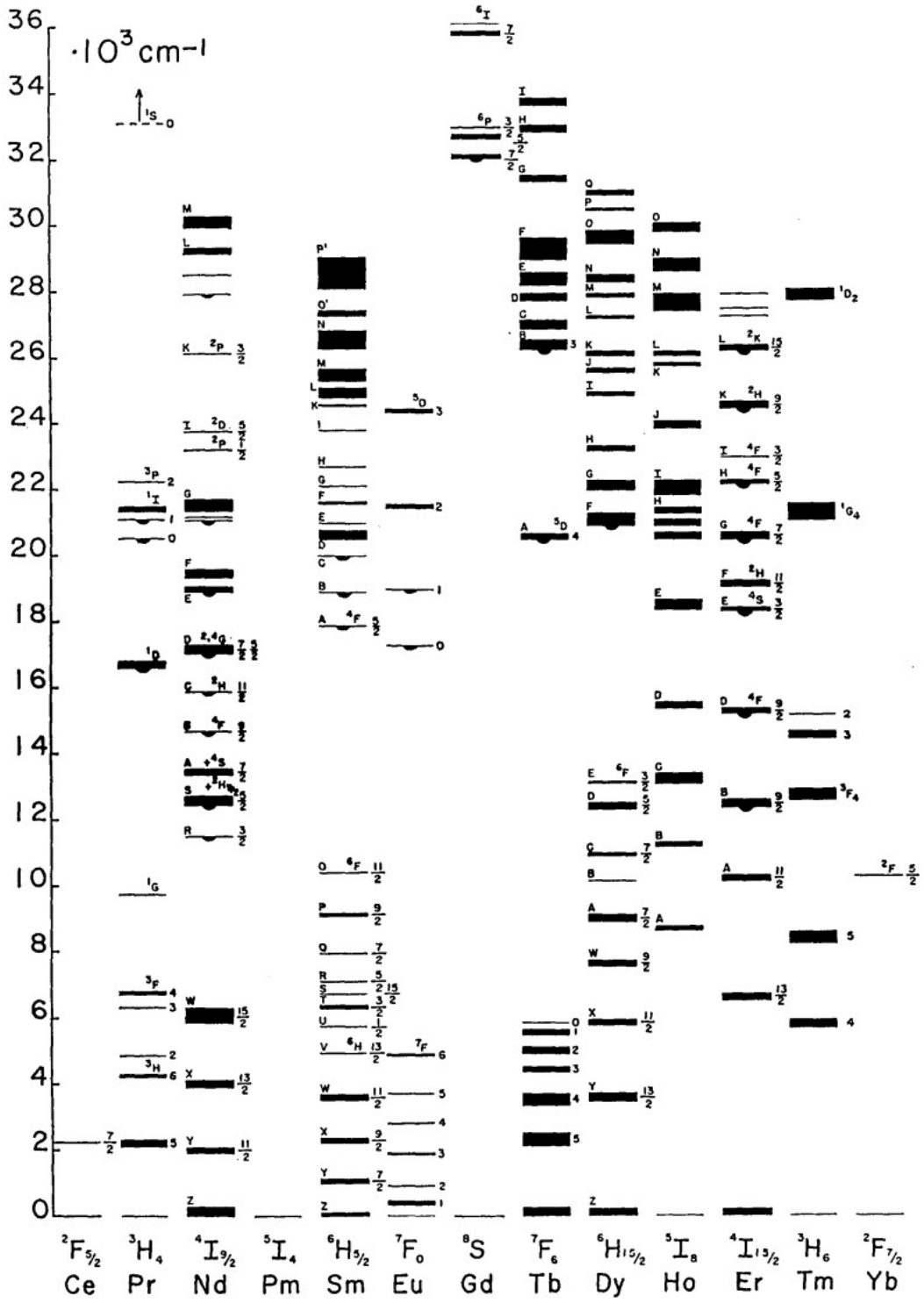

Figure 1.4 Dieke diagram showing observed 4f intraconfigurational energy levels of RE^{3+}s. Levels with semicircles below them are common emissive states. Adapted from Withnall et al. [26]

When a photon of appropriate energy is absorbed by an RE^{3+}, the RE^{3+} is excited from its ground state (lowest level seen on Dieke diagram) to a higher energy state. When relaxing back to a lower energy or ground state, the RE^{3+} emits a photon. Because photon energies are rarely exactly matched to the gaps between states, non-radiative relaxation (i.e., phonon emission) plays a critical role in maintaining the conservation of energy. Most optical work involving RE^{3+}s simply exploits the PL to convert photons from one energy to another. When the emitted photon has a higher energy than the absorbed photon(s), the PL process is termed up-conversion; the opposite case is termed down-conversion or direct excitation PL (see Figure 1.5).

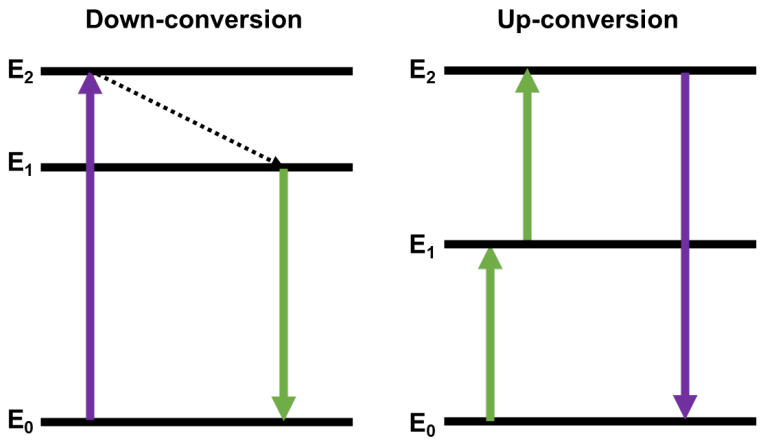

Figure 1.5 Simplified schematic showing the difference between down-conversion and up-conversion PL processes. Solid arrows indicate photons while the dashed arrow represents a phonon.

Display, lighting, and scintillation applications employ down-converting materials, in which the relative ratios of RE^{3+} dopants can be tuned to control overall emission color [29–31]. Bio-imaging research involves up-converting RE^{3+}-doped nanoparticles so that infrared (rather than harmful UV) light can be used to generate visible emissions from within live tissue [32]. Solar spectrum conversion research seeks to take advantage of both processes in RE^{3+}-doped materials to convert IR and UV photons into photons of intermediate energies that are more easily absorbed by silicon [33].

The PL emissions of RE^{3+}s have also been exploited for characterizing the state or properties of bulk materials. For example, the emissions of Nd^{3+} have been used to gauge the level of radiation-induced amorphization in Nd^{3+}-doped $LaPO_4$ and YPO_4 [34]. In addition, RE^{3+}-containing paints and coatings such as Tb^{3+}-doped Y_2SiO_5 have been demonstrated as thermal history sensors for components in the hot section of gas turbines [35, 36]. The fundamental phenomena responsible for these sensing applications are the crystallinity- and temperature-dependencies of the RE^{3+} PL emissions.

1.2.3 Mechano-Optical Coupling

The vast majority of $REPO_4$ literature falls into one of two categories: mechanics or optics. The former is focused on high-pressure dynamics, while the latter exploits the excellent PL characteristics of RE^{3+}s. Although mechanical and optical properties have a common origin in structure, exploration of mechano-optical coupling is extremely limited in the literature. More specifically, published work exploring the effect of stress on RE^{3+} PL in $REPO_4$s is quite new and sparse. Nevertheless, discovering connections between stress and PL emission can have two valuable impacts.

First, exploiting PL can advance high-pressure phase transformation research in $REPO_4$s and other luminescent ABO_4 materials. Traditionally, RS and synchrotron XRD have been used to determine P_{onset} values. Although both of these techniques can deliver unique material insight, PL offers a higher signal-to-noise ratio than RS (due to the lower probability of Raman scattering) and is much more accessible than synchrotron XRD. In PL spectra, changes in the number of peaks (or other peak metrics) can indicate a change in the local environment of the emitting ion. For example, Lösch et al. discovered the PL emission spectrum of Eu^{3+} from various Eu^{3+}-doped xenotime $REPO_4$s changes with the minority phase makeup of the host matrix [37]. Yang et al. reported differences in the green emission band ($\sim$543 nm) of the ambient pressure PL spectra of $TbPO_4$ powder synthesized in the xenotime and metastable monazite phases [38]. PL spectroscopy is likely to reveal the P_{onset} of the xenotime $\rightarrow$ monazite phase transformation because the emitting

RE^{3+} ions undergo a coordination change ($8 \rightarrow 9$) and a loss of site symmetry ($D_{2d} \rightarrow C_1$).

Second, high-pressure PL characterization may open the door to a remote, optical pressure-sensing functionality in $REPO_4$s. Demonstrating this functionality involves the development of a calibration curve linking the material's PL emissions to the stress it experiences. Potential applications include pressure-sensitive coatings or paints for extreme environments. The non-contact nature of this functionality could aid in *ex situ* periodic inspections or failure analysis. Furthermore, PL could be used to perform quick spot checks or to methodically map stress depending on the optical components available.

The only published work exploring the stress-dependence of RE^{3+} PL in $REPO_4$s is Runowski et al.'s *in situ* DAC study of up-converting $LaPO_4$: Yb^{3+}, Tm^{3+} and YPO_4: Yb^{3+}, Tm^{3+} [39]. The latter composition is particularly interesting as it undergoes the xenotime-monazite transformation at high pressure. Because Y^{3+} has no 4f electrons and is optically inactive, the two RE^{3+} dopants were used to perform up-conversion by the following process: Yb^{3+} absorbs IR photons, Yb^{3+} transfers absorbed energy to Tm^{3+}, and Tm^{3+} emits light. This work (see Figure 1.6) uncovered not only pressure-induced changes in PL peak metrics, but also discontinuities in certain peak positions, widths, and relative ratios at pressures close to the xenotime-monazite P_{onset} ($\sim$14 GPa). The quantum efficiency of the up-conversion process, however, is about an order of magnitude lower than that of down-conversion, and requires a more complex experimental setup [40]. Despite the higher efficiency of down-conversion, the stress-dependence of PL in down-converting xenotimes has yet to be reported in the literature. Measuring this dependence would likely yield calibration curves and may enable a higher-efficiency, optical pressure-sensing functionality in $REPO_4$s.

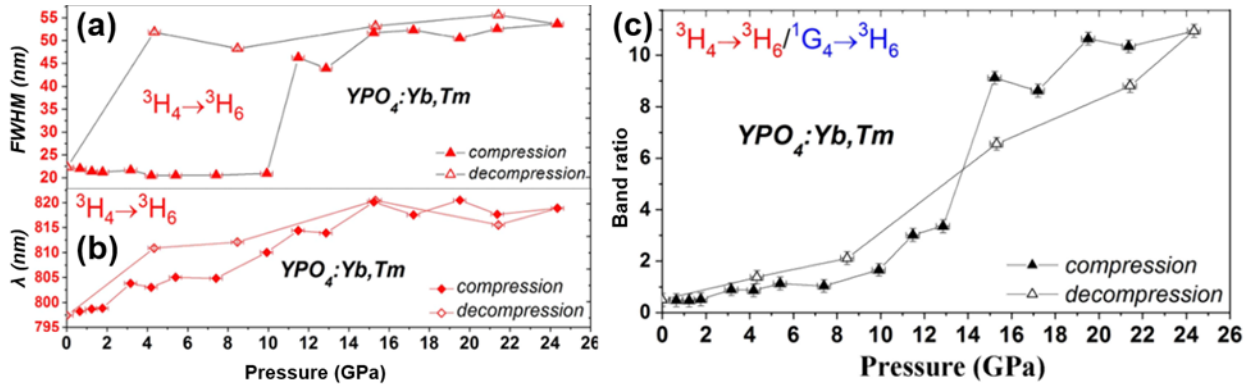

Figure 1.6 Pressure-dependences of select PL peak metrics of YPO_4: Yb^{3+}, Tm^{3+} adapted from Runowski et al. [39] (a) Full width at half maximum (FWHM). (b) Wavelength. (c) Relative peak ratio. Panels (a) and (c) show discontinuities during compression at pressures close to P_{onset}.

A critical factor enabling mechano-optical research is the remarkable RE^{3+} compositional flexibility exhibited by $REPO_4$s; that is, one RE^{3+} can easily be substituted for another in the $REPO_4$ crystal structure. As a result, an optically active RE^{3+} can be doped into a $REPO_4$ whose intrinsic RE^{3+}s may not be optically active.

CHAPTER 2

EXPERIMENTAL METHODS

This chapter covers the synthesis and processing of $REPO_4$ powders used in this work, diamond anvil cell (DAC) operation, and data processing and analysis for the two different *in situ* characterization techniques employed in this dissertation (XRD and PL).

2.1 REPO4 Synthesis and Processing

The $REPO_4$ samples in this work are xenotime $DyPO_4$ and $TbPO_4$ powders. Synthesis begins with the precipitation reaction shown in Equation 2.1.

$$RE(NO_3)_3 \cdot nH_2O_{(aq)} + H_3PO_{4(aq)} \longrightarrow REPO_4 \cdot nH_2O_{(s)} + 3HNO_{3(aq)} \tag{2.1}$$

First, 0.1 mol of $RE(NO_3)_3 \cdot nH_2O$ is dissolved in 200 mL of de-ionized water. Then, an excess of H_3PO_4 (> 0.1 mol) is diluted in 200 mL of de-ionized water. This excess helps to ensure that all precursor reacts. These two solutions are then combined under vigorous magnetic stirring because the precipitation of white powder begins immediately. The resultant solution has a pH of $\sim$1, which is then adjusted to $\sim$10 via the dropwise addition of ammonium hydroxide (NH_4OH, 30%) to accelerate precipitation. All reagents are obtained from Alfa Aesar. Next, the solution is centrifuged for 10 min at 1500 rpm. The supernatant solution is decanted, and the powder is dried in a vacuum oven overnight (100°C, $\sim$0.1 atm). The dried powder is then ball milled in ethanol with zirconia media for 24 hours. The same centrifuge process is used to separate the milled powder from the ethanol, and vacuum-drying takes a few hours (80°C, $\sim$0.1 atm). If the powder consolidates during drying, it is ground into a fine powder using a mortar and pestle.

At this stage of the process, the powder is a hydrated $REPO_4$ with a hexagonal crystal structure. High temperature calcination is required to remove the coordinated water molecules and to ensure complete crystallization of the xenotime phase. The calcination

profile for $DyPO_4$ is as follows: 5°C/min ramp to 550°C, 3 hr hold at 550°C, 5°C/min ramp to 1200°C, and 2 hr hold at 1200°C. The calcination of $TbPO_4$ involves 2 profiles run in series. The first is like that of $DyPO_4$, except the final hold is at 1600°C for 5 hrs. The second profile is a 5°C/min ramp to 1200°C with a 5 hr hold at 1200°C. All cooling is done at a rate of 5°C/min. $TbPO_4$ requires the higher temperature step in order to remove a monazite impurity phase. The monazite impurity likely exists due to $TbPO_4$'s closer proximity to the xenotime-monazite phase boundary in the ABO_4 Bastide phase stability diagram [7]. Figure 2.1 shows the verification of phase purity using powder XRD on a PANalytical PW3040 diffractometer. Rietveld refinement of XRD patterns is performed using HighScore Plus [41, 42].

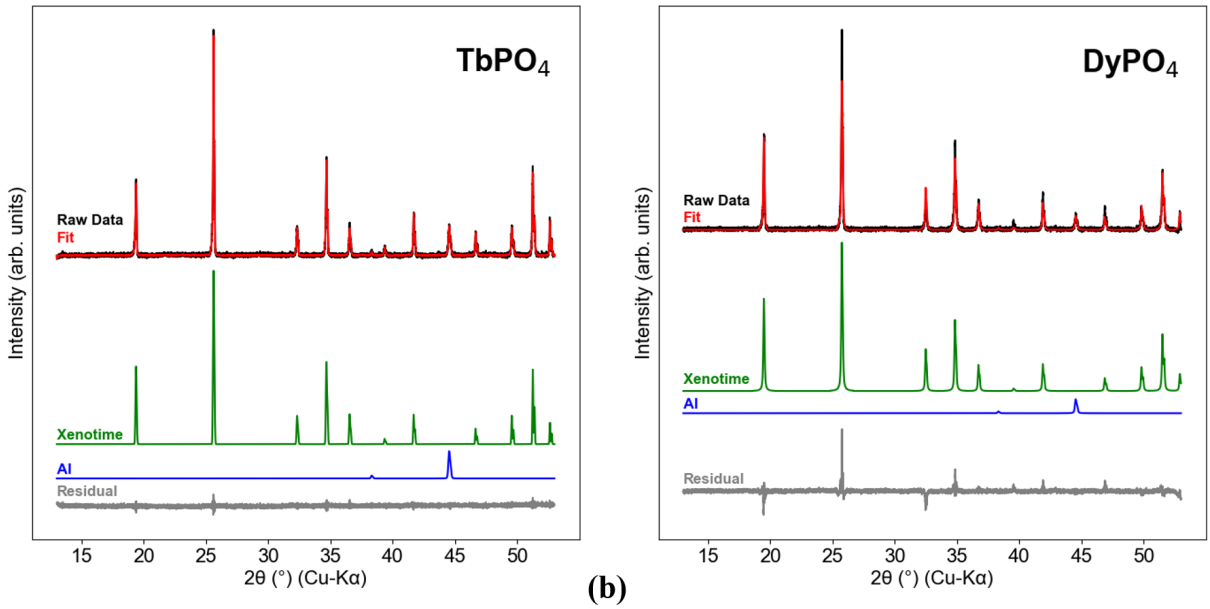

Figure 2.1 Refined XRD patterns of (a) $TbPO_4$ and (b) $DyPO_4$ powders used in this dissertation. Al peaks arise from the aluminum sample holder.

2.2 The Diamond Anvil Cell (DAC) Technique

The development of the diamond anvil cell (DAC) by Drs. Alvin Van Valkenburg, Charles E. Weir, Ellis R. Lippincott, and Elmer N. Bunting at the US National Bureau of Standards in 1958 has enabled the high-pressure research performed in this dissertation

and in all of the studies cited within [43]. This handheld device is capable of generating the gigapascal pressures necessary to induce phase transformation in many ceramic materials including $REPO_4$s. In addition, diamonds have high transmittance over a broad spectrum, which enables *in situ* characterization using lasers and x-rays. DAC operation involves a ductile, metallic gasket sandwiched between diamond anvils. A hole pre-drilled in the center of the gasket acts as a sample chamber and is pressurized when the diamond anvils are brought closer together (see Figure 2.2).

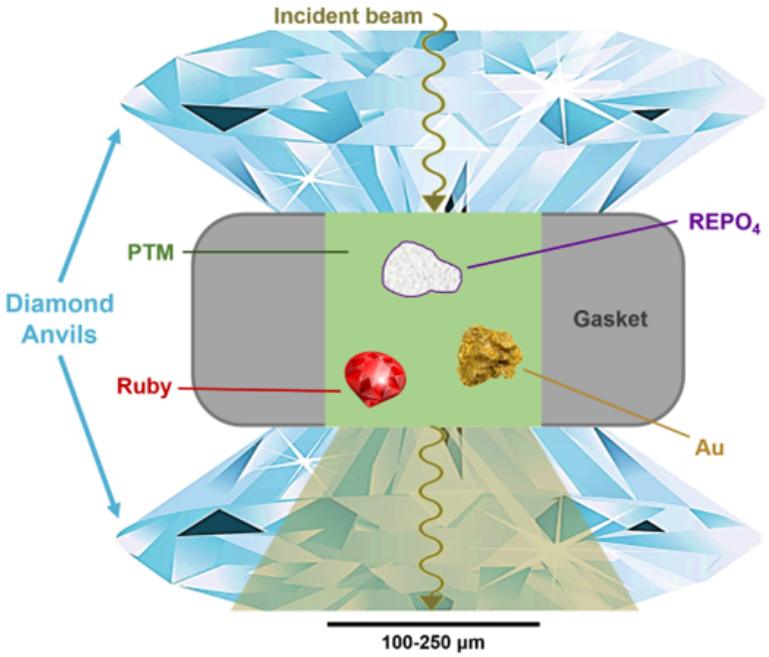

Figure 2.2 Simplified cross-section schematic of a loaded DAC. PTM is the pressure-transmitting medium used to create a hydrostatic environment in the gasket hole.

Due to significant gasket deformation during loading, the pressure in the gasket hole cannot simply be determined by force per area calculations. Rather, a pressure marker (an internal standard) is placed in the gasket hole. In spectroscopy experiments, ruby is used as the marker because its pressure-dependent fluorescence is well-understood and well-calibrated [44]. In diffraction experiments, gold is employed because it has a well-calibrated equation of state (EOS) [45]. Next, the sample is placed inside the gasket hole along with a pressure-transmitting medium (PTM) that can provide a hydrostatic

environment. Every PTM has a hydrostatic limit; that is, a pressure at which the PTM solidifies and begins to support shear stress [46]. Once this limit has been exceeded in an experiment, one can no longer assume that the sample is experiencing a hydrostatic environment. This dissertation also employs solid PTMs (i.e., media that are solid at 0 GPa). Although a solid PTM has an effective hydrostatic limit of 0 GPa, its bulk modulus (incompressibility) may be an indirect indicator of its ability to impart deviatoric stress on the sample. At a given DAC pressure, an increase in PTM bulk modulus results in less PTM compression, which is expected to generate greater contact stresses at PTM-sample interfaces. Given the non-uniform magnitude and direction of these contact stresses, greater shear stress is expected to be induced in the sample. While the mechanism by which solid PTMs impart shear has yet to be detailed in the literature, results from prior DAC experiments on α-Ti support the expectation that PTMs with higher bulk moduli impart more shear stress on the sample than PTMs with lower bulk moduli [47].

Finally, ramping the sample to high pressure is done in one of two ways depending on the DAC design: a screw mechanism for discrete, step-wise ramping or a gas membrane pneumatic mechanism for continuous ramping. The maximum pressure of the experiment is limited by the pressure at which the gasket blows out. Collecting data while ramping down to low pressure is complicated by unpredictably fast pressure loss when the diamonds are moved apart from each other. This pressure loss occurs because the gasket has been compressed beyond its elastic limit and can no longer maintain a seal between the diamonds.

2.3 *In Situ* DAC XRD

In situ DAC XRD experiments in this dissertation were conducted at room temperature at synchrotron x-ray beamlines. Collecting sufficient signal in a reasonable amount of time from the micro-volume of material in a DAC requires the high fluxes and micron-scale spot sizes available at synchrotron beamlines. In addition, the low divergence of synchrotron x-rays is critical for distinguishing closely spaced peaks in XRD patterns.

XRD experiments shown in Chapters 3 and 4 were conducted at beamline 16-ID-B of HPCAT (High Pressure Collaborative Access Team) at the Advanced Photon Source at Argonne National Laboratory. Chapter 3 involves XRD data collected over two synchrotron beam trips, resulting in slight differences in experimental details (e.g., beam wavelength, DAC pressurization mechanism, exposure time, gasket metrics). Such differences are detailed in Table 3.1. Additional XRD experiments shown in Chapter 5 were performed at beamline 12.2.2 of the Advanced Light Source at Berkeley National Laboratory, and experiment-specific details are provided in the same chapter. In most synchrotron XRD experiments, a Druck PACE 6000 pressure controller was used to pressurize the DAC [48]. Ruby powder (Almax easyLab Inc., Cambridge, MA) was used to gauge pressure during initial membrane engagement, while gold powder ($\geq$99.96% metals basis, Alfa Aesar, Ward Hill, MA, USA) was used during diffraction data collection. XRD data collection often begins at a pressure of a few GPa because some initial compression is required to confirm membrane engagement. This initial compression, however, does not preclude any material insight as $REPO_4$ phase transformations have not been reported at such low pressures (as corroborated by the findings in this dissertation).

XRD pattern integration, masking, and background subtraction were performed using Dioptas [49]. Pattern fitting was then performed using X'Pert HighScore Plus [42]. This software fits monazite using the $P2_1/c$ cell setting as a default. Although both the $P2_1/c$ and $P2_1/n$ cell settings are valid descriptions of monazite (space group No. 14), fitted lattice parameters were converted to the $P2_1/n$ cell setting to facilitate comparison to the literature. The LeBail fitting approach was used instead of traditional Rietveld structural refinement to accommodate the significant preferred orientation present in all scans [50]. This preferred orientation is an artifact caused by the small spot size of the beam with respect to the grain size of the sample (effectively sampling a finite number of grains). For computation involving derived data (e.g., cell setting conversion, unit cell metrics, pressure calculation), the uncertainties Python package was used to propagate error [51]. For all

numerical values shown with a number in parentheses afterwards, the number in parentheses represents the standard deviation of the last digit of the value before the parentheses.

2.4 *In Situ* DAC PL Spectroscopy

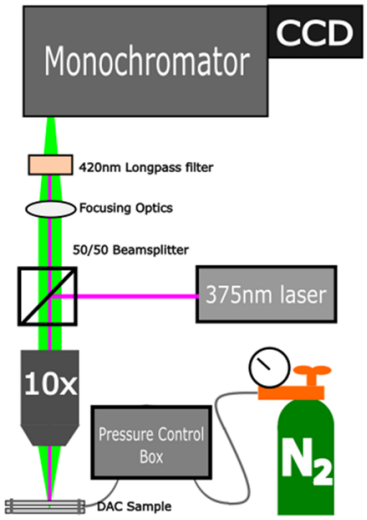

Figure 2.3 Schematic of DAC PL spectroscopy experimental setup.

In situ DAC PL experiments in this dissertation employ the experimental setup shown in Figure 2.3. A 375 nm pulsed laser (Picoquant LDH-P-C-375) is sent through a 50/50 beam-splitter and a 10x objective lens (Nikon Plan Fluor 10x/0.30) to enter the DAC and excite the powder. The laser excites the powder with a repetition rate of 10 MHz, pulse width <90 ps, and average power of 83.5 μW at the DAC (corresponding to an average intensity of 290 W/cm^2). The pressure of the DAC is controlled pneumatically (using nitrogen gas) or via screws on the DAC. The emitted light travels back through the objective and beam-splitter where it enters focusing optics (two lenses to focus into the monochromator). The emitted light then passes through a 420 nm long-pass filter and enters the monochromator, where it is diffracted and then captured on the CCD camera. The emission was focused into the 10 μm slit of a monochromator (Acton SP2150) and collected on a PIXIS256 CCD. The spectral resolution is 0.1 nm, and the laser spot is 3.4

μm by 8.6 μm. For ruby emission collection, the center wavelength was 690 nm, while for $TbPO_4$, the "Step & Glue" feature on Lightfield was utilized to capture a range from 470 nm to 640 nm. For all experiments, the reported pressure at each pressure step is the average of pressures derived from 3 different rubies. When fitting ruby peaks to find the peak center, the standard error of the mean (of the peak center wavelength) was propagated through the ruby equation of state in order to obtain a pressure error bar [44]. In $TbPO_4$ spectra, band centroids are calculated via a center of mass approach because fitting each band with a single curve does not accurately represent the data. Fitting each band with multiple curves (given the multiple peaks within each band) is highly dubious due to the lack of fundamental understanding of RE^{3+} hyperfine energy level-splitting in the literature. Without knowing the expected number of peaks and expected peak locations, multi-peak fits of bands become unreliable, especially when peaks broaden at high pressure.

CHAPTER 3

IN SITU SYNCHROTRON DIFFRACTION OF PRESSURE-INDUCED PHASE TRANSITION IN DYPO4 UNDER VARIABLE HYDROSTATICITY

Reproduced with permission from *Physical Review B* and co-authors (included in Appendix A).

Jai Sharma[1], Matthew Musselman[1], Bianca Haberl[2], and Corinne E. Packard[1]

[1]Colorado School of Mines, Golden, Colorado 80401, USA

[2]Neutron Scattering Division, Neutron Sciences Directorate, Oak Ridge National Laboratory, Oak Ridge, Tennessee 37831, USA

This manuscript describes the effect of non-hydrostatic stress on the pressure-induced xenotime-monazite phase transformation of $DyPO_4$. *In situ* DAC synchrotron XRD was used to directly interrogate crystal structure. Experiments revealed the high-pressure monazite phase of $DyPO_4$ as well as the sensitivity of P_{onset} to stress state. Findings were placed in context with experimental and computational $REPO_4$ literature. This chapter includes an overview of the authors' contributions, a summary of the key findings and contributions of this work, and the full manuscript published in *Physical Review B* in May 2021 (https://doi.org/10.1103/PhysRevB.103.184105).

3.1 Author Contributions

Matthew Musselman (a prior graduate student at Colorado School of Mines) synthesized samples, and he performed beamline experiments with the help of Dr. Bianca Haberl (a high-pressure beamline scientist from Oak Ridge National Lab) and Dr. Packard. I performed all the data analysis presented in this manuscript, and I was the primary author of this work. Drs. Haberl and Packard contributed to data interpretation and manuscript editing.

3.2 Scientific Advancements and Conclusions

The work presented in this chapter provides the first direct, crystallographic proof of the high-pressure monazite phase of $DyPO_4$ and the first systematic evaluation of the effect of non-hydrostatic stress on the $REPO_4$ xenotime-monazite phase transformation. The XRD-based transformation onset pressure (P_{onset}) of $DyPO_4$ (measured under hydrostatic conditions) shows prior Raman spectroscopy-based P_{onset} values are significant over-estimations and disrupts the widely-held assumption that $REPO_4$ P_{onset} decreases linearly with RE^{3+} ionic radius.

3.2.1 Key Findings

- The high-pressure monazite phase of $DyPO_4$ is crystallographically confirmed.
- The $DyPO_4$ xenotime-monazite transformation P_{onset} is 9.1 GPa – significantly lower than previously reported values based on Raman spectroscopy.
- The $DyPO_4$ xenotime-monazite transformation P_{onset} is significantly reduced in a non-hydrostatic environment.
- The large pressure range of xenotime-monazite phase coexistence suggests this transformation is diffusional rather than martensitic.
- Experiment-based P-V (pressure-volume) equations of state are reported for the first time for xenotime and monazite $DyPO_4$.

3.2.2 Key Contributions

- This work demonstrates Raman spectroscopy is insufficient for accurately determining the P_{onset} of the xenotime-monazite transformation due to the technique's poor signal-to-noise ratio.
- This study shows the xenotime-monazite P_{onset} does not decrease linearly with RE^{3+} ionic radius (as is commonly assumed in literature); rather, it is discontinuous at

some critical ionic radius between those of Y^{3+} and Dy^{3+}.

- This work shows the the xenotime-monazite P_{onset} value is sensitive to stress state.
- The stress state-sensitivity of the xenotime-monazite phase transformation means $REPO_4$s considered for CMC fiber coatings should be tested under non-hydrostatic conditions.
- The reduction of P_{onset} under non-hydrostatic conditions suggests $REPO_4$ compositions with higher hydrostatic P_{onset} values should not be automatically excluded from consideration for CMC applications.

3.3 Abstract

In situ synchrotron x-ray diffraction was conducted on polycrystalline $DyPO_4$ to elucidate the details of the pressure-induced transition from the xenotime polymorph to the monazite polymorph. We used three different pressure-transmitting media (neon, a 16:3:1 methanol-ethanol-water mixture, and potassium chloride) to investigate the effect of hydrostaticity on the phase behavior. Specifically, our data clearly show a hydrostatic onset pressure of the xenotime-monazite transition of 9.1 GPa, considerably lower than the 15.3 GPa previously determined by Raman spectroscopy. Based on (quasi)hydrostatic data taken in a neon environment, third-order Birch-Murnaghan equation-of-state fits give a xenotime bulk modulus of 144 GPa and a monazite bulk modulus of 180 GPa (both with pressure derivatives of 4.0). Structural data and axial compressibilities show that $DyPO_4$ is sensitive to shear and has an anisotropic response to pressure. More highly deviatoric conditions cause the onset of the transition to shift to pressures at least as low as 7.0 GPa. We attribute early transition to shear-induced distortion of the PO_4 tetrahedra. Our characterization of the high-pressure behavior of $DyPO_4$ under variable hydrostaticity is critical for advancing rare earth orthophosphate fiber coating applications in ceramic matrix composites and may inform future tailoring of phase composition for controlled shear and pressure applications.

3.4 Introduction

Rare earth orthophosphates ($REPO_4$s) are a burgeoning class of ceramics, most of which transition to other phases under pressure [1, 11, 23]. In equilibrium at atmospheric pressure, heavier compositions (RE = Tb-Lu, Sc, Y) adopt the xenotime (tetragonal, $I4_1/amd$) structure while lighter compositions (RE = La-Gd) adopt the monazite (monoclinic, $P2_1/n$) structure [9]. At high pressures, xenotime compositions can transition into monazite or other structures. This polymorphism has spurred recent interest in $REPO_4$s for ceramic matrix composite (CMC) applications, where the xenotime-monazite transition offers the possibility of additional plasticity and toughening mechanisms in oxide-oxide CMCs [15, 52]. In particular, Hay et al. showed that $DyPO_4$ (among other xenotime) fiber coatings deflect cracks and result in lower fiber push-out stresses than monazite $LaPO_4$ coatings.

Figure 3.1 shows the xenotime and monazite structures of $DyPO_4$ and the mechanism of transition is as follows: under compression, Dy-O bonds are distorted to the point of reconfiguration (the RE coordination number increases from 8 to 9), while the PO_4 groups (grey tetrahedra) are effectively rigid [53, 54]. This description is widely accepted for all $REPO_4$ compositions that undergo the xenotime-monazite transition.

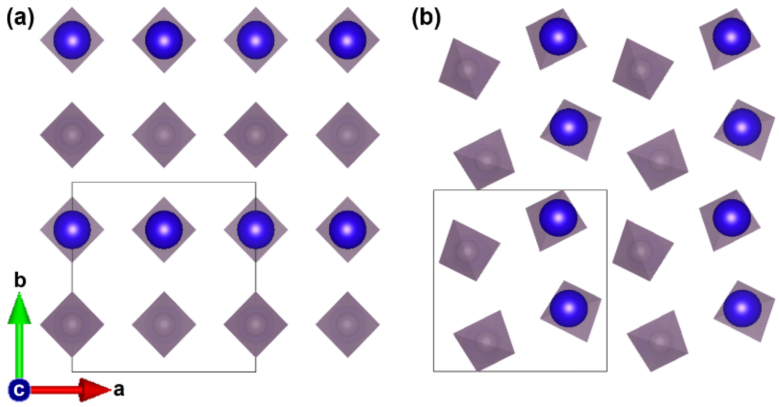

Figure 3.1 [001] views of the (a) xenotime and (b) monazite phases of dysprosium orthophosphate, $DyPO_4$. Violet spheres represent Dy^{3+} cations, grey tetrahedra represent PO_4 groups, and the boxes represent one unit cell. The apparent 90° rotation of monazite with respect to xenotime is merely a result of monazite's monoclinic cell setting.

Most xenotime $REPO_4$ transitions have been extensively investigated using *in situ* diamond anvil cell (DAC) Raman spectroscopy (RS) and x-ray diffraction (XRD) techniques. For $TbPO_4$, Tatsi et al.'s RS study reported a high-pressure polymorph that was likely monazite [17]. López-Solano et al.'s XRD study then confirmed that this polymorph was of the monazite structure and provided detailed structural information including an equation of state (EOS) for both polymorphs [11]. Gomis et al.'s single-crystal XRD work showed that $HoPO_4$ and $TmPO_4$ transition to the monazite structure and gave elastic constants and an EOS for each material in the xenotime phase [19]. Lacomba-Perales et al.'s synchrotron XRD study showed the xenotime-monazite transition in $ErPO_4$ and YPO_4 and gave an EOS for both polymorphs [11]. However, all xenotime compositions do not transition to monazite; Zhang et al. reported that $YbPO_4$, $LuPO_4$, and $ScPO_4$ transition to the scheelite (tetragonal, $I4_1/a$) structure [12, 13].

Similar insight into the high-pressure phase behavior of $DyPO_4$ has yet to be reported, though significant steps have been taken. Using *in situ* DAC RS, Musselman et al. and Stavrou et al. reported $DyPO_4$ transition onset pressures (P_{onset}) of 15.3(9) GPa and 13 GPa, respectively [20, 21]. They both attribute emergent Raman peaks at these pressures to a polymorph that takes on the monoclinic, monazite structure. Musselman et al.'s

determination is based on peaks emerging at locations consistent with monazite $TbPO_4$ peaks. Stavrou et al. further claim that monazite $DyPO_4$ transforms to scheelite at higher pressures around 30 GPa. This xenotime-monazite-scheelite transition pathway is consistent with that of neighboring xenotime $REPO_4$s [21]. Other ABO_4 compounds like alkaline-earth phosphates are stable in the monazite structure up to at least 30 GPa [11]. Very recently, Heuser et al. synthesized metastable $DyPO_4$ in the monazite structure [8]. While literature on the xenotime and monazite $DyPO_4$ polymorphs exists, the fundamental thermodynamics and kinetics of the transition are not fully established.

Moreover, the impact of hydrostaticity on the onset of the $DyPO_4$ transition has yet to be reported. It is well-documented that higher shear components often lower P_{onset} and Lacomba-Perales et al. came to similar conclusions when comparing their YPO_4 findings to previous work [11, 47]. Although the effect of hydrostaticity has yet to be systematically studied for $REPO_4$s, it has been studied in other ABO_4 compounds. For example, Santamaría-Pérez et al. conducted a systematic study for orthorhombic $BaSO_4$ [22]. Under less hydrostatic conditions, they found that transition began earlier and that the pressure range of phase coexistence was wider. Assessing the impact of hydrostaticity on the $DyPO_4$ transition is critical as structural applications like CMCs involve a significant degree of deviatoric stress in addition to hydrostatic pressure.

This study employs *in situ* DAC synchrotron XRD to directly and quantitatively interrogate the $DyPO_4$ structure and phase behavior. To apply pressure with varying degrees of hydrostaticity, three pressure-transmitting media (PTMs) are used: neon, a 16:3:1 methanol-ethanol-water mixture, and the soft salt KCl. Diffraction patterns are used to determine P_{onset}, calculate axial compressibilities, and develop EOS's for the xenotime and monazite phases. Our findings show a quasi-hydrostatic P_{onset} of 9.1(1) GPa – much lower than the previously reported RS-based value of 15.3(9) GPa [20]. In addition, deviatoric stresses induced by the solid PTM, KCl, trigger an even earlier $DyPO_4$ transition at least as low as 7.0 GPa. Independent of hydrostaticity (i.e., with all PTMs

used here), experiments reveal a wider pressure range of xenotime-monazite coexistence than was indicated by RS, suggesting that this transition is kinetically limited. Axial data from the quasi-hydrostatic experiments show that $DyPO_4$'s response to pressure is anisotropic. 3rd order Birch-Murnaghan EOS fits yield a xenotime bulk modulus (B0,X) of 144(1) GPa with a pressure derivative of 4 and monazite bulk modulus (B0,M) of 180(11) GPa with a pressure derivative of 4.

3.5 Experimental Details

Phase-pure xenotime $DyPO_4$ powder is obtained via precipitation reaction involving $Dy(NO_3)_3 \bullet 5H_2O$ ($\geq$99.9% RE oxide basis, Alfa Aesar) precursor and H_3PO_4 (85% w/w aqueous solution, Alfa Aesar) and subsequent calcination. Details of these two steps are described elsewhere [16]. *In situ* DAC XRD is conducted at room temperature at beamline 16-ID-B, HPCAT, Advanced Photon Source, Argonne National Laboratory. For all experiments, 301 stainless steel gaskets are drilled with the HPCAT laser micro-machining system [55] and two-dimensional diffraction patterns are collected with the PILATUS 1M-F detector. The x-ray beam spot size (full width at half maximum) is approximately 4 µm (vertical) by 6 µm (horizontal). These experiments are conducted over two synchrotron beam trips, resulting in slight differences in experimental details (such as beam wavelength). These details as well as experimental details of the DACs used are listed in Table 3.1.

Table 3.1 Experimental details for each of the three PTM experiments.

PTM	Beam λ (Å)	No. Scans	Exposure time (s)	Loading rate (MPa/s)	Pressure marker	Gasket hole thickness, diameter (μm)	Culet diameter (μm)	DAC type	P_{max} (GPa)
Neon	0.48595	74	1	1.8	gold powder	∼40, ∼110	250	symmetric	14.8
Mixture	0.40663	26	5	1.1	ruby chips	110, 250	500	Almax easyLab plate	14.2
KCl	0.40663	16	7.5	1.6	ruby chips	68, 180	380	Almax easyLab plate	12.6

Diamond anvil cell preparation involves loading the $DyPO_4$ powder sample and the pressure marker (Au or ruby) into the gasket chamber. Great care is taken that the sample does not bridge the anvils or gasket walls for best hydrostatic conditions. Three different PTMs are used: neon, 16:3:1 methanol-ethanol-water mixture, and KCl. The 16:3:1 methanol-ethanol-water mixture is hereafter referred to as the "mixture." In the case of KCl and the mixture, after a ruby is added to the sample, the PTM is added and the cell is closed and sealed. In the neon experiment, neon gas is loaded using the GSECARS gas membrane loading system [56]. The cell is then set up with a dual membrane system for (de)compression rate control [48]. Adding the can assembly for membrane compression to the already gas-loaded cell resulted in an inadvertent initial pressure jump to ∼4 GPa prior to placing the cell on the beamline. There are no reported $DyPO_4$ phase transitions below ∼4 GPa (as corroborated by our mixture and KCl experiments); therefore, the initial jump in the neon experiment does not preclude any material insight. The beamline's PACE 5000 pressure controlling system is then used to pressurize the cell during the experiment [48]. Pressure is determined from the unit cell volume and 3rd order Birch-Murnaghan EOS of gold (>99.96% metals basis, Alfa Aesar) [45, 57].

The mixture and KCl PTM experiments use an Almax easyLab plateDAC (Almax easyLab Inc., Cambridge, MA) and ruby chips (Almax easyLab Inc., Cambridge, MA) as pressure markers. The cell is pressurized by manual crank and pressure is determined using ruby R1 fluorescence [58]. Other distinct experiment parameters are shown in Table 3.1. Pressures derived from ruby fluorescence are presented without error estimates as only nominal values are recorded. Although these two experiments use a different pressure marker than the neon experiment, any systematic error in pressure scales is likely minimal as the gold EOS used in this study was calibrated against the ruby fluorescence method [45]. In addition, the ruby scale used in this study was also used in Musselman et al.'s Raman study – ensuring pressure scale consistency with prior Raman work [20].

XRD pattern integration, masking, and background subtraction are performed using Dioptas [49]. Pattern fitting is then performed using X'Pert HighScore Plus [42]. This software fits monazite using the $P2_1/c$ cell setting as a default. Although both the $P2_1/c$ and $P2_1/n$ cell settings are valid descriptions of monazite (space group No. 14), fitted lattice parameters are converted to the $P2_1/n$ cell setting for ease of comparison to literature. The atmospheric-pressure volume of xenotime $DyPO_4$ is calculated from a synchrotron scan ($\lambda = 0.48595$ Å) at 0 GPa (prior to any compression) using a plate DAC with no PTM. $DyPO_4$'s zero-pressure bulk modulus (B_0) and its pressure derivative (B_0') are determined by fitting volume vs. pressure data to the 3rd order Birch Murnaghan EOS with the EOSFit7-GUI program [59]. Xenotime EOS and axial compressibility fits use scans with $P < P_{onset}$, while monazite EOS and axial compressibility fits use scans with $P \geq P_{onset}$. For all other computation involving derived data (e.g., unit cell volume, gold-based pressure, cell setting conversion), Python is used to propagate error and a covariance of 0 is assumed.

3.6 Results

All three experiments have similar quasi-static loading rates (see Table 3.1, Fig. C1) despite the varying mode of pressure application [60]. Thus, we do not attribute differences

among datasets to kinetic effects. The LeBail fitting approach is used instead of traditional Rietveld structure refinement to accommodate the significant preferred orientation present in all scans of all experiments (Fig. C2 illustrates a representative example) [50]. Preferred orientation appears (see Fig. C2) due to the small spot size of the beam with respect to the grain sizes of the present sample (sampling a finite number of grains) [60]. It is thus also observed for the neon loading despite the neon's better hydrostaticity. The xenotime, monazite, neon, and KCl structures used for pattern fitting were determined by Milligan et al., Heuser et al., Hemley et al., and Froyen et al., respectively[8, 61–63].

The zero-pressure xenotime unit cell volume ($V_{0,X}$) used for normalization in Figure 3.2 is 289.39(2) $Å^3$. The dashed lines show $DyPO_4$ P_{onset} values of 9.1(1) GPa, 9.3 GPa, and 7.0 GPa when pressurized with the neon, mixture, and KCl PTMs, respectively.

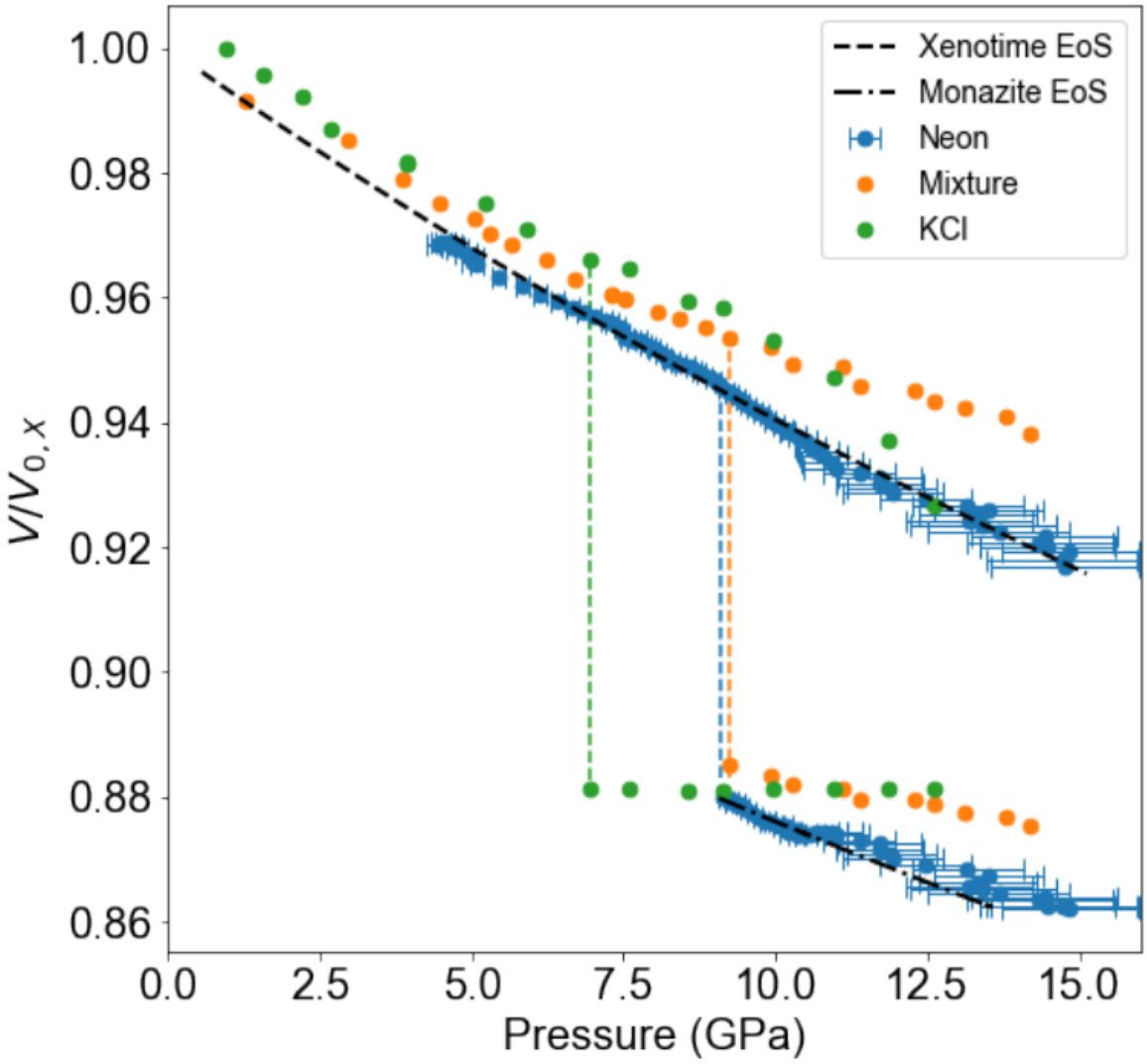

Figure 3.2 $DyPO_4$ unit cell contraction during compression under neon, mixture, and KCl PTMs. Volumes are normalized by the xenotime volume at 0 GPa, $V_{0,X}$ (in which 'X' denotes 'xenotime'). Vertical dashed lines indicate P_{onset}. For each PTM, the cluster at the top of the dashed line represents xenotime while the cluster at the bottom of the dashed line represents monazite. Error bars represent standard deviation. In mixture and KCl datasets, pressure was recorded as a nominal value. Volume error bars for all datasets are within the symbols. Black dashed curves represent EOS fits of neon data performed with a fixed bulk modulus pressure derivative (see Table 3.2).

The respective $DyPO_4$ volume contractions at P_{onset} are 6.96(3)%, 7.17(3)%, and 8.75(3)%. Figure 3.3, Figure 3.4, and Figure 3.5 show that all XRD peaks drift to higher Q and become more diffuse due to uniform and non-uniform strain, respectively. Transformation onset is determined by visual inspection of individual XRD patterns (see Fig. C3), not by judging color in the following contour plots (Figure 3.3a, Figure 3.4a, and Figure 3.5a) [60]. Visual inspection involves plotting the square root of intensity against Q to ensure that emerging peaks are not overlooked due to their extremely low intensity. Any given pattern is fit with both the xenotime and monazite phases only when visual inspection of that pattern reveals intensity at Q values consistent with monazite peaks. In the neon experiment, the (110), (002), and $(02\bar{1})$ monazite peaks are used to mark P_{onset} as they are the first monazite peaks to emerge and do not overlap with xenotime signal. In the mixture and KCl experiments, the (002) peak does not appear because of variation in preferred orientation between experiments. Therefore, only the (110) and $(02\bar{1})$ monazite peaks are used to mark P_{onset} in these experiments as shown in Figs. C3(b) and C3(c). All expected xenotime peaks appear in low-pressure patterns and persist after P_{onset} for all experiments. In addition, all major monazite peaks are observed at high pressure. Minor monazite peaks at $Q > 3$ $Å^{-1}$ are more difficult to verify as they often overlap with each other or stronger PTM, pressure marker, or xenotime peaks.

Figure 3.3(a) and Figure 3.3(b) show XRD pattern evolution and LeBail fit quality (at $P_{initial}$, P_{onset}, and P_{final}), respectively, in the neon experiment. The first scan in this experiment is at a modestly high pressure of 4.4 GPa due to the gas membrane can setup and features xenotime and gold (circles in Figure 3.3(a)) peaks. Non-xenotime peaks first emerge at 5.0 GPa; this corresponds to the crystallization of neon as reported in in the literature [64]. This is noteworthy as the conditions shift from hydrostatic (in liquid Ne) to quasi-hydrostatic (in solid Ne) at this point in pressure.

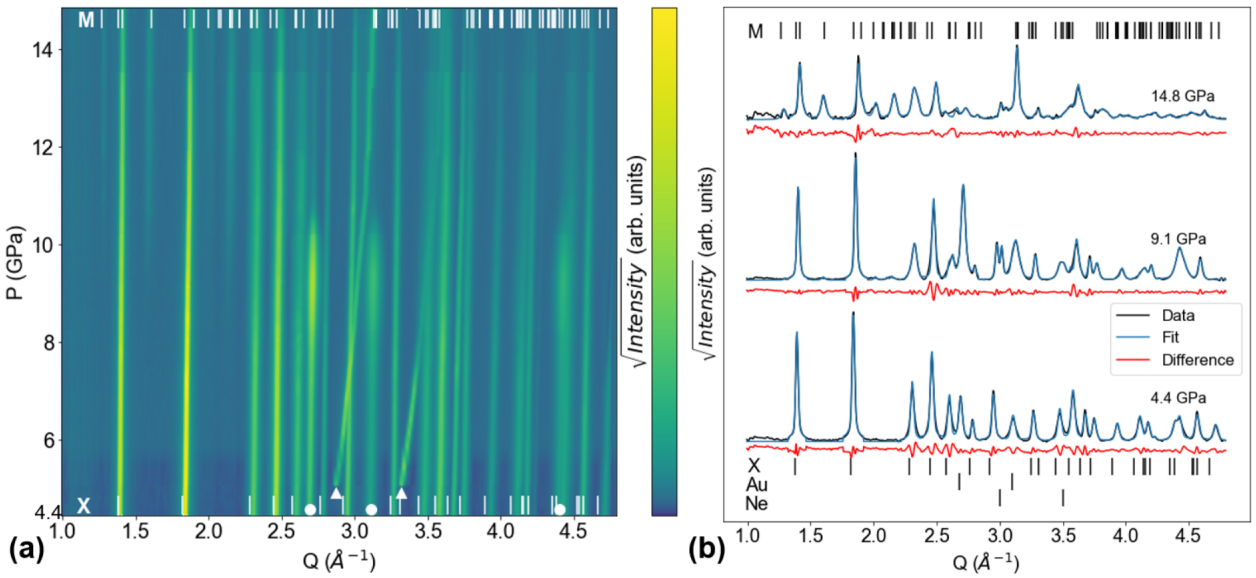

Figure 3.3 Neon dataset. 'X' ticks show a low-pressure xenotime reference pattern [61], while the 'M' ticks show a monazite fit. (a) Contour plot showing all XRD patterns. Monazite peaks emerge at 9.1(1) GPa. Circles and triangles denote the gold and neon peaks, respectively. (b) Select XRD patterns (initial, transition onset, final) and their LeBail fits.

Neon peaks shift more dramatically than the other materials' peaks because neon is the most compressible material in the DAC [62]. The first discernible monazite peaks emerge at 9.1(1) GPa and are located at Q = 1.59 Å^{-1}, 2.02 Å^{-1}, and 2.14 Å^{-1}; these are the (110), (002), and (02$\bar{1}$) reflections, respectively. In the P_{onset} scan, the refined monazite lattice parameters are a = 6.150(1) Å, b = 6.627(1) Å, c = 6.384(1) Å, and β = 99.60(1)°. Note that around 10 GPa, the gold signal becomes extremely weak, likely due to gold grains shifting out of the beam spot following the onset of the xenotime to monazite transition. In addition, the weak gold peaks start to overlap with stronger xenotime and now-solidified neon peaks. This overlap makes precisely locating the gold peak much more difficult. As a result, the uncertainty in the fitted gold lattice parameter increases dramatically. Since pressure is determined as a function of gold lattice parameter, the pressure uncertainty also increases dramatically.

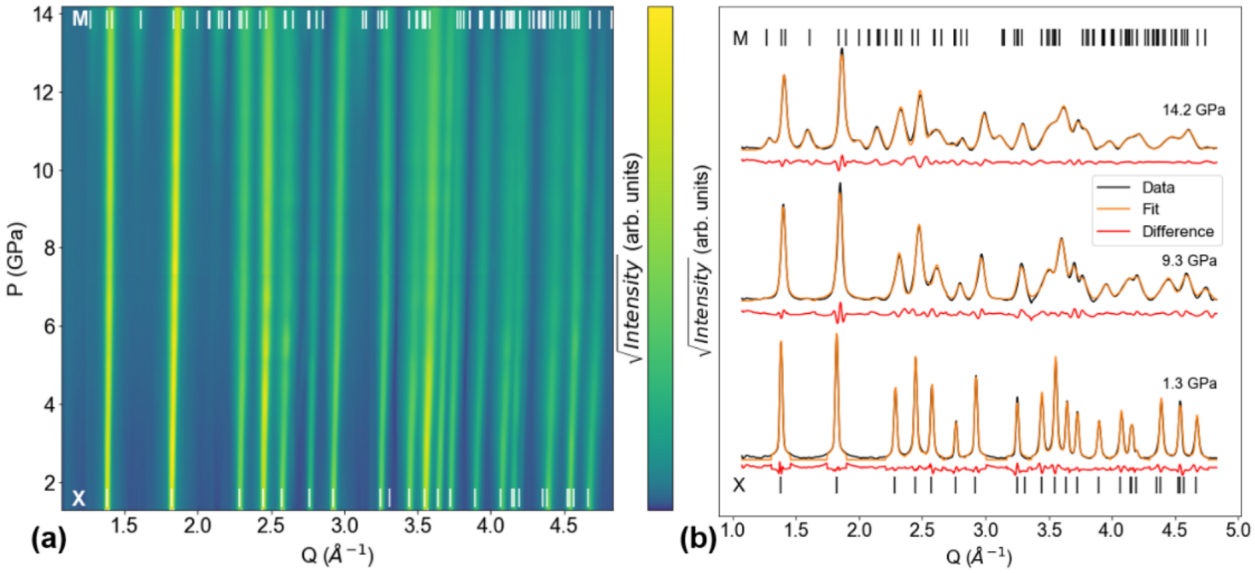

Figure 3.4 Mixture dataset. 'X' ticks show a low-pressure xenotime reference pattern [61], while the 'M' ticks show a monazite fit. (a) Contour plot showing all XRD patterns in ramp. Monazite peaks emerge at 9.3 GPa. (b) Select XRD patterns (initial, transition onset, final) and their LeBail fits.

Figure 3.4(a) and Figure 3.4(b) show XRD pattern evolution and LeBail fit quality (at $P_{initial}$, P_{onset}, and P_{final}), respectively, in the mixture experiment. The first scan at 1.3 GPa only shows xenotime peaks as the mixture PTM remains a liquid at this pressure and is indiscernible. The first discernible monazite peaks emerge at 9.3 GPa; these are located at Q = 1.59 Å^{-1} and 2.13 Å^{-1} and correspond to the (110), and (02$\bar{1}$) reflections, respectively. In the P_{onset} scan, the refined monazite lattice parameters are a = 6.159(1) Å, b = 6.611(1) Å, c = 6.425(1) Å, and β = 99.50(1)°. It is noteworthy that this transition commences prior to the freezing of the mixture; this means the mixture remains hydrostatic at P_{onset}. At ∼10.5 GPa (the mixture's effective hydrostatic limit), the mixture undergoes a glass transition into an amorphous solid phase that contributes no XRD peaks [46].

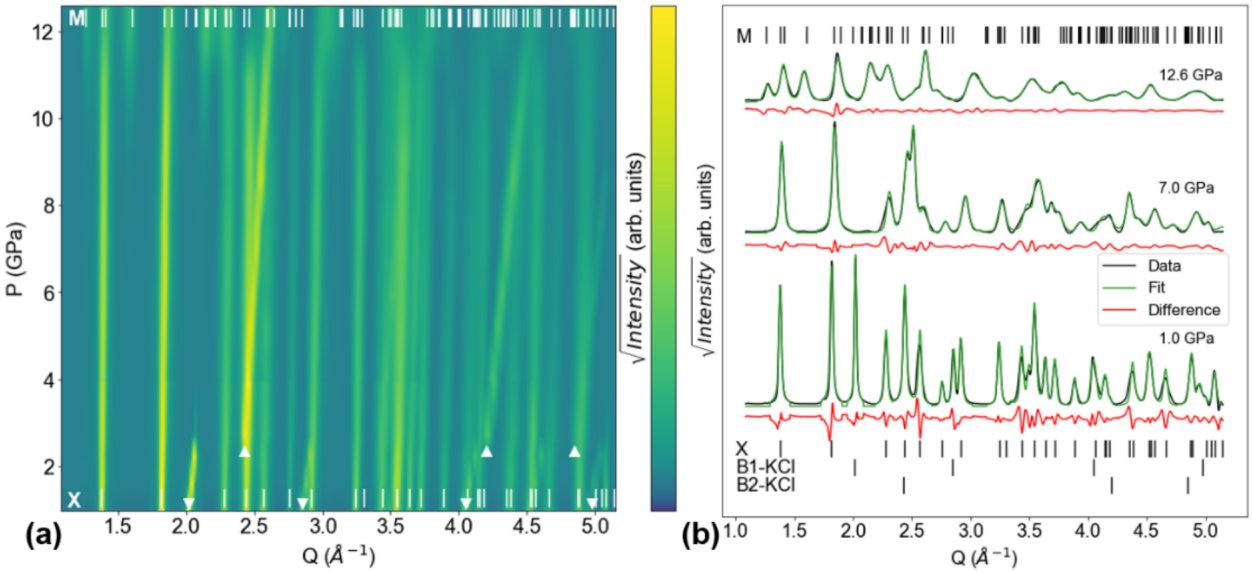

Figure 3.5 KCl dataset. 'X' ticks show a low-pressure xenotime reference pattern [61], while the 'M' ticks show a monazite fit. (a) Contour plot showing all XRD patterns in ramp. Inverted and upright triangles represent the B1 and B2 phases of KCl, respectively. Monazite peaks emerge at 7.0 GPa. (b) Select XRD patterns (initial, transition onset, final) and their LeBail fits.

Figure 3.5(a) and Figure 3.5(b) show XRD pattern evolution and LeBail fit quality (at $P_{initial}$, P_{onset}, and P_{final}), respectively, in the KCl experiment. The first scan shows peaks from xenotime $DyPO_4$ and B1-KCl (inverted triangles), which takes on a NaCl-type structure. At ∼2.7 GPa, B1-KCl transitions to B2-KCl (upright triangles), taking on a CsCl-type structure [63].

The KCl transition does not seem to affect the phase behavior of $DyPO_4$ in the KCl transition regime. Both sets of KCl phases' peaks have higher slope than $DyPO_4$'s peaks because both KCl phases are more compressible than $DyPO_4$ [63]. In marked contrast to the neon and mixture experiments, the first discernible monazite peaks emerge early at 7.0 GPa and are located at Q = 1.58 Å^{-1} and 2.12 Å^{-1}; these are the (110) and (02$\bar{1}$) reflections, respectively. In the P_{onset} scan, the monazite lattice parameters are a = 6.165(1) Å, b = 6.6673(5) Å, c = 6.407(1) Å, and β = 101.842(3)°. Although these uncertainties appear quite small, several checks on the LeBail fits did not change the outcome.

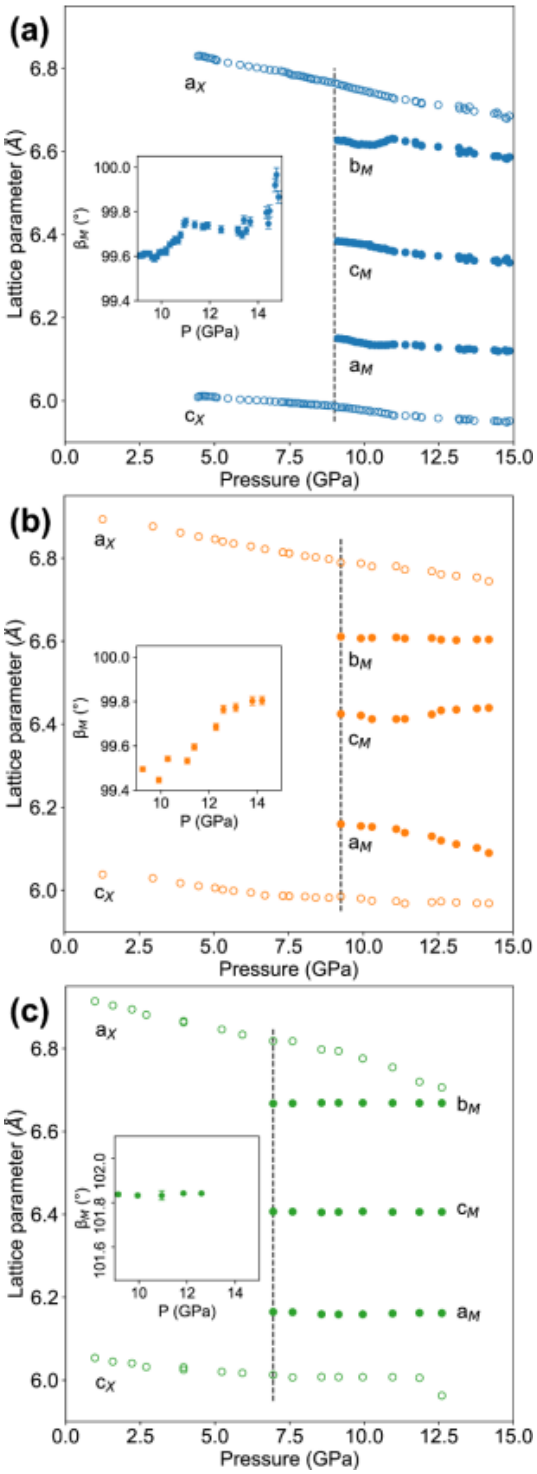

Figure 3.6 Pressure dependence of xenotime and monazite lattice parameters from the (a) neon, (b) mixture, and (c) KCl datasets. Dashed lines indicate P_{onset}. Lattice parameter error bars are within the symbol size. Insets show the monazite beta angle with standard deviation error bars. Across PTMs, consistent y-axis ranges for the panels and for the insets enable slope comparison.

Figure 3.6 plots the $DyPO_4$ lattice parameters from the LeBail fits for all three PTMs. Xenotime lattice parameters (a_X and c_X) steadily decrease during loading and have no apparent discontinuity or change in slope at P_{onset} across all PTMs. Monazite lattice parameters (a_M, b_M, c_M, and β_M) are less sensitive to pressure than xenotime parameters and the differences among the values of a_M, b_M, c_M are roughly the same across PTMs. β_M (shown in Figure 3.6 insets) spans similar ranges in the neon and mixture datasets but spans a much higher and tighter range in the KCl dataset. Contrary to xenotime trends, monazite lattice parameter trends have some slight but statistically significant irregularities. Soon after P_{onset} in the neon dataset (Figure 3.6(a)), a_M and b_M experience temporary dips and β_M experiences a temporary bump. After ∼10 GPa in the mixture dataset (Figure 3.6(b)), the a_M trend becomes steeper and the b_M and c_M trends become non-monotonic. It is also notable that the monazite unit cell volume does not contract upon compression in the KCl dataset – consistent with a high shear component present in the experiment.

3.7 Discussion

This study clearly shows that $DyPO_4$ transitions directly from the xenotime (tetragonal, $I4_1/amd$) to the monazite (monoclinic, $P2_1/n$) polymorph with no intermediate phase regardless of PTM. This result differentiates $DyPO_4$ from neighboring $REPO_4$ compositions (e.g., $TbPO_4$ and $Gd_xDy_{1-x}PO_4$), which exhibit an intermediate anhydrite phase [7]. No errant XRD peaks are observed in this study and forcing an anhydrite phase into the LeBail fits worsens fit quality. Moreover, Hay et al.'s revised Bastide stability diagram shows that $DyPO_4$ is too far from the xenotime-anhydrite-monazite triple point [7]. Once the monazite polymorph commences nucleation, there is a notably large pressure range of xenotime-monazite coexistence for all PTMs. In fact, the upper limit of the pressure range of coexistence remains unknown as the xenotime signal is still present in the final (highest pressure) scans taken herein. Phase fraction estimates from Rietveld refinements (see Fig. C6) show that KCl promotes more

significant monazite formation than neon and the mixture in addition to lowering the onset pressure, providing evidence that shear lowers the barrier to phase transition or otherwise increases the transformation kinetics in this system [60]. Santamaría-Pérez et al.'s $BaSO_4$ study showed a wider coexistence range under less hydrostatic media [22], though different mechanisms and different transformation kinetics are expected in barite. Other $REPO_4$ compositions are also reported to have significant ranges of phase coexistence [11, 18]. This coexistence, however, violates Gibb's phase rule [65]. For a single-component system in which temperature is fixed and pressure is the only degree of freedom, only one phase is thermodynamically allowed to exist; therefore, the observation of a significant xenotime-monazite coexistence range even under hydrostatic conditions in this study and others suggests that the transition is kinetically limited. It would be interesting to consider future studies with variable ramp rate and at elevated temperature, but this is outside the scope of the current work.

Another significant finding is that the XRD-based P_{onset} of 9.1(1) GPa is far lower than RS-based values of 15.3(9) reported by a subset of the authors of this work [20] and 13 GPa reported by Stavrou et al. [21]. The large difference between RS- and XRD-based P_{onset} values is unexpected as the RS-XRD discrepancy in $TbPO_4$ (an adjacent composition) is just 0.3 GPa [17, 18]. Taking a closer look at Musselman et al.'s Raman spectra provides a likely explanation for this 6.2 GPa gap. In that study, P_{onset} is marked by the appearance of small, distinct Raman bands representing almost all of monazite's optical modes. These modes harden with increasing pressure. Extrapolating monazite mode linear fits to lower pressures reveals that most of these modes fall within the broad peaks of xenotime modes at ∼9 GPa (see Fig. C4) [60]. In other words, monazite Raman modes may exist in the ∼9 GPa spectrum as weak shoulders or weak tails of xenotime Raman modes, but the poor signal-to-noise ratio of RS prevents unambiguous interpretation of these weak features as monazite signal. Stavrou et al.'s high pressure RS study of $DyPO_4$ reports a xenotime-monazite P_{onset} of 13 GPa [21] and presumably suffers from the same peak

overlap; however, the underlying Raman spectra have yet to be published. Thus, RS is insufficient for the conclusive determination of transition onset in $DyPO_4$. Consequently, the P_{onset} of $DyPO_4$ can be revised down to this study's XRD-based value of 9.1(1) GPa. Such a revision is likely not necessary for other xenotime $REPO_4$s as they already have XRD-based P_{onset} values reported in literature [12, 13, 17–19]. The revised $DyPO_4$ P_{onset} also marks a significant deviation from the linear dependence of P_{onset} on RE ionic radius that is suggested in literature [7, 16]. This deviation opens the intriguing possibility that at some critical ionic radius (between those of Y^{3+} and Dy^{3+}), P_{onset} has a discontinuity – i.e., it drops from above 15 GPa to below 10 GPa.

Beyond determining P_{onset} for $DyPO_4$, we find that P_{onset} is considerably stress-state dependent, with non-hydrostaticity promoting earlier transition. Neon and the mixture yield similar P_{onset} values: 9.1(1) GPa and 9.3 GPa, respectively. The latter value can be safely understood as hydrostatic because it is lower than the mixture's hydrostatic limit (i.e., below its freezing point). The P_{onset} difference between these two experiments is marginal and may be due to the fact that they use different methods of pressure determination (the former via gold diffraction, the latter via ruby fluorescence). In contrast, the KCl experiment yields a P_{onset} of 7.0 GPa – a significant drop of $\sim$22%. This pressure may be even lower if the ruby pressure readings are systematically overestimated due to the non-hydrostaticity of the KCl PTM. Unlike the other PTMs, KCl is a crystalline solid at all pressures and induces non-negligible shear stresses on $DyPO_4$. This is relevant for $REPO_4$s as shown by Lacomba-Perales et al. who report that less hydrostatic conditions result in earlier transition in YPO_4 [11] and by Heffernan et al. who report interesting shear-induced behaviors in $GdPO_4$ [54]. Non-hydrostaticity promoting earlier $DyPO_4$ transition is also consistent with Santamaría-Pérez et al.'s work on orthorhombic BaSO4 and gives additional insight into the mechanism of the shear-induced lowering of P_{onset} as discussed later [22].

When evaluating lattice parameters in this study, it is critical to note that those of monazite are less accurate than those of xenotime – especially at pressures close to P_{onset} when the monazite signal is extremely weak. Weak monazite peaks located close to other weak monazite peaks or strong xenotime peaks can easily lead to improper LeBail fitting and introduce inaccuracy. Even in the final (highest pressure) scans of each experiment, the strongest monazite peak is weaker than the strongest xenotime peak. Despite this uncertainty, Figure 3.6 shows that across all three experiments, the monazite lattice parameters a_M, b_M, and c_M at P_{onset} are consistent. The KCl experiment's β_M angle, however, is $\sim$2.5° higher than that of neon and the mixture (which are in close agreement).

Furthermore, the lattice parameter trends seen in the monazite phase (see Figure 3.6) also exhibit some irregularities. Soon after P_{onset} in the neon experiment, a_M, b_M, and β_M trends show temporary non-monotonicity, which is attributed to inaccurate inferred pressures rather than anomalous $DyPO_4$ behavior. At this point in the experiment, the gold peaks became extremely weak and began to overlap with stronger xenotime and neon peaks (see Figure 3.3(a)). Resultant inaccuracy in the gold peak position then propagates directly to the determined pressures. In the mixture dataset (Figure 3.6(b)) at $\sim$10 GPa, the a_M trend becomes steeper and the b_M and c_M trends become non-monotonic. These irregularities coincide with the non-hydrostatic limit (10.5(5) GPa), at which point the mixture undergoes a glass transition. The KCl experiment (Figure 3.6(c)) shows no contraction of the monazite unit cell due to the rather non-negligible degrees of shear stress. This is typical of phase transitions in a high shear environment where a local drop in pressure occurs as a nucleus of the low-pressure polymorph transitions to the higher density, high-pressure polymorph. Since this localized drop will cause the transition to continue elsewhere in the sample in the absence of a hydrostatic PTM, the monazite unit cell is not expected to contract until all material is transformed.

Quantitative evaluation of these lattice parameters is further made difficult by the fact that literature does not provide lattice parameters of the high-pressure $DyPO_4$ polymorph.

The best comparison point presently available is López-Solano et al.'s *in situ* DAC diffraction study of $TbPO_4$, a neighboring composition of $DyPO_4$ [18]. Their work uses a different monoclinic cell setting than this work, thus their a_M is equivalent to our study's c_M and their c_M is equivalent to our study's a_M. This switch explains why they report a_M ¿ c_M, while Figure 3.6 here shows the opposite. All linear (a_X, c_X, a_M, b_M, and c_M) lattice parameters reported herein are ∼1% smaller than those reported by López-Solano et al., which is expected since Dy^{3+} has a smaller ionic radius than Tb^{3+}. The monazite beta angle (β_M) reported herein is ∼3% smaller in the neon and mixture experiments and ∼1% smaller in the KCl experiment. Like $TbPO_4$, linear lattice parameters of $DyPO_4$ decrease with pressure while β_M increases under quasi-hydrostatic loading. Another important structural metric is tetragonal distortion (c_X/a_X), which is plotted against pressure in Fig. C5 [60]. The magnitude and pressure dependence of tetragonal distortion in the neon and mixture experiments is in good agreement with the $TbPO_4$ study – suggesting that xenotime $DyPO_4$ and xenotime $TbPO_4$ distort similarly under quasi-hydrostatic loading. Both of those PTMs do not yield as great of an increase in tetragonal distortion as KCl does for the same pressure range – indicating KCl distorts xenotime $DyPO_4$ the most. A more thorough method of assessing unit cell distortion for both xenotime and monazite is evaluating axial compressibilities (summarized in Table C1) [60]. Analyzing relative values of axial compressibilities for a given phase provides insight into a material's (an)isotropic response to stress. It is important to note beforehand that xenotime axial compressibilities are more accurate than monazite ones due to signal-to-noise ratio deterioration under high pressure. Heffernan finds that xenotime axial compressibilities follow the order "$[001] \ll [010] = [100]$," while monazite axial compressibilities follow "$[100] < [010] < [001]$" [54]. Xenotime data from all three experiments as well as monazite data from the neon experiment match these trends. The mixture monazite data is not consistent because the b and c parameters no longer decrease monotonically past the hydrostatic limit. KCl's monazite data is inconsistent because the lattice parameters appear pressure-independent

(i.e., the a_M, b_M, and c_M axial compressibilities are virtually 0 GPa^{-1}). This also explains why the qualities of fit for KCl monazite data (also in Table C1) are extremely poor [60]. Axial compressibility fits also provide zero-pressure parameters (y-intercepts of the linear fits), which should be consistent with the 1 atm lattice parameters in the structure files used for LeBail fitting. Xenotime zero-pressure parameters are consistent in this respect, while monazite zero-pressure parameters are not. Monazite's inconsistency may be due to an insufficient pressure range of monazite data points, aforementioned pressure-induced degradation of the XRD signal, or the metastability of the monazite $DyPO_4$ structure used as a reference in this study [8].

P-V data is fit to the 3rd order Birch-Murnaghan EOS to explore the thermodynamics of the transition and permit comparison to elastic properties measured through other methods. EOS parameters are listed in Table 3.2 and plots with EOS fits are shown in Fig. C7 [60].

Table 3.2 Bulk moduli (B_0) and their zero-pressure derivatives (B_0') calculated by fitting volume vs pressure data to the 3rd order Birch-Murnaghan EoS. The fits themselves are plotted in Fig. C7 [60]. The weighted chi square value (χ^2_w) is the measure of goodness of fit. Fits were performed by fixing B_0' to 4 or by letting it float between 2 and 7. Numbers in parentheses after a value represent the standard deviation of the last digit of the value. The xenotime V_0 values marked with an asterisk are fixed during fitting. KCl monazite fits do not converge.

Phase	PTM	$B_0' = 4$			$2 \leq B_0' \leq 7$			
		V0 (Åˆ3)	B_0 (GPa)	χ^2_w	V0 (Åˆ3)	B_0 (GPa)	B_0'	χ^2_w
Xenotime	Neon	289.39(2) *	144(1)	0.05	289.39(2) *	135(1)	7.0(1)	0.03
	Mixture	289.39(2) *	170(1)	0.03	289.39(2) *	163(6)	6.4(20)	0.03
	KCl	289.39(2) *	204(18)	154.86	289.39(2) *	209(17)	2.0(40)	152.90
Monazite	Neon	266.57(70)	180(11)	0.96	267.02(75)	163(9)	6.4(22)	0.93
	Mixture	261.45(51)	421(33)	5.60	261.71(55)	389(33)	7.0(7)	4.91
	KCl	-	-	-	-	-	-	-

Two sets of fits are performed in all cases, one with B_0' fixed to 4 and one with B_0' floating between 2 and 7. Xenotime fits fix $V_{0,X}$ to 289.39(2) $Å^3$, which is derived from a pre-compression synchrotron scan. In monazite fits, fixing $B_{0,M}$ to Heuser et al.'s reported value of 273.630(5) $Å^3$ [8] – as well as similar values reported by others [66–68] – leads to

$B_{0,M}$ being lower than $B_{0,X}$. Such a finding would be inconsistent with the axial compressibility analysis performed herein, as well as prior high pressure $REPO_4$ XRD studies reporting $B_{0,M}$ to be ∼20% greater than $B_{0,X}$ in $ErPO_4$, ∼28% greater in YPO_4, and ∼6% greater in $TbPO_4$ [11, 18]. Previously reported $DyPO_4$ $V_{0,M}$ values likely result in this inconsistency because they are based on metastable monazite $DyPO_4$ synthesized or simulated at 1 atm. Therefore, $V_{0,M}$ is made a free parameter in the monazite fits shown in Table 3.2.

For the xenotime polymorph, χ^2_w values show that the neon dataset yields qualities of fit that are similar to those of the mixture dataset and dramatically better than those of the KCl dataset (for both B_0' conditions). Among the neon- and mixture-based fits, the neon-based, fixed B_0' fit has the best quality (χ^2_w closest to 1) and yields a $B_{0,X}$ value that is comparable to values determined using other techniques. Namely, Wilkinson et al. report a 122-141 GPa range using values converted from nanoindentation data and Li et al. report 141.5 GPa using computational chemical bond theory [69, 70]. Furthermore, $B_{0,X}$ = 144(1) GPa with B_0' = 4 is consistent with $REPO_4$ compositional trends. Even the floating B0'-based $B_{0,X}$ is between the reported $B_{0,X}$ values of $TbPO_4$ and $HoPO_4$ (the left and right lanthanide neighbors of $DyPO_4$, respectively), which are 134 GPa (B_0' = 6.4) and 152 GPa (B_0' = 4.2), respectively [18, 19].

In marked contrast, the mixture and KCl datasets give B_0 values that are far too high. On one hand, the KCl dataset's exceedingly high B_0 values are consistent with Lacomba-Perales et al.'s observations that non-hydrostatic DAC experiments on $REPO_4$s yield overestimated moduli [11]. On the other hand, the mixture dataset's high B_0 values cannot be explained by non-hydrostatic stress since the mixture remains hydrostatic up to ∼10.5 GPa. We suggest that this inconsistency may be due to the fact that a sprinkling of Au powder was used for pressure measurement in the neon experiment, while a ruby sphere was used in the mixture and KCl experiments. While the Au powder experienced the same (quasi-)hydrostatic conditions as the sample in the neon experiment, the ruby may have

become trapped between the gasket and anvil in the mixture and KCl experiments. Trapping may have led the ruby to experience higher shear, resulting in a somewhat incorrect pressure reading. This explanation may be supported by close inspection of Figs. C7(c) and C7(e), which show that the xenotime EOS fits switch from lying below the experimental data to lying above the experimental data at ∼5 GPa. Considering these issues as well as the neon data's close match with literature values as discussed above, we regard the fixed B_0' fit of the neon data as most accurate.

For the monazite polymorph, the neon dataset again yields the best fits (for both B_0' conditions) as evidenced by the respective χ^2_w values being closer to 1. The mixture dataset is significantly underfit and most of its data points are located at pressures above the mixture's hydrostatic limit (see Fig. C7(d)) [60]. In the mixture experiment, a similar behavior as in the KCl experiment is expected. That is, local pressure drops during non-hydrostatic compression introduce error into the fitted EOS (which naturally includes pressures above 9.3 GPa for the high-pressure polymorph). The KCl monazite dataset (see Fig. C7(f)) does not produce any converging fits because $B_{0,M}$ becomes negative during optimization cycles [60]. Taking a step back, this dataset should not yield reasonable 3rd order Birch-Murnaghan fits as the monazite phase is not compressed under these non-hydrostatic conditions until the entire sample volume has transitioned. Among the two neon dataset-based fits, we select the fit conducted with a fixed B_0' to have a consistent B_0' condition with the selected xenotime EOS. Therefore, we report a monazite $DyPO_4$ bulk modulus of 180(11) GPa (B_0' = 4) and a zero-pressure volume of 266.57(70) Å^3. This ∼25% increase from $B_{0,X}$ to $B_{0,M}$ appears consistent with the aforementioned increases in other compositions. Evaluating the value of $B_{0,M}$ itself is made difficult by the fact that no experimental comparison exists in literature – only Kowalski et al.'s ab initio quantum chemistry calculation of 127.6 GPa [71]. This simulated value is far lower than the $B_{0,M}$ values in Table 3.2 and even lower than the $B_{0,X}$ values reported here and elsewhere in literature [69, 70]. As aforementioned, one would expect $B_{0,M}$ to be higher than $B_{0,X}$ for

such $REPO_4$s, as indeed is observed here. Thus, Kowalski et al.'s value appears underestimated for reasons yet unknown.

It may be tempting to conclude that the neon-based $B_{0,M}$ values are as accurate if not more accurate than the neon-based $B_{0,X}$ values; however, this is not the case for two reasons: first, the $V_{0,M}$ of stable (not metastable) monazite $DyPO_4$ must be ascertained with further high pressure XRD experiments as this parameter has a tremendous influence on the fitted $B_{0,M}$ value. Second, even if this neon monazite data is fit using the most accurate $V_{0,M}$, $B_{0,M}$ would still be less accurate than $B_{0,X}$ due to the coexistence of xenotime and monazite phases in all scans above P_{onset}. In other words, all scans used for xenotime EOS fitting only contain xenotime, whereas all scans used for monazite EOS fitting contain both phases.

Next, we consider the mechanism of the lowered P_{onset} due to high shear in more depth. Heffernan et al. elucidate the role of shear in $REPO_4$s' structural response to pressure in their in situ DAC study of monazite $GdPO_4$ [54]. They observe an additional $GdPO_4$ Raman band appearing at pressures above their PTM's hydrostatic limit even though XRD suggests no such transition. The authors attribute this additional mode to shear-induced PO_4 tetrahedra distortion, which exacerbates Gd-O bond distortion. Such a mechanism may also be responsible for the lower transition pressure of xenotime $DyPO_4$ in a KCl environment as we see here. That is, hydrostatic pressure may compress the Dy-O cage, but KCl-induced shear may further distort Dy-O bonds (indirectly) via PO_4 tetrahedral distortion. The magnitude of this shear may be sufficient to not only distort Dy-O bonds, but to reconfigure them – thus triggering the early transition. Our observation of the β_M angle being $\sim$2.5° higher in the KCl experiment than in the other experiments also points towards a possible shear-induced distortion of the monoclinic cell. Confirming this proposed mechanism will require future *in situ* DAC single crystal XRD studies. Nevertheless, it may be scientifically interesting as well as technologically important if modifying and controlling shear could lower P_{onset} even further.

Finally, our findings can inform future $REPO_4$ work and CMC fiber coating development more broadly. Given the large discrepancy between RS- and XRD-based P_{onset} values for $DyPO_4$, XRD should be considered for conclusive P_{onset} determination in $REPO_4$ solid solutions with similar Raman band overlap (e.g., $Gd_xDy_{1-x}PO_4$). All other pure xenotime $REPO_4$s – as well as $Gd_xTb_{1-x}PO_4$ and $Sm_xTb_{1-x}PO_4$ solid solutions – have already been characterized using XRD [11–13, 18], thus their reported transition pressures stand unaltered. Furthermore, the at least 22% reduction of $DyPO_4$ P_{onset} under KCl loading suggests that xenotime $REPO_4$ fiber coating transformation may begin at lower pressures than expected in the high-shear environment of a CMC. This in turn means that transformation-based plasticity and toughening mechanisms could be activated at lower stresses in the application environment. Therefore, a candidate material's propensity for transformation should be assessed under high-shear – in addition to hydrostatic – conditions. Using shear-sensitivity as a criterion for screening $REPO_4$ candidates potentially opens up a wider range of compositions worth considering for CMC applications.

3.8 Conclusion

This experimental study provides crystallographic proof that xenotime $DyPO_4$ transitions directly to the monazite structure upon room temperature compression. Prior Raman spectroscopy indicated a transition onset pressure of 15.3 GPa [20]; however, our synchrotron XRD study shows that transition onset is much earlier, at 9.1 GPa. All lattice parameters and their pressure dependences are consistent with the trends reported for the neighboring $TbPO_4$ composition. By employing neon, 16:3:1 methanol-ethanol-water, and KCl as PTMs, we also explore the effect of various levels of hydrostaticity on the phase behavior, finding that non-hydrostaticity reduces P_{onset} to at least as low as 7.0 GPa. Compared to the other PTMs, KCl causes the most rapid increase in the xenotime c/a ratio and yields the highest monazite β angle. These are both likely indicators of shear-induced structural distortion of the PO_4 tetrahedra, which may have triggered the

early phase transition. For all PTMs, xenotime and monazite coexist for large pressure ranges, suggesting that this transition is kinetically limited. Calculated axial compressibilities reveal the anisotropy of $DyPO_4$'s response to stress and are consistent with expectations for $REPO_4$s in general. Our 3rd order Birch-Murnaghan EOS fits of (quasi-)hydrostatic data yield a xenotime bulk modulus of 144(1) GPa and a monazite bulk modulus of 180(11) GPa (both with B_0' fixed to 4). The findings presented herein provide additional insight into the pressure-induced transition in $DyPO_4$ and how this transition could be tailored to CMC fiber coating applications.

3.9 Acknowledgments

The authors thank Drs. Jesse Smith and Ross Hrubiak for performing initial alignments at the beamline, Dr. Sergey Tkachev for assisting with gas-loading samples, as well as Sarah Boardman and Yachao Chen for helping perform the beamline experiments. The authors also thank Drs. Nitin Kumar and Sina Soltanmohammed, who assisted in developing the batch-processing and batch-fitting procedures for the synchrotron data. This manuscript has been authored by UT-Battelle, LLC under Contract No. DE-AC05-00OR22725 with the U.S. Department of Energy. The United States Government retains and the publisher, by accepting the article for publication, acknowledges that the United States Government retains a non-exclusive, paid-up, irrevocable, world-wide license to publish or reproduce the published form of this manuscript, or allow others to do so, for United States Government purposes J.S. was supported by the Department of Defense (DoD) through the National Defense Science and Engineering Graduate (NDSEG) Fellowship Program. B.H. was supported by resources at the Spallation Neutron Source (SNS) and the High Flux Isotope Reactor (HFIR), DOE Office of Science User Facilities operated by the Oak Ridge National Laboratory (ORNL). This work was performed at HPCAT (Sector 16), Advanced Photon Source (APS), Argonne National Laboratory. HPCAT operations are supported by DOE-NNSA under Award No. DE-NA0001974 and DOE-BES under Award No. DE-FG02-99ER45775, with partial instrumentation funding

by NSF. Use of the COMPRES-GSECARS gas loading system was supported by COMPRES under NSF Cooperative Agreement No. EAR 11-57758 and by GSECARS through NSF Grant No. EAR-1128799 and DOE Grant No. DE- FG02-94ER14466. A.P.S. is supported by DOE-BES, under Contract No. DE-AC02-06CH11357. This research was funded by the National Science Foundation (NSF) under Award No.: DMR-1352499.

3.10 Supplementary Information

Supplementary information referenced in this manuscript is provided in Appendix C. Figures C1-C7: Additional XRD and Raman spectroscopy-based plots; Table C1: Axial compressibilities.

CHAPTER 4

PHASE TRANSFORMATION PATHWAY OF DYPO4 TO 21.5 GPA

Reproduced with permission from *Crystals* and co-authors (included in Appendix A).

Jai Sharma[1], Henry Q. Afful[1], and Corinne E. Packard[1]

[1]Colorado School of Mines, Golden, Colorado 80401, USA

This manuscript explores the phase evolution of $DyPO_4$ to pressures beyond those achieved in Chapter 3, as the Chapter 3 study did not go to high enough pressures to observe the end of the xenotime-monazite phase coexistence range. While this *in situ* DAC synchrotron XRD revealed, for the first time, the full xenotime-monazite phase coexistence range as well as the emergence of a post-monazite phase, which is likely scheelite. The xenotime-monazite-scheelite transformation pathway is consistent with observed and predicted pathways of compositional neighbors. This chapter includes an overview of the authors' contributions, a summary of the key findings and contributions of this work, and the full manuscript published in *Crystals* in February 2023 (https://doi.org/10.3390/cryst13020249).

4.1 Author Contributions

All authors were involved in performing beamline experiments. I designed the experiments, wrote the beamtime proposal, and performed all the data analysis presented in this manuscript, and I was the primary author of this work. Henry Afful (PhD student at Colorado School of Mines) contributed to the monazite literature search, and he and Dr. Packard contributed to the reviewing, and editing of this manuscript.

4.2 Scientific Advancements and Conclusions

The work presented in this chapter furthers understanding of the phase transformation pathway of $DyPO_4$ by going to higher pressures than the Chapter 3 study. XRD data in this chapter yields the first estimation of the xenotime-monazite phase coexistence range for $DyPO_4$ as well as the first experimental observation of the post-monazite phase of $DyPO_4$.

4.2.1 Key Findings

- The pressure range of the $DyPO_4$ xenotime-monazite phase coexistence is determined to be 7.6(15) GPa.
- A post-monazite $DyPO_4$ phase emerges at 13.9(10) GPa and likely adopts the scheelite structure.
- The $DyPO_4$ P_{onset} does not increase significantly when the loading rate is increased by an order of magnitude.

4.2.2 Key Contributions

- This study provides a figure updating the $REPO_4$ high pressure phase map previously published by Musselman et al. [20]. The new map in this study uses XRD-based data (given the short-comings of Raman spectroscopy discussed in Chapter 3) and uniquely shows phase coexistence ranges. This figure also shows visually how the xenotime-monazite P_{onset} does not decrease linearly with RE ionic radius.
- This work confirms the $DyPO_4$ xenotime-monazite phase transformation likely proceeds via a diffusional, nucleation and growth-based mechanism.
- This study reveals a new phase transformation and the phase coexistence behavior of $DyPO_4$ at previously untested pressures.
- This work suggests xenotime $REPO_4$s close to the xenotime-monazite phase boundary follow the xenotime-monazite-scheelite phase transformation pathway.

4.3 Abstract

Interest in the deformation behavior and phase transformations of rare earth orthophosphates ($REPO_4$s) spans several fields of science—from geological impact analysis to ceramic matrix composite engineering. In this study, the phase behavior of polycrystalline, xenotime $DyPO_4$ is studied up to 21.5(16) GPa at ambient temperature using *in situ* diamond anvil cell synchrotron X-ray diffraction. This experiment reveals a large xenotime–monazite phase coexistence pressure range of 7.6(15) GPa and evidence for the onset of a post-monazite transformation at 13.9(10) GPa to scheelite. The identification of scheelite as the post-monazite phase of $DyPO_4$, though not definitive, is consistent with $REPO_4$ phase transformation pathways reported in both the experimental and the computational literature.

4.4 Introduction

Rare earth orthophosphates ($REPO_4$s) are highly refractory and insoluble ceramics relevant to various research areas ranging from geoscience to structural ceramics [1]. Much of the world's rare earth element supply comes from naturally occurring xenotime and monazite minerals, whose properties and formation are of great relevance in geochronology and geothermobarometry in addition to mineral extraction [2, 72]. The pressure-induced phase transformations of certain $REPO_4$ compositions have also spurred research toward their use as fiber coatings, where they can confer additional plasticity and toughening mechanisms to oxide–oxide ceramic matrix composites [7, 14, 15]. At ambient pressure ($\sim 10^{-4}$ GPa), $REPO_4$s adopt either the xenotime (tetragonal, $I4_1/amd$) or monazite (monoclinic, $P2_1/n$) structure. The xenotime structure is also referred to as "zircon" (based on $ZrSiO_4$); however, this study employs the former name because it specifically originates from YPO_4 minerals [1]. At high pressures, xenotime compositions transform into the monazite or scheelite (tetragonal, $I4_1/a$) structures (see Figure 4.1) [9].

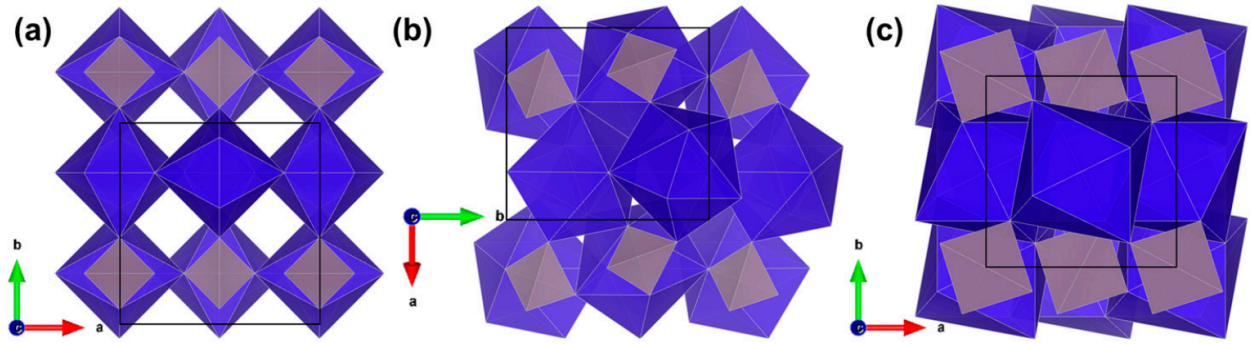

Figure 4.1 [001] views of $REPO_4$ structure in the (a) xenotime, (b) monazite, and (c) scheelite phases. RE-O polyhedra are shown in violet, PO_4 tetrahedra are shown in grey, and the unit cell boundaries are shown as thin black boxes. The 90° rotation of monazite axes with respect to those of xenotime and scheelite is a result of the monoclinic cell setting of monazite, as shown in detailed transformation schemes reported by Hay et al. [5]. Structures are visualized using the VESTA software [73].

The scheelite-type structure has also been observed in other ABO_4 materials (e.g., tungstates, molybdates, vanadates, and arsenates) [74–76]. The $REPO_4$ xenotime, monazite, and scheelite structures feature chains of alternating PO_4 tetrahedra (shown in gray) and RE-O polyhedra (shown in violet) with RE-O coordination numbers of 8, 9, and 8, respectively.

Figure 4.1 shows that the $REPO_4$ structure becomes increasingly compact when transforming from xenotime to monazite to scheelite. This compaction can be attributed to increasing rotation and displacement of the RE-O polyhedra and resultant changes in the phosphate chain linkages (edge-sharing → corner-sharing) [76]. Although the exact unit cell volume losses during these transformations are composition-dependent, the loss associated with the xenotime → monazite transformation is significantly lower than that of the monazite → scheelite transformation [13]. This disparity likely emerges from the fact that the former transformation involves an increase in RE-O coordination (8 → 9), while the latter involves a decrease (9 → 8) [76]. An intermediate anhydrite (orthorhombic, Amma) phase has also been reported in certain xenotime compositions prior to the emergence of monazite when the xenotime composition is subject to high deviatoric

stresses (e.g., $TbPO_4$ [37]) or has a composition that is extremely close to the 1 atm ($\sim 10^{-4}$ GPa) xenotime–monazite phase boundary (e.g., $Gd_xTb_{1-x}PO_4$ [77]).

Prior studies and reviews have reported phase diagrams showing $REPO_4$ transformation pressures based on a variety of computational and experimental techniques [7, 21, 78–80]. Recent advancements in in situ diamond anvil cell (DAC) X-ray diffraction (XRD) experiments require updating the high-pressure $REPO_4$ phase map [11–13, 18, 19, 21, 81–83]. In contrast to Raman spectroscopy and ab initio calculations, XRD provides more direct, crystallographic proof of the existence of $REPO_4$ phases and phase transformations. Figure 4.2 compiles experimentally observed phase data from DAC XRD studies for all non-radioactive, single-RE compositions except $PrPO_4$, which has only been studied thus far using DAC Raman spectroscopy [84].

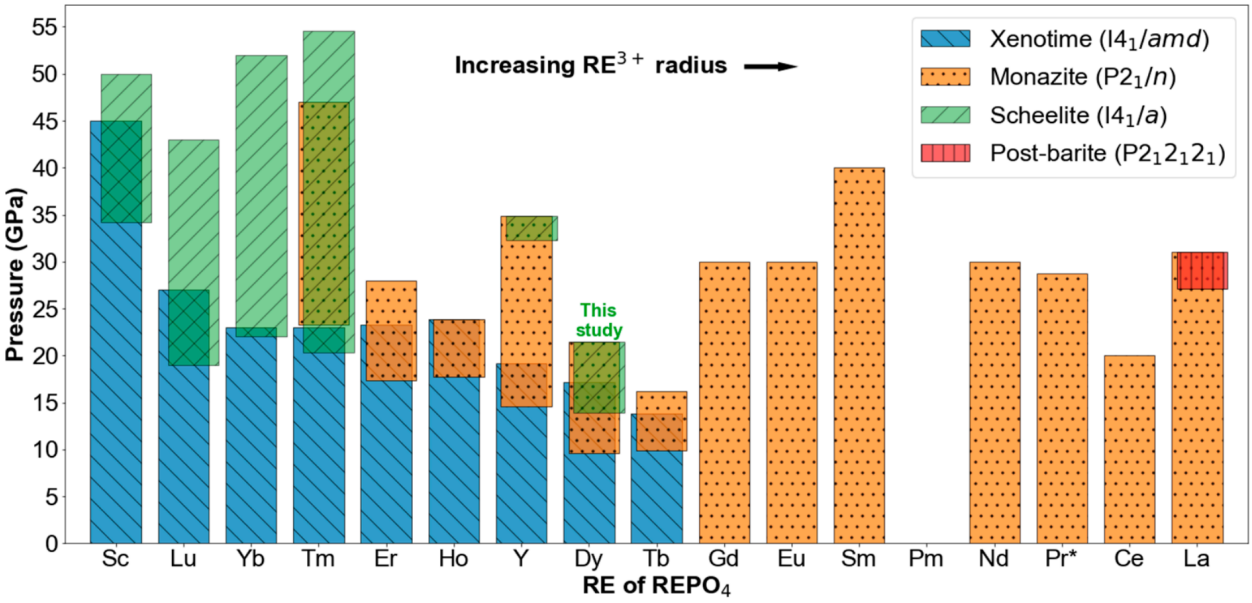

Figure 4.2 High-pressure phase map of the experimentally observed phases of all single-RE $REPO_4$s except $PmPO_4$ because Pm is both radioactive and extremely rare. The legend lists the phases with their corresponding space groups. For each composition, the upper limit of the highest bar(s) represents the highest pressure at which data are reported and does not represent a phase boundary. See text for references to the sources of phase data. All phase data are compiled from XRD studies except for $PrPO_4$, which has only been characterized via Raman spectroscopy * [84].

Under hydrostatic conditions, the xenotime → monazite transformation has been reported in $ErPO_4$, $HoPO_4$, YPO_4, $DyPO_4$, and $TbPO_4$ with onset pressures (P_{onset}) of 17.3 GPa, 17.7 GPa, 14.6 GPa, 9.1(1) GPa, and 9.9 GPa, respectively [11, 13, 18, 19, 81]. We note that for any number followed by a number in parentheses, the number in parentheses represents the standard deviation of the last digit of the number before the parentheses. In the $REPO_4$ phase transformation literature, there has long been an assumption that the xenotime → monazite P_{onset} varies linearly with RE3+ radius, such as many other properties of $REPO_4$s [7]. However, the $DyPO_4$ P_{onset} of 9.1(1) GPa from our 2021 study [81] disrupts this trend, suggesting instead that xenotime → monazite P_{onset} values fall into two clusters: a high-pressure one around ∼16 GPa ($ErPO_4$, $HoPO_4$, and YPO_4) and another that is <10 GPa ($DyPO_4$ and $TbPO_4$). Alloyed compositions of $Gd_xDy_{1-x}PO_4$ and $Gd_xTb_{1-x}PO_4$ also have transformation pressures that fall within the lower-pressure group, without following a trend with average RE^{3+} radius [7, 20, 77]. Neither thermodynamic properties (e.g., enthalpies of formation) nor structural properties (e.g., bond lengths and angles) show significant discontinuities between YPO_4 and $DyPO_4$, yet these compositions' P_{onset} values are known to differ by at least 5.5 GPa [9, 23, 68, 71, 85].

The xenotime → monazite transformation in $REPO_4$s has also been described as sluggish and kinetically limited due to the experimentally observed xenotime–monazite phase coexistence being inconsistent with thermodynamic expectations (i.e., Gibbs phase rule) [13, 18, 81]; this is shown in Figure 4.2 as the regions where blue and orange bars overlap. The xenotime–monazite phase coexistence ranges for $ErPO_4$, YPO_4, and $TbPO_4$ are 6 GPa, 4.6 GPa, and 3.9 GPa, respectively [11, 13, 18]. In prior experiments, $HoPO_4$ and $DyPO_4$ were not taken to high enough pressures to capture the full xenotime–monazite coexistence range [19, 81].

Other xenotime compositions with smaller RE^{3+} radii undergo the xenotime → scheelite transformation, which involves no change in RE-O coordination number. $ScPO_4$,

$LuPO_4$, and $YbPO_4$ transform directly to the scheelite structure at P_{onset} values of 34.2 GPa, 19 GPa, and 22 GPa, respectively [12, 13]. Their respective xenotime–scheelite phase coexistence ranges (represented by overlap of green and blue bars in Figure 4.2) are 10.8 GPa, 8 GPa, and 1 GPa, indicating kinetic limitations similar to the xenotime → monazite transformation [12, 13].

$TmPO_4$, as described by Stavrou et al., represents a "borderline case" between xenotime compositions that transform to monazite and those that transform to scheelite [21]. In $TmPO_4$, the xenotime → scheelite transformation begins at 20.3 GPa, and these two phases coexist over a 2.7 GPa range. Immediately after the disappearance of xenotime at 23 GPa, monazite emerges at 23.3 GPa and coexists with scheelite until 47 GPa. Then, scheelite persists through the end of the experiment. Stavrou et al. characterize monazite $TmPO_4$ as a "metastable minority phase" and attribute the long monazite–scheelite coexistence to the stabilization of monazite grains "when embedded in a scheelite matrix."

Among the compositions, which adopt the monazite structure at 1 atm ($\sim 10^{-4}$ GPa), only $LaPO_4$ has been shown to undergo a pressure-induced phase transformation. Lacomba-Perales et al. proposed that $LaPO_4$ transforms to barite (orthorhombic, Pnma) based on powder XRD but could not confirm the barite structure due to significant peak overlap [11]. Ruiz-Fuertes et al. used single crystal XRD and second harmonic generation analysis to confirm the post-monazite structure as non-centrosymmetric "post-barite" (orthorhombic, $P2_12_12_1$) [86]. Post-barite first emerges at 27.1 GPa and coexists with monazite through the end of the experiment at 31 GPa. This experimental data conflicts a bit with their ab initio calculations, which show a pressure range where barite is energetically preferred before the emergence of post-barite, but the authors argue large kinetic barriers may explain the lack of barite in their $LaPO_4$ experiments and may hinder barite formation in other monazite $REPO_4$ compositions [86]. Ruiz-Fuertes et al. project (based on ab initio calculations) a post-barite transformation to occur at 45 GPa and 35 GPa in $GdPO_4$ and $NdPO_4$, respectively, with barite as a possible, but unlikely, transition

phase.

Our 2021 XRD study [81] reported a $DyPO_4$ xenotime → monazite P_{onset} at 9.1(1) GPa under a quasi-hydrostatic loading rate but did not go to high enough pressures to resolve the xenotime–monazite phase coexistence range. This XRD study aims to identify the end of the xenotime–monazite phase coexistence range by going to higher pressures. Results reveal a xenotime–monazite phase coexistence range of 7.6(15) GPa and a previously unreported phase transformation to a post-monazite phase at 13.9(10) GPa. Comparison to the experimental and the computational literature strongly suggests this post-monazite phase adopts the scheelite (tetragonal, $I4_1/a$) structure.

4.5 Materials and Methods

Phase-pure xenotime $DyPO_4$ powder was obtained via precipitation reaction involving $Dy(NO_3)_3 \bullet 5H_2O$ (≥99.9% RE oxide basis, Alfa Aesar) precursor and H_3PO_4 (85% w/w aqueous solution, Alfa Aesar) and subsequent calcination. These two steps are detailed elsewhere [16]. The sample powder consists of sub-micron grains, which exhibit the anisotropic, elongated crystal habit expected of tetragonal materials (see the scanning electron micrograph in Figure D1, see supplementary materials). An energy-dispersive X-ray spectrum of the powder (shown in Figure D2) shows no elemental impurities. In situ DAC XRD was conducted at room temperature at beamline 16-ID-B, HPCAT, Advanced Photon Source, Argonne National Laboratory. Two-dimensional diffraction patterns were collected with the PILATUS 1M-F detector. The X-ray wavelength was 0.42459 Å, and the beam spot size (full width at half maximum) was ∼2 µm by ∼4 µm. We used a Diacell Helios DAC with a membrane (both from Almax easyLab Inc., Cambridge, MA, USA) driven by a Druck PACE 6000 pressure controller [48]. DAC preparation involved successively loading $DyPO_4$ powder, gold powder (>99.96% metals basis, Alfa Aesar, Ward Hill, MA, USA), ruby chips (Almax easyLab Inc., Cambridge, MA, USA), and 16:3:1 methanol–ethanol–water mixture (MEW) pressure medium into the hole of the 301 stainless steel gasket. The gasket hole diameter and indented thickness were 220 µm and 80

µm, respectively. For pressure marking during initial membrane engagement, ruby was used (R1 fluorescence calibration [44]), while gold was used (third order Birch-Murnaghan EoS [87]) during diffraction data collection. Data collection started at 3.1(2) GPa due to some initial compression required to confirm membrane engagement. There are no reported $DyPO_4$ phase transitions below this starting pressure (as corroborated by our 2021 XRD study) [81]; therefore, the initial jump does not preclude any material insight.

XRD pattern integration, masking, and background subtraction were performed using Dioptas [37]. Pattern fitting was then performed using X'Pert HighScore Plus [42]. This software fits monazite using the $P2_1/c$ cell setting as a default. Although both the $P2_1/c$ and $P2_1/n$ cell settings are valid descriptions of monazite (space group No. 14), fitted lattice parameters were converted to the $P2_1/n$ cell setting to facilitate comparison to the literature. The LeBail fitting approach [50] was used instead of traditional Rietveld structural refinement to accommodate the significant preferred orientation present in all scans. This apparent preferred orientation appears due to the small spot size of the beam with respect to the grain size of the sample (effectively sampling a finite number of grains) rather than any inherent orientation of the sample grains. The atmospheric-pressure volume of xenotime $DyPO_4$ (289.39(2) $Å^3$) was derived from a prior synchrotron XRD pattern of a sample from the same batch as the sample in this study [81]. The following reference structures were used in this study: xenotime $DyPO_4$ from Milligan et al. [61], monazite $DyPO_4$ from Heuser et al. [8], gold from Couderc et al. [88], ruby from Jephcoat et al. [89], and calculated scheelite $TbPO_4$ from López-Solano et al. [18]. Importantly, the scheelite $TbPO_4$ structure file was not employed in LeBail fitting—only in peak position comparison. For the computation involving derived data (e.g., unit cell volume, gold-based pressure, cell setting conversion), Python was used to propagate error with an assumed covariance of zero.

4.6 Results

During the experiment, the gold lattice parameter decreases steadily as shown in Figure 4.3a. In Figure 4.3b, the pressure increases steadily with time and yields an effective sample loading rate of ∼20 MPa/s, an order of magnitude faster than that of our 2021 XRD study [81].

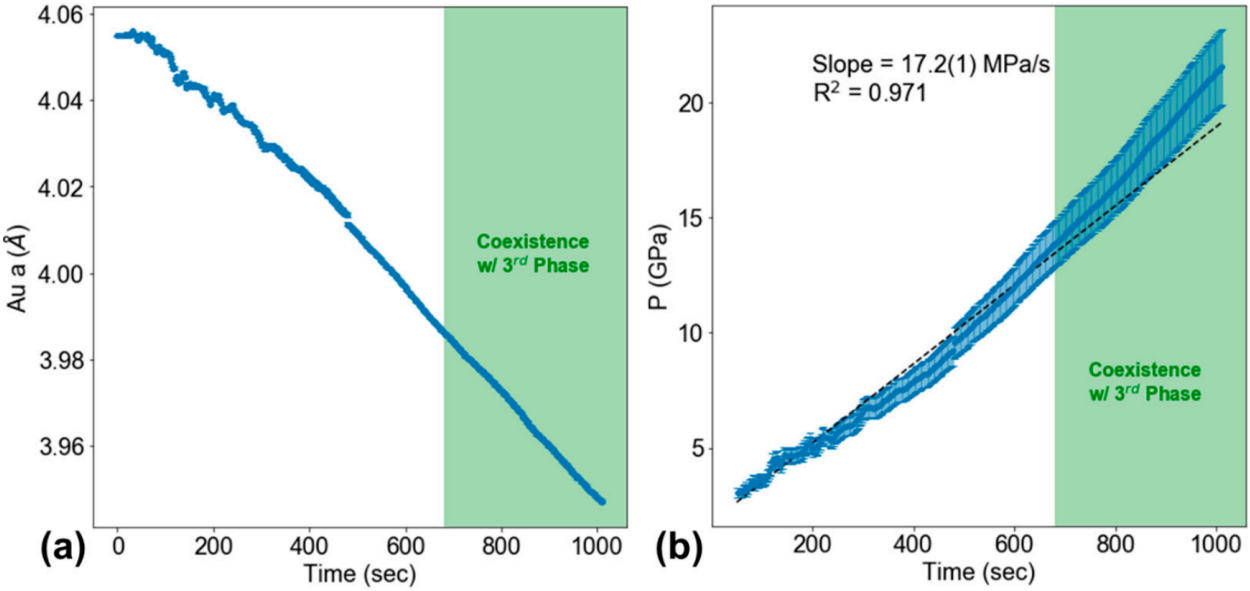

Figure 4.3 Plots showing (a) gold lattice parameter and (b) pressure against time during the experiment. Error bars represent standard deviation. The linear fit of the pressure data yields an effective loading rate of 17.2(1) MPa/s. Green, shaded areas represent the pressure range in which a third (post-monazite) phase of $DyPO_4$ appears in the patterns.

Figure 4.4 shows the pressure evolution of integrated background-subtracted XRD patterns. The square root of intensity is plotted against Q to show weak peaks more clearly. In Figure 4.4a, sample XRD peaks drift to higher Q and broaden with increasing pressure due to uniform and non-uniform strain, respectively. The first scan shows peaks from xenotime $DyPO_4$, gold (triangles), and ruby (circles). Figure 4.4 also illustrates the relative loss of sample signal compared to the strong gold signal as pressure increases. P_{onset} values are determined by visual inspection of individual XRD patterns as shown in Figure 4.4b, not by the coloring in Figure 4.4a.

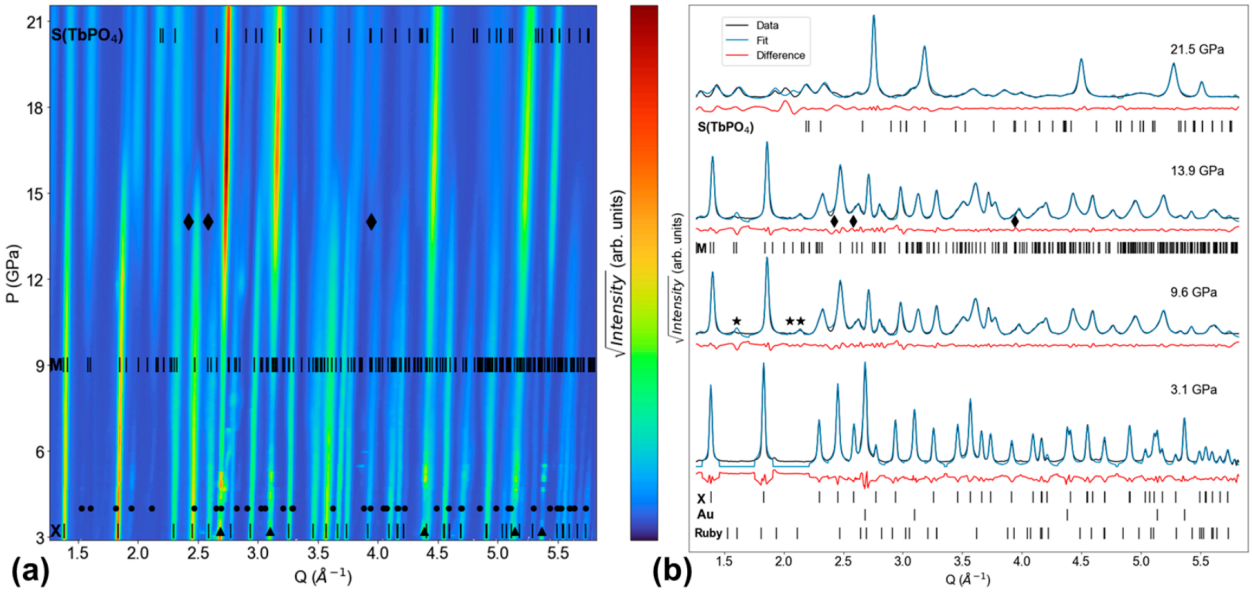

Figure 4.4 Synchrotron XRD patterns. X, M, and S($TbPO_4$) ticks show Bragg reflections of xenotime $DyPO_4$, monazite $DyPO_4$, and scheelite $TbPO_4$, the last based on ab initio structural data reported by Lopez-Solano et al. [18]. Star symbols mark emerging monazite peaks at 9.6(7) GPa, and diamond symbols mark emerging peaks of the unidentified phase at 13.9(10) GPa. (a) A contour plot showing all XRD patterns. Peak positions of gold and ruby are marked with triangles and circles, respectively. (b) The LeBail fits of key patterns (initial scan, onset of monazite, onset of unidentified phase, and final scan.

Figure 4.4b shows the LeBail fits of key patterns (initial scan, onset of monazite, onset of new phase, and final scan). The first discernible monazite peaks emerge at 9.6(7) GPa at Q = 1.60, 2.05, and 2.14 $Å^{-1}$; these are the (110), (002), and (0202$\bar{1}$) reflections. At P_{onset}, the monazite lattice parameters are a = 6.134(1) Å, b = 6.695(1) Å, c = 6.276(1) Å, and β = 99.79(1)°, and the unit cell volume loss during transformation is 7.90%. Although these lattice parameter uncertainties appear quite small, several checks on the LeBail fits do not change the outcome. The xenotime → monazite P_{onset} is below the hydrostatic limit of the MEW pressure medium (10.5(5) GPa), meaning non-hydrostatic stresses likely do not influence the onset of this transformation. At 10.5(5) GPa, MEW undergoes a glass transition into an amorphous phase that contributes no XRD peaks [46]. Above this hydrostatic limit, the sample stress state is understood to be non-hydrostatic. Starting at 17.2(13) GPa, there are no longer any peaks uniquely attributable to xenotime (based on visual inspection of individual patterns). The disappearance of xenotime peaks by this pressure is also apparent in Figure 4.4a and yields a xenotime–monazite phase coexistence range of 7.6(15) GPa.

Interestingly, a new set of previously unidentified XRD peaks emerge at 13.9(10) GPa at Q = 2.42, 2.58, and 3.94 $Å^{-1}$ and persist as the pressure increases (see diamonds in Figure 4.4). These peak positions are inconsistent with xenotime, anhydrite, monazite, ruby, gasket material, gold, or even a "monazite II" phase reported in $CeVO_4$ [90]. Peak positions for the post-monazite phase of $TbPO_4$, scheelite (derived from ab initio calculations at 20.5 GPa), are shown in Figure 4.4 as there are no available structural data on any post-monazite phases of $DyPO_4$. The final scan at 21.5(16) GPa contains peaks corresponding to monazite, gold, ruby, and the unidentified phase.

Next, we examine the pressure-dependence of lattice parameters more closely, finding consistent lattice parameter deviations around the pressure at which the post-monazite phase emerges. Figure 4.5 shows the pressure evolution of $DyPO_4$ lattice parameters for the xenotime (a_X and c_X) and monazite (a_M, b_M, c_M and β_M) phases.

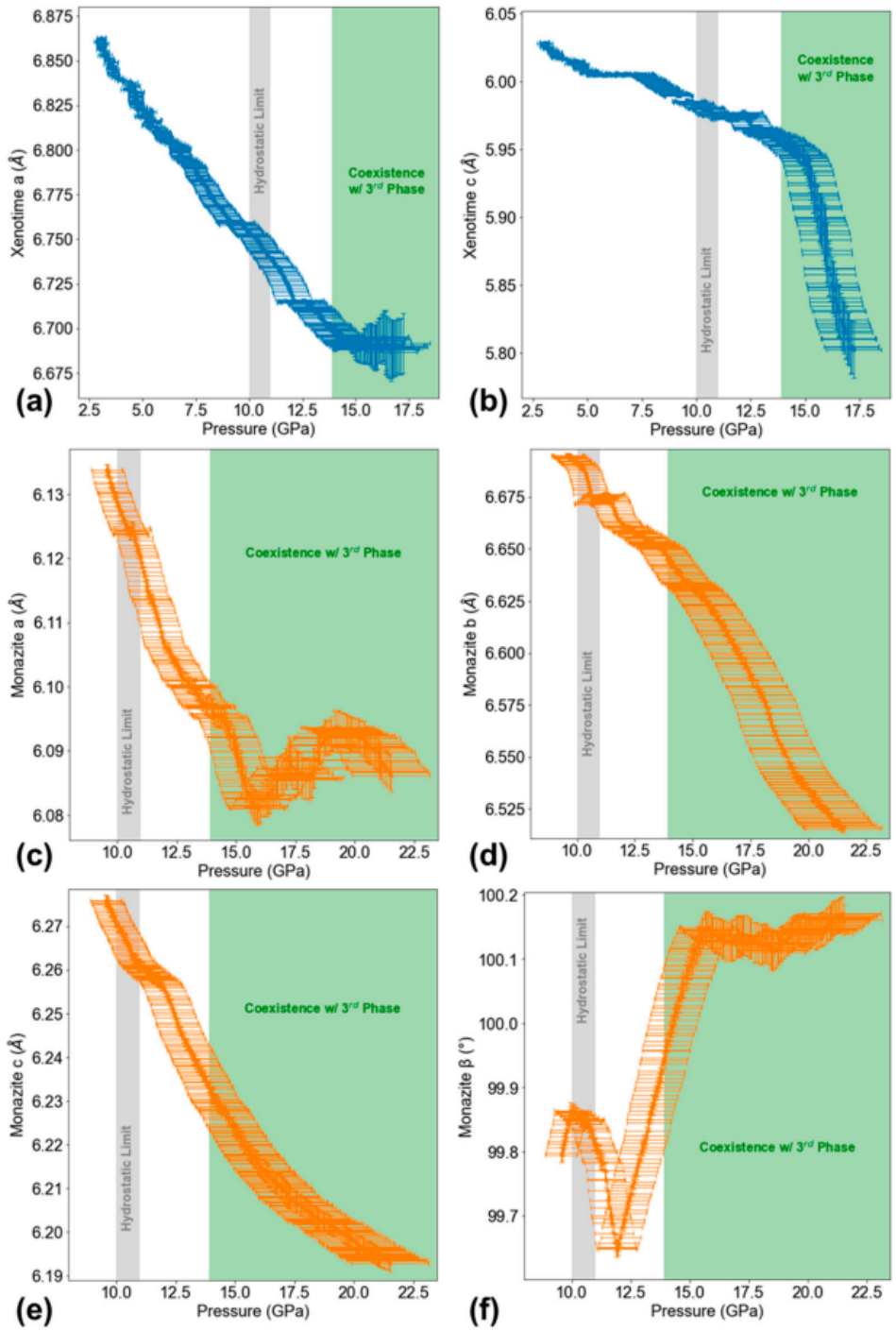

Figure 4.5 Pressure dependence of xenotime (X) and monazite (M) $DyPO_4$ lattice parameters. Green, shaded areas represent the pressure range in which a third (post-monazite) phase of $DyPO_4$ exists. The thin gray shaded area represents the hydrostatic limit of the pressure medium: (a) a_X; (b) c_X; (c) a_M; (d) b_M; (e) c_M; (f) β_M. All parameters show some irregularity around the hydrostatic limit (10.5(5) GPa). The a_X, c_X, a_M and β_M parameters exhibit notable changes in behavior after ∼14 GPa.

Figure 4.5a shows a_X decreasing fairly steadily and monotonically with two slight disruptions at pressures consistent with the xenotime → monazite P_{onset} (9.6(7) GPa) and with the hydrostatic limit of MEW (10.5(5) GPa). Starting at ∼14 GPa, however,$a_X$stops decreasing, and the lattice parameter uncertainty expands significantly; this change in behavior coincides with the emergence of the unidentified peaks. Figure 4.5b shows similar behavior in c_X, except this parameter starts decreasing rapidly at ∼14 GPa. The axial ratio of xenotime (shown in Figure D3) also shows a dramatic trend change at ∼14 GPa. Figure 4.5c shows a_M decreasing monotonically with slight disruptions at the hydrostatic limit and ∼14 GPa. After ∼15 GPa, a_M becomes non-monotonic with pressure, and its error bar expands significantly. Figure 4.5d and Figure 4.5e do not show any anomalies in b_M and c_M around 14 or 15 GPa—only minor disruptions around the hydrostatic limit. Figure 4.5f shows β_M changes monotonicity around the hydrostatic limit, steadily increases with smaller error bars after 12 GPa, then remains almost constant after ∼15 GPa with larger error bars. Figure 4.6 shows all $DyPO_4$ lattice parameters plotted together to better illustrate their relative values and relative compressibilities.

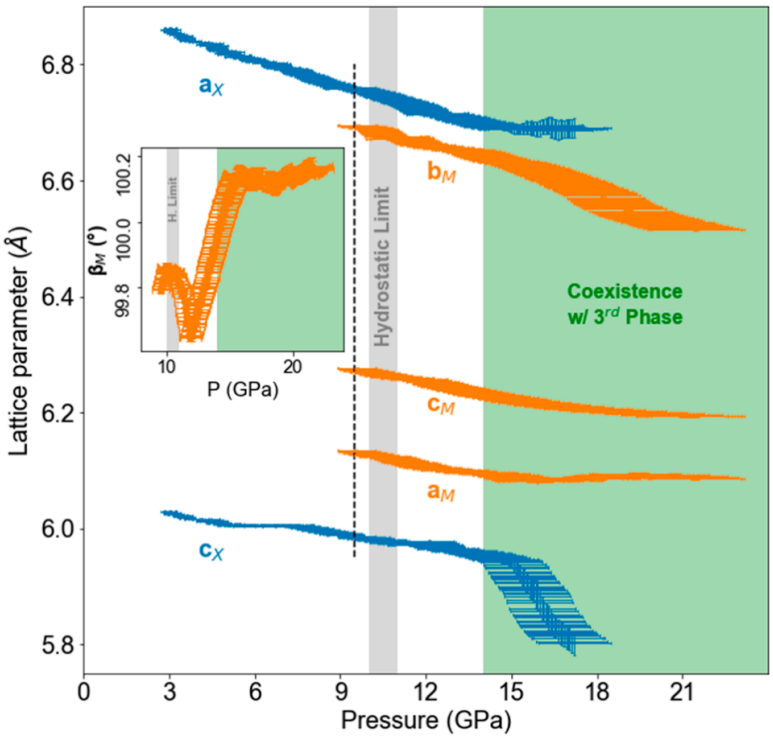

Figure 4.6 Pressure evolution of all $DyPO_4$ lattice parameters for the xenotime (a_X and c_X) and monazite (a_M, b_M,c_M and β_M) phases. Error bars represent standard deviation. The vertical dashed line indicates the xenotime $\rightarrow$ monazite P_{onset}. Green, shaded areas represent the pressure range in which a third (post-monazite) phase of $DyPO_4$ exists. The thin gray shaded area represents the hydrostatic limit of the pressure medium. The inset shows the monazite beta angle.

The c_X, a_M, b_M, and β_M parameters stand out with the most significant changes in behavior beginning at ∼14 GPa, coinciding with the emergence of the third (post-monazite) phase of $DyPO_4$.

Axial compressibilities of the xenotime and monazite phases are obtained by linearly fitting lattice parameter data from pressures below the hydrostatic limit (10.5 GPa). These values are summarized in Table 4.1. The monazite beta angle (β_M) was not analyzed as this parameter's non-monotonic behavior precludes a meaningful linear fit.

Table 4.1 $DyPO_4$ axial compressibilities derived from linear fits of lattice parameter data at pressures below the hydrostatic limit. Negative values indicate compression.

Lattice Parameter	Axial Compressibility (Å,°/GPa) × 10^3	Intercept at 0 GPa	R^2 of Linear Fit
a_X	-16.09 (12)	6.907 (1)	0.9871
c_X	-6.238 (127)	6.045 (1)	0.8876
a_M	-10.67 (22)	6.236 (2)	0.9921
b_M	-11.64 (72)	6.807 (7)	0.9326
c_M	-11.10 (21)	6.382 (2)	0.9934
β_M	-	-	-

4.7 Discussion

This experiment shows the P_{onset} of $DyPO_4$ xenotime → monazite phase transformation is 9.6(7) GPa when loading at ∼20 MPa/s. This pressure is nominally higher than the 9.1(1) GPa P_{onset} observed in our 2021 $DyPO_4$ study under quasi-static loading (∼2 MPa/s) [81]; however, the magnitude of the P_{onset} error unfortunately precludes any conclusions regarding rate-dependence of the xenotime → monazite transformation (e.g., thermal activation, mechanism). The xenotime axial compressibilities (see Table 4.1) and the monazite lattice parameters at P_{onset} are not notably different from those reported in our 2021 $DyPO_4$ study [81], while the monazite axial compressibilities differ significantly in their absolute and relative values. The discrepancy in compressibilities is likely due to this study having a much smaller quasi-hydrostatic pressure regime in which monazite exists (∼1 GPa); therefore, there is a much smaller range and significantly fewer monazite datapoints suitable for fitting in this study than in our previous study.

This work also provides, for the first time, an estimate of the full $DyPO_4$ xenotime–monazite phase coexistence range. Figure 4.4 shows that the xenotime phase is present up to 17.2(13) GPa (also reflected in Figure 4.2 as the upper bound of the blue bar). This value establishes that, while there is not a trend in the experimentally observed monazite P_{onset} with rare-earth radius, there is a general compositional trend in which the upper pressure bound of xenotime decreases with increasing RE^{3+} radius (see Figure 4.2). The $DyPO_4$ xenotime–monazite coexistence range is then 7.6(15) GPa, which is significantly larger than that of both neighboring compositions (4.8 GPa for YPO_4 and 4.6 GPa for $TbPO_4$) and slightly larger than that of $ErPO_4$ (6.0 GPa) [11, 13, 18]. Comparison to $HoPO_4$ is precluded by incomplete xenotime phase transition [19].

Beyond characterizing the xenotime → monazite transformation, this study provides proof of the existence of a new, post-monazite phase of $DyPO_4$. As a reminder, it is crucial to note that no $DyPO_4$ structures other than xenotime and monazite were used during the LeBail fitting (as no other experiment-based $DyPO_4$ structures have been reported). As a result, the fitting process attempted to accommodate the unidentified peaks at Q = 2.42 $Å^{-1}$, 2.58 $Å^{-1}$, and 3.94 $Å^{-1}$ (emerging at 13.9(10) GPa as seen in Figure 4.4) with the xenotime and monazite structures. This accommodation explains the anomalies in a_X, c_X, a_M, and β_M after 13.9(10) GPa as shown in Figure 4.5. The gold lattice parameter variation with time (and its corresponding pressure profile) is smooth and has no interruption at the post-monazite transition pressure (see Figure 4.3), showing that anomalies in xenotime and monazite lattice parameters do not result from experiment instabilities. Indexing the unidentified peaks to a certain structure or space group is extremely difficult because of a weak sample signal at pressures >14 GPa as well as monazite peaks covering most of the Q range.

Comparison to the literature strongly suggests the post-monazite phase is scheelite (tetragonal, $I4_1/a$). Based on preliminary Raman spectroscopy experiments, Stavrou et al. deduce a xenotime → monazite → scheelite transformation pathway in $DyPO_4$ with a

monazite → scheelite P_{onset} at ∼33 GPa [21]. This P_{onset} value may be a significant overestimation, as the Raman spectroscopy-based xenotime → monazite P_{onset} has also proven to be a significant overestimation when compared to XRD work [81]. Further analysis of this Raman spectroscopy-based monazite → scheelite P_{onset} is complicated by the fact that the underlying Raman spectra have yet to be published. Nevertheless, the pressure-induced phase transformation pathways of other xenotime $REPO_4$s support the existence of a monazite → scheelite transformation in $DyPO_4$. Figure 4.2 shows scheelite evolves from monazite (in YPO_4) or directly from xenotime (in $ScPO_4$, $LuPO_4$, $YbPO_4$, and $TmPO_4$) with increasing pressure. Experimental studies of $ErPO_4$, $HoPO_4$, and $TbPO_4$ neither confirm nor deny transformation to scheelite due to limited experimental pressure ranges [11, 18, 19]. In the case of $TbPO_4$, Lopez-Solano et al. point to "kinetic energy barriers" possibly hindering transformation to scheelite [18]. However, ab initio calculations performed by Bose et al. and Lopez-Solano et al. show $ErPO_4$, $HoPO_4$, and $TbPO_4$ are expected to follow the xenotime → monazite → scheelite phase transformation pathway. Bose et al. predict monazite → scheelite P_{onset} values of ∼11 GPa, ∼12 GPa, and ∼14 GPa for $ErPO_4$, $HoPO_4$, and $TbPO_4$, respectively [80]. Lopez-Solano et al. predict a slightly higher $TbPO_4$ monazite → scheelite P_{onset} of 15.5 GPa [18]. Barite and post-barite also bear consideration for the post-monazite phase, but both seem unlikely given experimental and computational data on $LaPO_4$ put the transition for this and other compositions at pressures above 26 GPa [11, 86]. Additionally, Lopez-Solano et al. found the scheelite structure to be energetically favorable to the barite structure [18]. No studies to date report a similar comparison between the scheelite and post-barite structures. Given that the unidentified XRD peaks in this study emerge at a pressure consistent with the expected monazite → scheelite transformation in neighboring compositions, it is likely that these peaks belong to a scheelite $DyPO_4$ phase.

In the absence of scheelite unit cell data for $DyPO_4$, we use $TbPO_4$ for comparison. Lopez-Solano et al. predicted unit cell data of scheelite $TbPO_4$ at 20.5 GPa, which are

added to the top of Figure 4.4 as "S($TbPO_4$)" peak position ticks [18]. Although the new peaks from $DyPO_4$ do not exactly match these ticks in scans around 20.5 GPa, the peaks are reasonably close to the ticks given the differences in methods, RE, temperature, kinetics, and stress state, which together have confounding effects on the unit cell. If this post-monazite $DyPO_4$ phase is further confirmed to be scheelite, 13.9(10) GPa would be the lowest pressure at which scheelite has been reported in $REPO_4$s to date.

4.8 Conclusion

This work significantly extends the characterization of the high-pressure phase behavior of $DyPO_4$, which has been limited, particularly at pressures above 15 GPa. Our 2021 XRD study reported a xenotime → monazite P_{onset} at ∼9 GPa but did not go to high enough pressures to reveal the xenotime–monazite phase coexistence range. This XRD study goes to higher pressures, showing a xenotime–monazite phase coexistence range of 7.6(15) GPa as well as the emergence of new peaks at 13.9(10) GPa. Contextualizing these new peaks within the experimental and the computational literature provides compelling evidence that monazite $DyPO_4$ undergoes a pressure-induced phase transformation to the scheelite structure. Our results also motivate further XRD studies of other $REPO_4$s (e.g., $ErPO_4$, $HoPO_4$, and $TbPO_4$) at higher pressures to explore possible monazite → scheelite transformations and to elucidate high-pressure phase transformation pathways more broadly.

4.9 Acknowledgments

The authors thank Dr. Ivar Reimanis for lending us his Diacell Helios DAC, Matthew Musselman for synthesizing the sample used in the experiment, and Dr. Jesse Smith at HPCAT for performing initial alignment and calibration. The authors acknowledge the APS synchrotron facilities for provision of beamtime on beamline 16-ID-B. This research was supported by the National Science Foundation under Award No. DMR1352499. J.S. was supported by the Department of Defense through the National Defense Science and

Engineering Graduate Fellowship Program. This work was performed at HPCAT (Sector 16), Advanced Photon Source, Argonne National Laboratory. HPCAT operations are supported by DOE National Nuclear Security Administration under Award No. DE-NA0001974 and DOE Office of Basic Energy Sciences (BES) under Award No. DE-FG02-99ER45775, with partial instrumentation funding by the National Science Foundation (NSF). A.P.S. is supported by DOE-BES, under Contract No. DE-AC02-06CH11357.

4.10 Supplementary Information

Supplementary information referenced in this manuscript is is provided in Appendix D. Figure D1: Scanning electron micrograph showing grain size and morphology of sample powder; Figure D2: Energy-dispersive X-ray spectrum of sample powder; Figure D3: Pressure dependence of the axial ratio (c_X/a_X) of the xenotime unit cell.

CHAPTER 5

IN SITU SYNCHROTRON DIFFRACTION OF XENOTIME TBPO4 UNDER VARIABLE HYDROSTATICITY

Manuscript to be submitted to *Solids*

Jai Sharma and Corinne E. Packard

Metallurgical & Materials Engineering Dept., Colorado School of Mines, Golden, Colorado 80401, USA

This manuscript assesses the shear-dependence of the $TbPO_4$ xenotime-monazite phase transformation and follows up on the $DyPO_4$ transformation study in Chapter 3. *In situ* DAC synchrotron XRD was performed using 3 different pressure-transmitting media (PTM) conditions. Trends in the transformation onset pressure (P_{onset}) and phase coexistence ranges are assessed, and a post-monazite $TbPO_4$ phase is discovered. Comparison to other experimental and computational literature suggests this post-monazite phase may be scheelite. This chapter includes an overview of the authors' contributions, a summary of the key findings and contributions of this work, and the full manuscript soon to be submitted to *Solids*.

5.1 Author Contributions

Dr. Packard and I conceptualized the experiments and performed the beamline experiments. I performed formal analysis and was the primary author of this work. Dr. Packard contributed to data interpretation and manuscript editing.

5.2 Scientific Advancements and Conclusions

The work presented in this chapter provides the first systematic analysis of the effect of non-hydrostaticity on $TbPO_4$ pressure-induced phase transformation. Experiments show some of the lowest the lowest P_{onset} values reported for any $REPO_4$. Results also indicate

strategically choosing a PTM (including no PTM) can generate enough shear to induce phase transformation at pressures accessible outside a diamond anvil cell. One experiment potentially provides the first experimental proof of the post-monazite phase of $TbPO_4$.

5.2.1 Key Findings

- The P_{onset} of the $TbPO_4$ xenotime-monazite phase transformation begins at 8.7(6) GPa (in neon PTM), which is lower than previous reports [18].
- The $TbPO_4$ xenotime-monazite P_{onset} decreases as the PTM's effective bulk modulus (at ambient pressure) increases.
- The use of no PTM reduces the $TbPO_4$ xenotime-monazite P_{onset} to 4.4(3) GPa, the lowest P_{onset} reported for any $REPO_4$.
- This study provides *in situ* evidence to corroborate Hay et al.'s *ex situ* observations of transformation in $TbPO_4$ [7].
- $TbPO_4$ has consistently lower P_{onset} values than $DyPO_4$ (even under non-hydrostatic conditions). This is likely due to monazite being more thermodynamically favorable in $TbPO_4$ than in $DyPO_4$.
- When no PTM is used, a post-monazite $TbPO_4$ phase emerges at 10.2(7) GPa. This phase likely adopts the scheelite structure.

5.2.2 Key Contributions

- This work shows conducting *in situ* DAC experiments with non-hydrostatic PTMs can help explain *ex situ* observations of phase transformation from other types of experiments (e.g., indentation, fiber pull-out).
- This study shows a high-shear environment can lower the P_{onset} to pressures below the xenotime $REPO_4$'s hardness, suggesting transformation-related strain-hardening affects measured hardness values [15].

- This work shows that while shear induces earlier transformation onset, it does not induce earlier transformation completion.
- This study shows transformation plasticity and transformation toughening may be accessible at lower pressures and over a wider range of pressures than previously expected.
- This work indicates scheelite may be observed in other xenotime $REPO_4$s (tested under various PTMs) at pressures of at least 20 GPa.

5.3 Abstract

The pressure-induced phase transformations of rare earth orthophosphates ($REPO_4$s) have attracted interest in ceramic matrix composite (CMC) engineering, yet understanding of the shear dependence of these transformations remains limited. This study employs diamond anvil cell experiments with three pressure media (neon, KCl, sample itself/no medium) to systematically assess the effect of shear on the xenotime-monazite phase transformations of $TbPO_4$. Results show a systematic lowering of the $TbPO_4$ transformation onset pressure (P_{onset}) with increasingly non-hydrostatic media. The $TbPO_4$ P_{onset} under no medium (4.4(3) GPa) is the lowest $REPO_4$ P_{onset} reported to date and represents a $\sim$50% drop from the hydrostatic P_{onset}. Enthalpic differences likely account for lower P_{onset} values in $TbPO_4$ than in $DyPO_4$. Experiments also show scheelite may be the post-monazite phase of $TbPO_4$; this phase is consistent with observed and predicted $REPO_4$ transformation pathways.

5.4 Introduction

The deformation mechanisms of rare earth orthophosphates ($REPO_4$s) under complex stress states are highly pertinent to several research fields including geoscience and structural ceramics. In shocked xenotime and monazite minerals, $REPO_4$ deformation microstructures can provide insight into the extreme conditions generated during impact

events [72, 91, 92]. In addition, the pressure-induced xenotime-monazite phase transformation of certain $REPO_4$ compositions offers the possibility of enhanced toughness and plasticity in ceramic matrix composites (CMCs) for aerospace components subject to extreme conditions [7, 15]. When tested as CMC fiber coatings, transforming compositions have been shown to deflect or arrest cracks and facilitate fiber sliding at lower stresses than non-transforming compositions [7].

Identifying the $REPO_4$ compositions which undergo the pressure-induced xenotime-monazite phase transformation requires understanding the compositional phase boundary in the middle of the lanthanide series. In equilibrium at 1 atm (10^{-4} GPa), compositions with smaller RE^{3+} ionic radii (RE = Tb-Lu, Sc, Y) adopt the xenotime (tetragonal, $I4_1/amd$) structure while those with larger RE^{3+} ionic radii (RE = La-Gd) adopt the monazite (monoclinic, $P2_1/n$) structure [9]. Under high hydrostatic pressure, xenotime-structured compositions are known to transform to either the monazite structure or the scheelite (tetragonal, $I4_1/a$) structure with the latter being more favorable in xenotime compositions with the smallest RE^{3+} ionic radii [93]. The three aforementioned crystal structures are illustrated in Figure 5.1.

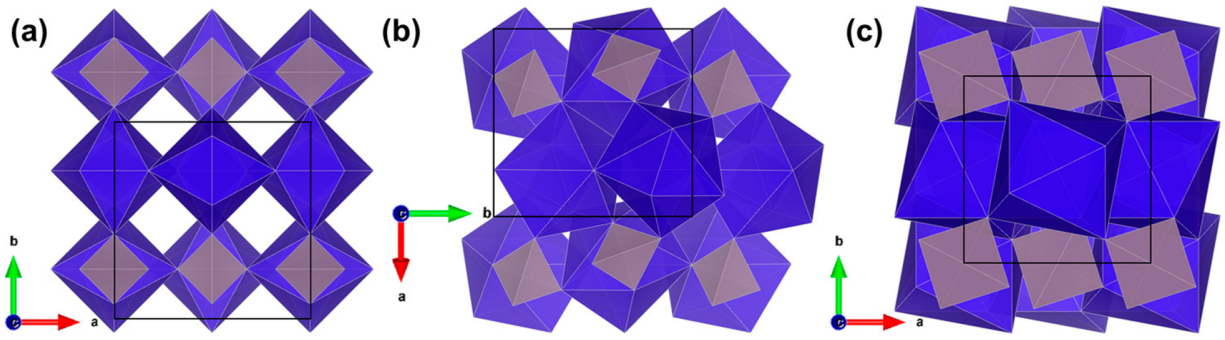

Figure 5.1 [001] views of $REPO_4$ structure in the (a) xenotime, (b) monazite, and (c) scheelite phases. RE-O polyhedra are shown in violet, PO_4 tetrahedra are shown in grey, and the unit cell boundaries are shown as black boxes. The 90° rotation of monazite axes with respect to those of xenotime and scheelite is a result of the monoclinic cell setting of monazite. Adapted from Sharma et al. [93].

The xenotime, monazite, and scheelite structures all contain chains of alternating RE-O polyhedra and PO_4 tetrahedra and have RE-O coordination numbers of 8, 9, and 8, respectively, [76]. Figure 5.1 shows the increasing compaction of the $REPO_4$ structure going from xenotime to monazite to scheelite. This compaction is caused by increasing rotation and translation of the RE-O polyhedra and PO_4 tetrahedra [76]. The barriers associated with these rotations and translations are expected to lower under deviatoric stress as shear strain disrupts otherwise stable bonding symmetries [7]. An intermediate structure, anhydrite (orthorhombic, Amma), has also been reported in xenotime compositions that are extremely close to the xenotime-monazite phase boundary (e.g., $Gd_{0.5}Tb_{0.5}PO_4$) or subjected to high deviatoric stresses at low hydrostatic pressures (e.g., $Gd_xDy_{1-x}PO_4$, $TbPO_4$) [7, 37, 77]).

While the pressure-induced phase transformations of $REPO_4$s have been extensively characterized in (quasi-)hydrostatic environments via *in situ* diamond anvil cell (DAC) x-ray diffraction (XRD) and Raman spectroscopy (RS), studies which systematically evaluate the influence of non-hydrostaticity are extremely limited [93]. Such studies typically vary the pressure-transmitting medium (PTM) in the DAC in order to vary the hydrostaticity of the stress state experienced by the sample. For example, Santamaria-Perez et al. studied orthorhombic $BaSO_4$ using three different fluid PTMs (helium, silicone oil, and 4:1 methanol-ethanol), finding a decreasing hydrostatic limit led to lower transformation onset pressures (P_{onset}) and wider pressure ranges of phase coexistence [22]. In $REPO_4$ literature specifically, Lacomba-Perales et al.'s *in situ* DAC XRD study notes shear promotes earlier xenotime-monazite transformation in YPO_4, but this conclusion is based on a cursory comparison of their findings to a prior YPO_4 study done by others [11]. Our recent *in situ* DAC XRD study probed the effect of shear on the xenotime-monazite transformation of $DyPO_4$ by systematically varying the PTM [81]. We found neon and 16:3:1 methanol-ethanol-water (MEW) PTM yield similar P_{onset} values of 9.1(1) GPa and 9.3 GPa, respectively, while KCl PTM yields a much lower P_{onset} of 7.0

GPa (a ∼22% drop). Even though neon crystallizes at 4.7 GPa, neon and MEW remain (quasi-)hydrostatic at P_{onset} [46]. The significant P_{onset} reduction under KCl is likely attributable to a higher shear stress state given the fact that KCl is never hydrostatic, and its ambient pressure bulk modulus is ∼20 times that of neon [94–96]. Solid PTMs with higher bulk moduli are expected to impart greater shear on the sample as less PTM compression results in greater contact stresses and friction at PTM-sample interfaces (for a given DAC pressure). Unfortunately, $DyPO_4$ was not tested under any solid PTM other than KCl, so another high-shear state was not evaluated. Beyond our $DyPO_4$ study, the effect of shear on phase transformations has yet to be reported for any other $REPO_4$ [81]. In addition, the high-pressure, post-monazite phase of $TbPO_4$ has yet to be experimentally observed.

This study employs *in situ* DAC synchrotron XRD to probe the pressure-induced phase transformations of xenotime $TbPO_4$ under variable hydrostaticity. The experiments performed in this study involve three PTMs: neon, KCl, and "none" (i.e., cell packed with sample and no PTM material). In the "none" PTM condition, the sample is effectively the PTM. Xenotime $DyPO_4$ is also tested in the "none" condition to build on our prior study [81]. $DyPO_4$ and $TbPO_4$ have ambient pressure bulk moduli of 144 GPa and 134 GPa, respectively [18, 81]. Our $TbPO_4$ experiment using neon PTM shows a xenotime-monazite P_{onset} of 8.7(6) GPa, which is lower than other XRD-based hydrostatic P_{onset} values of 9.8 GPa and 9.9 GPa [18]. In addition, $TbPO_4$ experiments in this study show a systematic lowering of the xenotime-monazite P_{onset} when changing the PTM from neon to KCl to "none" (i.e., as PTM bulk modulus increases). Lastly, our $TbPO_4$ experiment with no medium shows an almost 50% drop in P_{onset} (reaching the lowest value reported for any $REPO_4$ to date), provides potential proof of scheelite as the post-monazite phase, and corroborates Hay et al.'s *ex situ* observation of monazite in indented xenotime $TbPO_4$.

5.5 Materials and Methods

Xenotime $TbPO_4$ and $DyPO_4$ powders were synthesized via precipitation reaction and subsequent calcination. Details of these synthesis steps are provided in Chapter 2. The sample powder consists of grains ranging from sub micrometer to a few micrometers in size; these grains exhibit the anisotropic, elongated crystal habit expected of tetragonal materials (see Figures D1 and F1). *In situ* DAC XRD was conducted at room temperature at Beamline 12.2.2 of the Advanced Light Source at Berkeley National Laboratory. For experiments involving neon PTM, DACs were loaded with neon using the University of Chicago Gas Loader in the high-pressure lab at Beamline 12.2.2. Two-dimensional diffraction patterns were collected with the PILATUS 3S 1M detector and an x-ray wavelength of 0.4947 Å. All DACs used were of the symmetric Princeton design and were compressed using a membrane driven by a Druck PACE 6000 pressure controller. Additional experiment-specific details are shown in Table 5.1.

Table 5.1 Experimental details for the XRD experiments performed at Beamline 12.2.2 at the Advanced Light Source.

Experiment Name	Sample	PTM	Culet diameter (μm)	Exposure time (s)	Spot size (μm)	Gasket material	Gasket indented thickness, hole diameter (μm)	P_{max} (GPa)
Tb-neon	$TbPO_4$	Neon	500	20	30	301 SS	60-80, 260	14.0(10)
Tb-KCl	$TbPO_4$	KCl	500	20	20	301 SS	60-80, 260	11.9(8)
Tb-none	$TbPO_4$	none	300	20	10	Re	50, 160	19.3(14)
Dy-none	$DyPO_4$	none	300	20	30	Re	50, 160	10.4(7)

For pressure marking during initial membrane engagement, ruby was used (R1 fluorescence calibration), while gold was used (3rd order Birch-Murnaghan equation of state) during diffraction data collection [44, 87]. Data collection began at pressures higher than 0 GPa due to some initial compression required to confirm membrane engagement. There are no reported $TbPO_4$ or $DyPO_4$ phase transitions below these starting pressure pressures (as corroborated by prior work); therefore, the initial jump does not preclude any material insight [18, 81, 93].

XRD pattern integration, masking, and background subtraction were performed using Dioptas [49]. Pattern fitting was then performed using X'Pert HighScore Plus [42]. This software fits monazite using the $P2_1/c$ cell setting as a default. Though both the $P2_1/c$ and $P2_1/n$ cell settings are valid descriptions of monazite (space group No. 14), fitted lattice parameters were converted to the $P2_1/n$ cell setting to facilitate comparison to literature. The LeBail fitting approach was used instead of traditional Rietveld structural refinement to accommodate the significant preferred orientation present in all scans [50]. This apparent preferred orientation appears due to the small spot size of the beam with respect to the grain size of the sample (effectively sampling a finite number of grains) rather than any systematic preferred orientation of the sample grains. P_{onset} is determined by visual inspection of individual XRD patterns and fit residuals, not by judging color in the waterfall plots shown in the next section (Figure 5.3a, Figure 5.4a, Figure 5.5a, and Figure 5.6a). Visual inspection involves plotting the square root of intensity against Q to ensure emerging peaks are not overlooked due to their extremely low intensity. The following reference structures were used in this study: xenotime $TbPO_4$ from Lopez-Solano et al. [18], xenotime $DyPO_4$ from Milligan et al., [61], monazite $TbPO_4$ and $DyPO_4$ from Heuser et al. [8], anhydrite $TbPO_4$ from Losch et al. [97], gold from Couderc et al. [88], ruby from Jephcoat et al. [89], and calculated scheelite $TbPO_4$ from López-Solano et al. [18]. Importantly, the ruby, anhydrite $TbPO_4$, and scheelite $TbPO_4$ structures were not employed in LeBail fitting, only in peak position comparison. In XRD patterns, the peaks of these three phases are extremely weak or obscured by stronger peaks; as a result, LeBail fits incorporating these phases did not converge. For computation involving derived data (e.g., unit cell volume, gold-based pressure, cell setting conversion), the uncertainties Python package was used to propagate error [51].

5.6 Results and Discussion

Across all experiments, pressure causes XRD peaks to drift to higher Q and broaden due to uniform and non-uniform strain, respectively. In addition, XRD signal quality

deteriorates under increasingly non-hydrostatic PTMs (i.e., going from neon to KCl to none); this trend has been previously reported in hydrostaticity studies of other materials [22, 47].

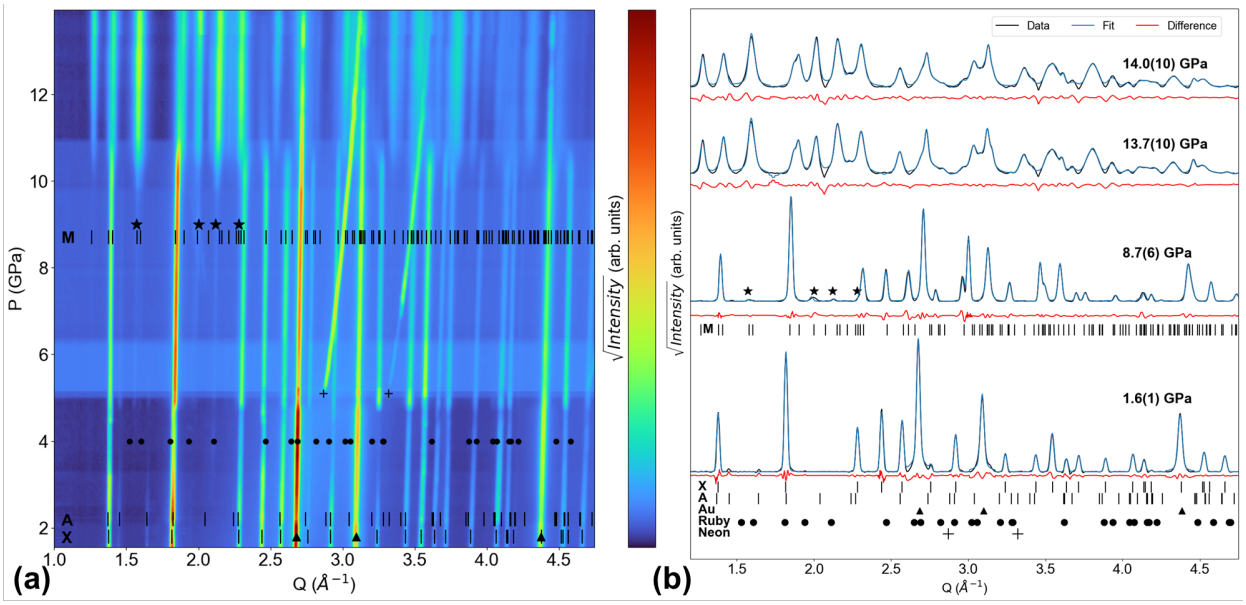

Figure 5.2 Tb-neon XRD experiment. (a) Waterfall plot of all XRD patterns. (b) Select XRD patterns (initial, onset of monazite, end of xenotime, final) and their LeBail fits. Monazite peaks emerge at 8.7(6) GPa. 'X', 'M', and 'A' ticks show $TbPO_4$ peak positions for the xenotime, monazite, and anhydrite phases, respectively [8, 61, 97]. Triangles, circles, pluses, and stars denote the peak positions of gold, ruby, neon, and emerging monazite, respectively [62, 88, 89].

For the Tb-neon experiment, Figure 5.2(a) shows XRD pattern evolution throughout the entire experiment, while Figure 5.2(b) shows LeBail fit quality at $P_{initial}$, P_{onset}, the transformation end pressure (P_{end}), and P_{max}. The first scan in this experiment features xenotime, anhydrite, and gold (upward triangle symbol) peaks. At ~5 GPa, the neon PTM crystallizes, and conditions shift from hydrostatic (in liquid neon) to quasi-hydrostatic (in solid neon) [64]. Solid neon adopts the FCC structure and is still extremely compressible with a bulk modulus of ~1 GPa [62]. Neon remains the most compressible material in the DAC as evidenced by neon peaks shifting much more more dramatically with increasing pressure than the other materials' peaks in Figure 5.2(a). The first discernible monazite

peaks emerge at 8.7(6) GPa and are located at Q = 1.58 $Å^{-1}$, 1.59 $Å^{-1}$, 1.98 $Å^{-1}$, 2.13 $Å^{-1}$, and 2.29 $Å^{-1}$ (as denoted by stars in Figure 5.2); these are the (110), $(10\overline{2})$, (002),$(02\overline{1})$, and $(21\overline{2})$ reflections, respectively. Figure 5.2 also shows these peaks grow with pressure. In the P_{onset} scan shown in Figure 5.2(b), the refined monazite lattice parameters are a = 6.175(1) Å, b = 6.699(1) Å, c = 6.483(1) Å, and β = 100.67(1)°. This P_{onset} value is higher than neon's crystallization pressure and lower than neon's hydrostatic limit, meaning the stress state is quasi-hydrostatic at P_{onset}. Going higher in pressure, monazite peaks grow while xenotime peaks diminish. At 13.7(10) GPa, there are no longer any clearly discernible peaks that are attributable to xenotime. Therefore, 13.7(10) GPa is the end of the xenotime-monazite phase transformation (P_{end}) and yields a xenotime-monazite phase coexistence range of 5.0(10) GPa. In the final scan at 14.0(10) GPa, monazite, gold, and neon are the only phases present. The presence of any anhydrite is unlikely but unclear given the deterioration of signal quality as well as the number and broadness of peaks at this pressure.

A key result from the Tb-neon experiment is the P_{onset} of 8.7(6) GPa, which is the lowest P_{onset} value for $TbPO_4$ in neon PTM reported to date. Lopez-Solano et al. reported a higher value of 9.9 GPa based on XRD experiments also conducted with neon PTM. Our experiment shows monazite peaks are clear at 9.9 GPa and at pressures leading up to this value (see Figure 5.2(a)). Figure 5.3 provides a closer look at our dataset, showing how including the monazite structure improves the fit of the XRD pattern collected at 8.7(6) GPa.

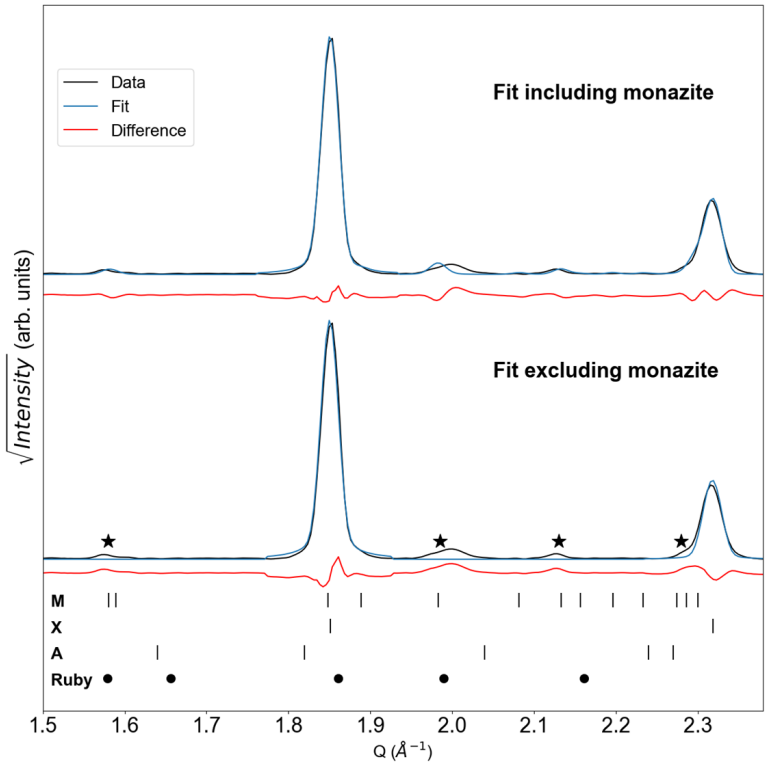

Figure 5.3 LeBail fits with and without monazite for the P_{onset} scan from the Tb-neon experiment. 'X', 'M', and 'A' ticks show $TbPO_4$ peak positions for the xenotime, monazite, and anhydrite phases, respectively [8, 61, 97]. Circles show reference ruby peak positions, and stars indicate regions of intensity consistent with monazite peaks [89].

When monazite is excluded from the fit, there are regions of increased residual intensity (denoted by stars) that align with monazite peak positions. Although some ruby peaks are also quite close to the starred regions, ruby peaks do not align with all of these regions. Furthermore, ruby signal is not expected to intensify with pressure, while the intensity in those starred regions does (as shown in Figure 5.2).

In addition, Lopez-Solano et al.'s $TbPO_4$ P_{onset} is higher than the previously reported $DyPO_4$ P_{onset} of 9.1(1) GPa (also in neon PTM) [81]. Thermodynamic data (i.e., calculated enthalpy differences between xenotime and monazite phases as well as experimental calcination temperatures required to convert monazite to xenotime) show the monazite phase is more favorable in $TbPO_4$ than in $DyPO_4$ [16, 23, 24, 98]. As a result, $TbPO_4$ is expected to have a lower xenotime-monazite P_{onset} than $DyPO_4$. The $TbPO_4$ P_{onset} reported in this study is consistent with thermodynamic expectations. Nevertheless, the P_{end} of 13.7(10) GPa determined in this study is consistent with Lopez-Solano et al.'s P_{end} of 13.8 GPa.

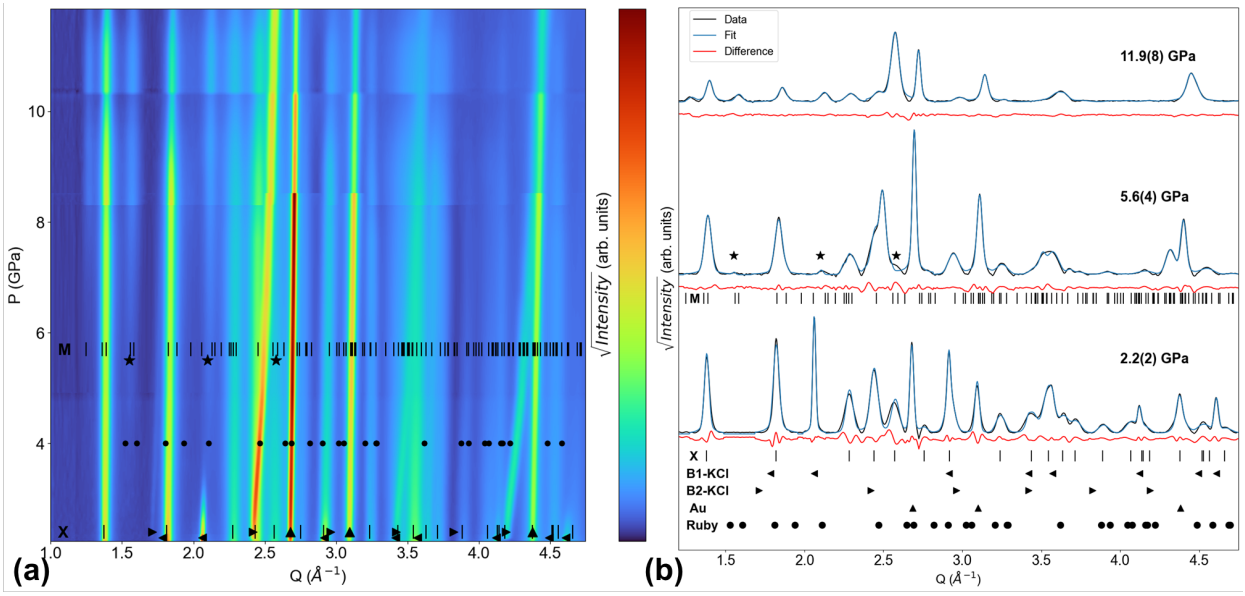

Figure 5.4 Tb-KCl XRD experiment. (a) Waterfall plot of all XRD patterns. (b) Select XRD patterns (initial, onset of monazite, final) and their LeBail fits. Monazite peaks emerge at 5.6(4) GPa. 'X' and 'M' ticks show $TbPO_4$ peak positions for the xenotime and monazite phases, respectively [8, 61]. Circles, upward triangles, leftward triangles, rightward triangles, and stars denote the peak positions of ruby, gold, B1-KCl, B2-KCl, and emerging monazite, respectively [63, 88, 89].

For the Tb-KCl experiment, Figure 5.4(a) shows XRD pattern evolution throughout the entire experiment, while Figure 5.4(b) shows LeBail fit quality at $P_{initial}$, P_{onset}, and P_{max}. The first scan in this experiment contains peaks belonging to xenotime, gold (upward triangle symbol), and B1-KCl (leftward triangle symbol). B1-KCl is the ambient pressure phase of KCl with a NaCl-type structure, and it begins transforming to the CsCl-type B2-KCl structure (rightward triangle symbol) at 2.3(1) GPa. Similar to neon in the Tb-neon experiment, KCl in this experiment is the most compressible material in the DAC, causing its peaks to shift (in Q) more than the sample's peaks [63]. KCl peaks do not shift as dramatically as neon's peaks in the Tb-neon experiment because KCl has a higher bulk modulus than neon.

At 5.6(4) GPa, monazite peaks emerge at Q = 1.55 $Å^{-1}$, 2.1 $Å^{-1}$, and 2.58 $Å^{-1}$ (as denoted by stars in Figure 5.4); these are the (110), $(02\bar{1})$, and (211) reflections, respectively. In the P_{onset} scan, the refined monazite lattice parameters are a = 6.239(1) Å, b = 6.832(3) Å, c = 6.793(1) Å, and $\beta = 99.06(1)^\circ$. Both the xenotime and monazite phases persist through the end of the experiment at 11.9(8) GPa, so the phase coexistence range is at least 6.3(8) GPa. In the final scan at 11.9(8) GPa, xenotime, monazite, gold, and B2-KCl are the only phases present. The anhydrite phase, if it exists, may be obscured by much stronger KCl peaks.

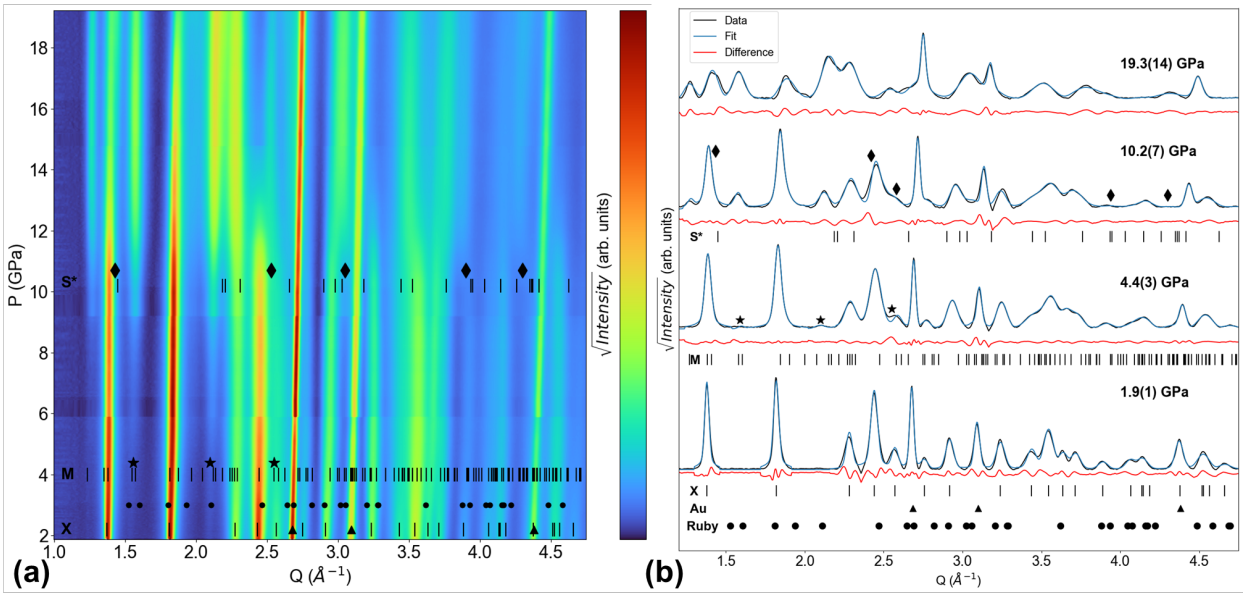

Figure 5.5 Tb-none XRD experiment. (a) Waterfall plot of all XRD patterns. (b) Select XRD patterns (initial, onset of monazite, onset of scheelite, final) and their LeBail fits. Monazite peaks emerge at 4.4(3) GPa. Scheelite peaks appear to emerge at 10.2(7) GPa. 'X', 'M', and 'S*' ticks show $TbPO_4$ peak positions for the xenotime, monazite, and simulated scheelite phases, respectively [8, 18, 61]. Triangles, circles, stars, and diamonds denote the peak positions of gold, ruby, emerging monazite, and emerging scheelite, respectively [88, 89].

For the Tb-none experiment, Figure 5.5(a) shows XRD pattern evolution throughout the entire experiment, while Figure 5.5(b) shows LeBail fit quality at $P_{initial}$, the xenotime-monazite P_{onset}, the potential scheelite P_{onset}, and at P_{max}. The first scan in this experiment shows xenotime, gold (upward triangle symbol), and possibly weak ruby (circle symbol) peaks. At 4.4(3) GPa, monazite peaks emerge at Q = 1.55 $Å^{-1}$, 2.10 $Å^{-1}$, and 2.58 $Å^{-1}$ (as denoted by stars in Figure 5.5); these are the (110), $(02\overline{1})$, and (211) reflections, respectively. In the P_{onset} scan, the refined monazite lattice parameters are a = 6.134(1) Å, b = 6.870(1) Å, c = 6.187(2) Å, and $\beta = 99.83(2)°$.

At 10.2(7) GPa, new peaks emerge at Q = 1.43 $Å^{-1}$, 2.53 $Å^{-1}$, 3.04 $Å^{-1}$, 3.89 $Å^{-1}$, and 4.29 $Å^{-1}$ (denoted by diamond symbols in Figure 5.5), and these peaks grow as pressure continues to increase. The phase giving rise to these peaks is likely scheelite-structured $TbPO_4$ as Lopez-Solano et al. and Bose et al. have predicted scheelite as the post-monazite phase of $TbPO_4$, and scheelite has been experimentally observed in YPO_4, $TmPO_4$, $YbPO_4$, $LuPO_4$, and $ScPO_4$ [12, 13, 18, 80]. Figure 5.5 also shows 'S*' ticks, which represent the peak positions of a simulated scheelite $TbPO_4$ structure at 20.5 GPa, as reported by Lopez-Solano et al. [18]. Given the differences between this study and Lopez-Solano et al.'s simulation (e.g., methods, temperature, pressure, stress state, and the confounding effects of these factors), the proximity of most of the new peaks (diamond symbols) to the 'S*' ticks suggests the presence of scheelite is plausible and requires confirmation via further XRD experiments. If confirmed, 10.2(7) GPa GPa would be the lowest pressure at which any scheelite structure has been reported in $REPO_4$s to date.

The final scan in this experiment contains xenotime, monazite, gold, and potentially scheelite. Therefore, this experiment yields a xenotime-monazite phase coexistence range of at least 14.9(14) GPa and a potential xenotime-monazite-scheelite phase coexistence range of at least 9.1(14) GPa. While the anhydrite phase exists in the sample powder, evidence of this phase does not appear in the scans of this experiment.

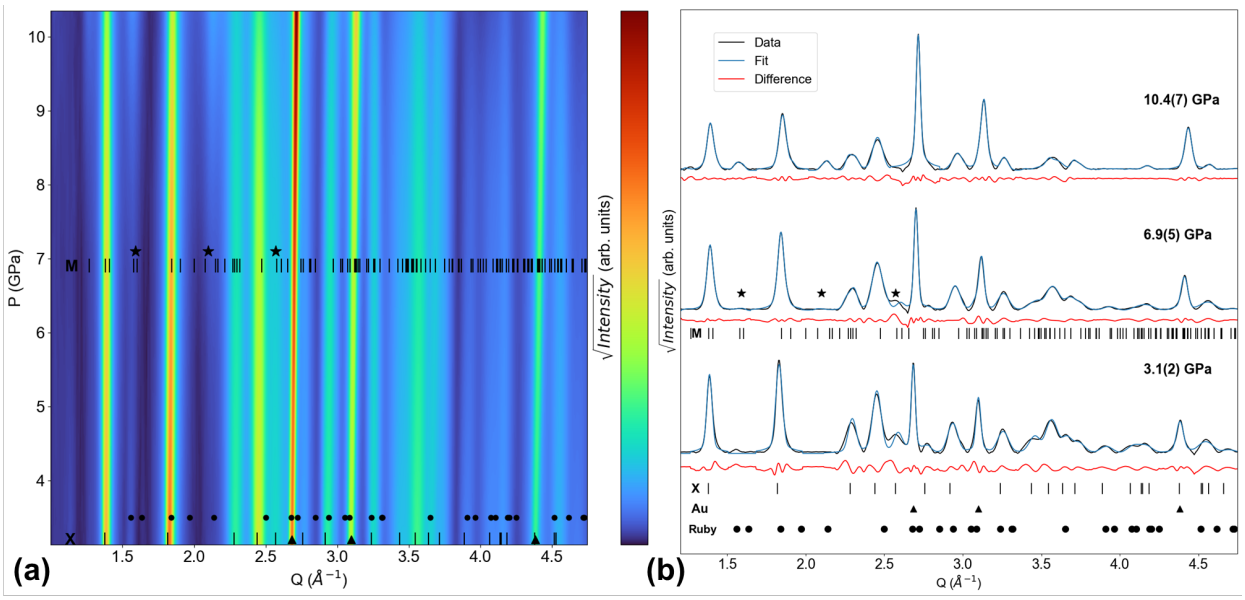

Figure 5.6 Dy-none XRD experiment. (a) Waterfall plot of all XRD patterns. (b) Select XRD patterns (initial, onset of monazite, final) and their LeBail fits. Monazite peaks emerge at 6.9(5) GPa. 'X' and 'M' ticks show $DyPO_4$ peak positions for the xenotime and monazite phases, respectively [8, 61]. Triangles, circles, and stars denote the peak positions of gold, ruby, and emerging monazite, respectively [88, 89].

A Dy-none experiment was also performed to build on our prior $DyPO_4$ study, in which KCl was the only non-hydrostatic PTM tested [81]. Figure 5.6(a) shows XRD pattern evolution throughout the entire experiment, while Figure 5.6(b) shows LeBail fit quality at $P_{initial}$, at the xenotime-monazite P_{onset}, and at P_{max}. The first scan in this experiment shows xenotime, gold (upward triangle symbol), and ruby (circle symbol) peaks. At 6.9(5) GPa, monazite peaks emerge at Q = 1.59 Å^{-1}, 2.10 Å^{-1}, and 2.57 Å^{-1} (as denoted by stars in Figure 5.5); these are the (110), (02$\bar{1}$), and (211) reflections, respectively. In the P_{onset} scan, the refined monazite lattice parameters are a = 6.187(3) Å, b = 6.603(2) Å, c = 6.783(5) Å, and β = 102.40(4)°. The final scan at 10.4(7) GPa contains xenotime, monazite, and gold. Consequently, the $DyPO_4$ xenotime-monazite phase coexistence range is found to be at least 3.5(7) GPa.

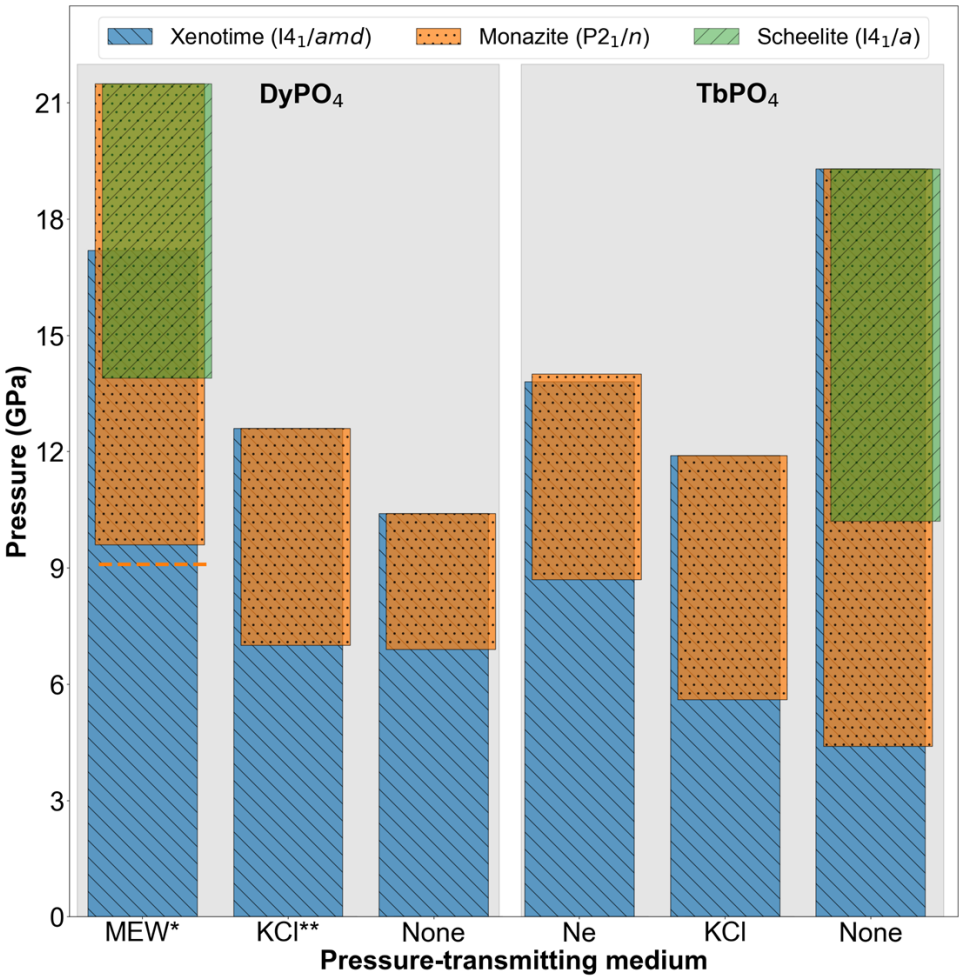

Figure 5.7 High-pressure XRD-based phase map of $DyPO_4$ and $TbPO_4$, each tested with three different PTMs. The legend lists the phases with their corresponding space groups. For each $REPO_4$-PTM combination, the upper limit of the highest bar(s) represents the highest pressure at which data are reported and does not represent a phase boundary. *The Dy-MEW data was originally reported by Sharma et al. [93]. The dashed orange line shows the $DyPO_4$ xenotime-monazite P_{onset} value using neon PTM [81]. **The Dy-KCl data was originally reported by Sharma et al. [81].

Figure 5.7 summarizes the $DyPO_4$ and $TbPO_4$ phase behavior transformation data reported in this study as well as in two prior $DyPO_4$ studies [81, 93]. In the $DyPO_4$ section, phase data from an experiment using the MEW PTM (Dy-MEW [93]) is shown since a prior experiment using neon (Dy-neon [81]) did not to go high enough pressures to gauge the xenotime-monazite phase coexistence range. MEW has a hydrostatic limit of 10.5(5) GPa and is therefore, hydrostatic at the xenotime-monazite P_{onset} like neon. The P_{onset} from the Dy-neon experiment (9.1(1) GPa) is shown as an orange dashed line in Figure 5.7 and is within the error bar of the P_{onset} from the Dy-MEW experiment (9.6(7) GPa).

Figure 5.7 shows $DyPO_4$ and $TbPO_4$ both exhibit xenotime-monazite P_{onset} reductions with non-hydrostatic PTMs. Shear can facilitate the plastic deformation involved in phase transformation (i.e., polyhedral rotations and translations) and thereby, reduce the hydrostatic pressure required to induce phase transformation. In addition, the $TbPO_4$ P_{onset} values are marginally (KCl) or significantly (none) lower than those of $DyPO_4$ in the same PTM. $TbPO_4$ P_{onset} values being lower likely stems from the monazite phase being more thermodynamically favorable in $TbPO_4$ than in $DyPO_4$ regardless of the kinetic barriers involved [16, 23, 24, 98].

Figure 5.7 also shows the onset of the scheelite phase at 13.9(10) GPa in the Dy-MEW and at 10.2(7) GPa in the Tb-none experiments. This difference in scheelite P_{onset} values is likely a convolution of compositional and shear effects. Moreover, the lack of scheelite (green bars) in the other 4 experiments shown in Figure 5.7 does not imply that scheelite wouldn't emerge in those experiments; rather, the experiment did not go to sufficiently high pressures. Given the fact that P_{onset} lowers under shear, it is within reason that the Dy-KCl and Dy-none experiments simply did not ramp to high enough pressures to reach the onset of scheelite. By the same logic, it is within reason that the Tb-neon and Tb-KCl experiments did not ramp to high enough pressures to reach the onset of scheelite. Therefore, additional Dy-KCl, Dy-none, Tb-Ne, and Tb-KCl experiments going to higher pressures are merited.

Next, the effect of shear on xenotime-monazite phase coexistence is considered. All experiments shown in Figure 5.7 show significant phase coexistence ranges of at least 3 GPa, further supporting the notion that $REPO_4$ phase transformations are diffusional rather than martensitic. The $TbPO_4$ experiments show while shear induces earlier onset of transformation, it does not induce earlier completion of transformation. While the xenotime-monazite coexistence range is 5.0(10) GPa in the Tb-neon experiment, this range extends to at least 6.3(8) GPa and at least 14.9(14) GPa in the Tb-KCl and Tb-none experiments, respectively. This range extension has also been reported in $BaSO_4$ and α-Ti when these materials are compressed using non-hydrostatic PTMs [22, 47]. At a fundamental level, extended phase coexistence under shear may be attributable to non-uniform stress fields causing varying degrees of transformation progression in a given volume of material. Conclusions regarding coexistence trends cannot be drawn from the $DyPO_4$ experiments as the Dy-KCl and Dy-none experiments do not go to sufficiently high pressures. For completeness, plots showing the pressure-dependence of $TbPO_4$ and $DyPO_4$ lattice parameters as well as a table of axial compressibilities are provided in Appendix E.

5.7 Conclusion

This study systematically probes the effect of non-hydrostaticity on the pressure-induced phase transformations of xenotime $TbPO_4$ using *in situ* DAC XRD. Our prior $DyPO_4$ study found the non-hydrostatic KCl PTM induces the xenotime-monazite phase transformation at a pressure ∼22% lower than in hydrostatic media (e.g., neon, 16:3:1 MEW) [81]. In this work, our experiments with three PTMs (neon, KCl, and none) show a lowering of the $TbPO_4$ xenotime-monazite P_{onset} from 8.7(6) GPa to 5.6(4) GPa to 4.4(3) GPa, respectively. The P_{onset} value for $TbPO_4$ with no PTM is the lowest value reported to date for any $REPO_4$ and represents an almost 50% P_{onset} reduction in a stress state more relevant to potential CMC applications. When comparing $DyPO_4$ and $TbPO_4$, the latter's P_{onset} values are consistently lower; this fact is likely due to the monazite phase being more thermodynamically favorable in $TbPO_4$ than in $DyPO_4$. Lastly, our $TbPO_4$

experiment with no PTM provides potential proof of scheelite as the high-pressure, post-monazite phase.

5.8 Acknowledgments

This work was performed at Beamline 12.2.2, Advanced Light Source, Berkeley National Laboratory. The authors thank the beamline scientists: Dr. Martin Kunz, Dr. Kathrin Armstrong, and Dr. Bora Kalkan. The authors also greatly appreciate the assistance of John Copley and Dr. Tom Duffy at Princeton University in providing diamond anvil cells and invaluable support while preparing for and performing experiments. In addition, the authors thank Dr. Ivar Reimanis for lending his diamond anvil cell for beamline experiments. Moreover, the authors thank Henry Afful for helping perform experiments and synthesizing the $EuPO_4$ sample as well as Matthew Musselman for synthesizing the $DyPO_4$ sample. This research was supported by the National Science Foundation under Award No. DMR-1352499. J.S. was supported by the Department of Defense through the National Defense Science & Engineering Graduate Fellowship Program. Beamline 12.2.2 is partially supported by COMPRES, the Consortium for Materials Properties Research in Earth Sciences under NSF Cooperative Agreement EAR 1606856. Beamline 12.2.2 at the Advanced Light Source is a DOE Office of Science User Facility under contract no. DE-AC02-05CH11231.

5.9 Supplementary Information

Supplementary information is shown in Appendix E and includes plots showing the pressure evolution of lattice parameters from each of the experiments as well as a table of axial compressibilities.

CHAPTER 6

REVEALING THE PRESSURE-INDUCED PHASE TRANSFORMATION OF XENOTIME TBPO4 VIA *IN SITU* PHOTOLUMINESCENCE SPECTROSCOPY

Manuscript to be submitted to *ACS Materials Letters*

Jai Sharma[1], Brandon Reynolds[2], Matthew J. Crane[2], and Corinne E. Packard[1]

[1]Metallurgical & Materials Engineering Dept., Colorado School of Mines, Golden, Colorado 80401, USA

[2]Chemical & Biological Engineering Dept., Colorado School of Mines, Golden, Colorado 80401, USA

This manuscript describes the use of down-conversion (or direct excitation) photoluminescence (PL) spectroscopy to detect the xenotime-monazite transformation in $TbPO_4$. PL band metrics indicate transformation onset and end pressures that appear consistent with synchrotron XRD results from Chapter 5. Certain irreversible pressure-induced changes in PL spectra can offer insight into stress history (including history of phase transformation). The chapter includes an overview of the author's contributions, a summary of the key findings and contributions of this work, and the full manuscript soon to be submitted to *ACS Materials Letters*.

6.1 Author Contributions

Dr. Packard and I conceptualized this study as part of my NDSEG fellowship proposal. Brandon Reynolds and I performed experiments with instrumentation support and guidance from Dr. Matthew Crane. Brandon and I analyzed data and drafted this manuscript. Drs. Crane and Packard contributed to the reviewing and editing of this manuscript.

6.2 Scientific Advancements and Conclusions

The work presented in this chapter complements the $TbPO_4$ XRD study shown in Chapter 5 with a technique that does not require synchrotron access and is more sensitive to local symmetry: photoluminescence (PL) spectroscopy. While Runowski et al. have performed *in situ* DAC PL on a xenotime $REPO_4$, their study involves up-conversion PL, which is a significantly less efficient process than down-conversion (or direct excitation) PL, which is employed in this study [39]. This PL study shows the crystal field experienced by Tb^{3+} in $TbPO_4$ changes during the xenotime-monazite phase transformation, and tracking these changes via PL yields a phase transformation pressure range that is consistent with the XRD-based phase transformation range determined in Chapter 5. PL spectra after decompression confirm the irreversibility of transformation and show other irreversible changes, offering insight into stress history. Finally, this work shows high-pressure PL characterization can open the door to a non-contact, optical stress history-sensing functionality in CMC fiber coatings.

6.2.1 Key Findings

- At pressures consistent with the XRD-based xenotime-monazite P_{onset}, new $TbPO_4$ PL peaks emerge.
- The emergence of additional $TbPO_4$ PL peaks at the aforementioned pressure is consistent with the symmetry reduction expected during phase transformation.
- At pressures consistent with the XRD-based xenotime-monazite P_{onset} and P_{end}, $TbPO_4$ PL band metrics (centroid and intensity ratios) show clear trend changes.
- $TbPO_4$ PL spectra after decompression show the presence of metastable monazite, indicating synchrotron techniques are not necessary to detect monazite in very small samples.

- Certain $TbPO_4$ PL band centroids and intensity ratios do not return to their original value after decompression, indicating residual crystal field distortion or disruption that may serve as an indicator of stress history.

- Pressure-induced PL changes are more reversible when $TbPO_4$ has not experienced pressures high enough to induce phase transformation.

6.2.2 Key Contributions

- While RS and synchrotron XRD are traditionally used for interrogating $REPO_4$s phase transformations, this work shows direct excitation (down-conversion) PL spectroscopy, a technique with stronger signal than RS and greater accessibility than synchrotron techniques, can be used to detect the pressure-induced xenotime-monazite phase transformation.

- This work shows direct excitation (down-conversion) PL emissions of RE^{3+} can provide insight into stress history in $REPO_4$s.

- This work provides the first high-pressure, direct excitation (down-conversion) PL dataset of $TbPO_4$ or any other xenotime $REPO_4$, enabling further fundamental research into the effect of pressure and symmetry loss on 4f orbitals.

- The identification and analysis of pressure-dependent Tb^{3+} PL band metrics can be applied when studying the behavior of $TbPO_4$ in other conditions (e.g., various stress states).

- Compared to up-conversion PL, the use of down-conversion PL can allow $REPO_4$s to be studied with fewer (or no) dopants, yielding experimental data that more accurately reflects the sample's behavior. This advantage also holds for a wide range of other RE-based oxide compounds (e.g., REXO4s, X = V, As, Sb, W, Nb, or Mo).

6.3 Abstract

The pressure-induced xenotime-monazite phase transformation of certain rare earth orthophosphates ($REPO_4$s) has garnered broad interest from geoscience to structural ceramics. Studying this transformation has required *in situ* DAC Raman spectroscopy or synchrotron XRD, which suffer from poor signal and poor accessibility, respectively. This study exploits the photoluminescence (PL) of Tb^{3+} ions and the unique sensitivity of photoluminescence (PL) to local bonding environment to interrogate the symmetry-reducing xenotime-monazite phase transformation of $TbPO_4$. At pressures consistent with the XRD-based phase transformation onset pressure of 8.7(6) GPa, PL spectra show new peaks emerging as well as trend changes in the centroids and intensity ratios of certain PL bands. Furthermore, PL spectra of recovered samples show transformation is irreversible. Hysteresis in certain PL band intensity ratios also reveals stress history in $TbPO_4$. This *in situ* PL approach can be applied to probe pressure-induced transformations and crystal field distortions in other RE-based oxide compounds.

6.4 Introduction

Rare earth orthophosphates ($REPO_4$s) are a highly refractory class of ceramics with multi-disciplinary appeal [1]. These materials naturally occur in xenotime and monazite minerals, whose properties and formation are of great interest in geoscience and in mining [2, 72, 92, 99]. $REPO_4$s have also been synthesized with high purity and precise RE doping for optical applications (e.g., phosphors, lasers, and scintillators) [30, 31, 100–102]. In recent decades, $REPO_4$s have been investigated as potential fiber coatings in oxide-oxide ceramic matrix composites (CMCs) for aerospace components subject to extreme conditions [5, 14]. In particular, $REPO_4$ compositions which undergo pressure-induced phase transformations offer the possibility of additional toughening and plasticity mechanisms in CMCs [7, 15]. Phase transformation may also be relevant to tuning the photoluminescent

properties of $REPO_4$s or other RE-based materials for fundamental, low-symmetry RE studies as well applications in sensing, laser-cooling, and photonic devices [33, 39, 103–106].

Exploiting the pressure-induced phase transformation of $REPO_4$s begins with understanding their polymorphism. In equilibrium at 1 atm, $REPO_4$ crystal structure is largely determined by ionic radius. Compositions with smaller RE^{3+} ionic radii (RE = Tb-Lu, Sc, Y) crystallize in the xenotime structure (tetragonal, $I4_1/amd$), while those with larger RE^{3+} ionic radii (RE = La-Gd) crystallize in the monazite structure (monoclinic, $P2_1/n$) as shown in Figure 6.1 [9].

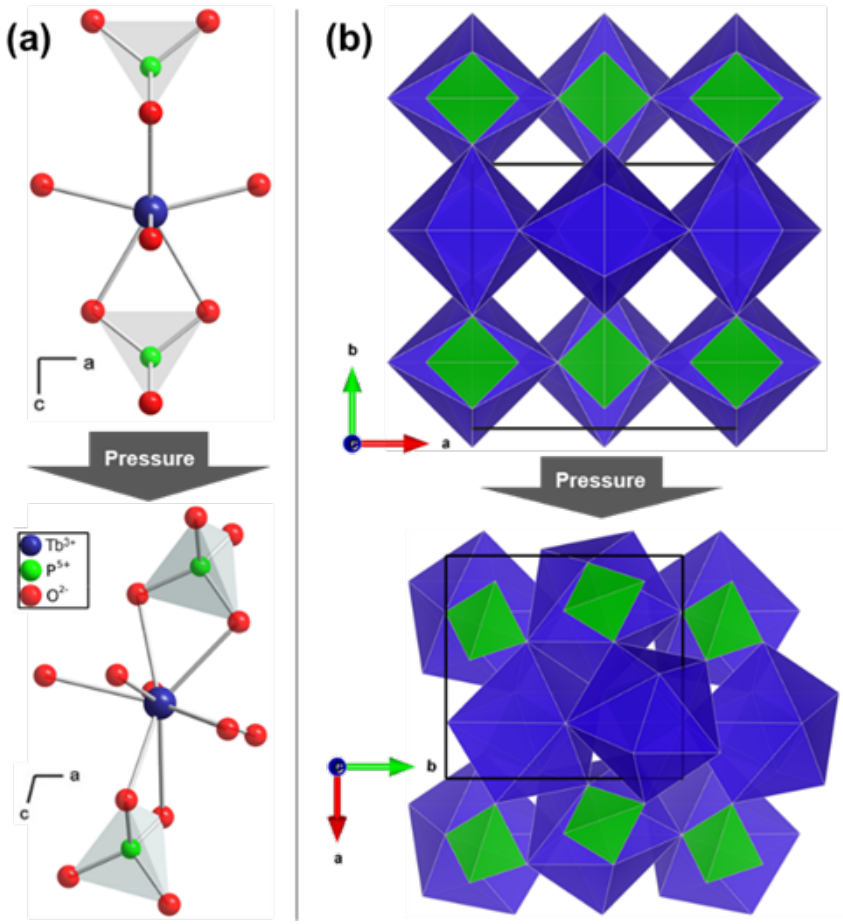

Figure 6.1 Structural changes in $TbPO_4$ during the pressure-induced xenotime-monazite phase transformation. (a) Tb^{3+} local bonding environment. Violet, green, and red spheres represent Tb^{3+}, P^{5+}, and O^{2-} ions, respectively. Adapted from Heuser et al. [8]. (b) [001] views of crystal structure. Violet polyhedra, green tetrahedra, and the black box represent the Tb-O cage, PO_4 groups, and the unit cell boundary, respectively. Crystal structures generated using VESTA software [73].

At high pressure (HP), certain xenotime compositions (RE = Tb-Tm, Y) transform to the monazite structure [20, 81, 93]. This transformation involves an increase in RE-O coordination ($8 \rightarrow 9$), the loss of RE site symmetry ($D_{2d} \rightarrow C_1$), and a volume loss of $\sim$5%. The transformation occurs via the reconfiguration of RE-O bonds, while the PO_4 tetrahedra remain effectively rigid [69].

Finding the onset pressure (P_{onset}) of the xenotime-monazite phase transformation in $REPO_4$s typically requires *in situ* diamond anvil cell (DAC) Raman spectroscopy (RS) or synchrotron x-ray diffraction (XRD). For the composition of interest in this study, $TbPO_4$, RS-based P_{onset} values of $\sim$9.5 GPa and 10.1 GPa have been reported by Tatsi et al. and Musselman et al [16, 17]. Both these studies report some degree of phase transformation irreversibility and utilize pressure-transmitting media which are hydrostatic at relevant pressures (e.g., 4:1 methanol-ethanol and 16:3:1 methanol-ethanol-water). The $TbPO_4$ XRD experiment with neon pressure medium (presented in Chapter 5) shows P_{onset} and transformation end pressure (P_{end}) values of 8.7(6) GPa and 13.7(10) GPa, respectively. Lopez-Solano et al.'s $TbPO_4$ XRD study (also using neon pressure medium) reports a higher P_{onset} of 9.9 GPa; however, this value appears to be an overestimation for reasons discussed in Chapter 5 [18].

Although both RS & synchrotron XRD can deliver unique material insight, they each have significant limitations. RS generally suffers from a low signal-to-noise ratio due to the low probability of Raman scattering, and this ratio only degrades with pressure [107–109]. Moreover, the Raman-active phonon modes observed do not necessarily reflect the RE^{3+} local environment, which is what changes dramatically during the xenotime-monazite phase transformation. RE^{3+} local environment can be probed using certain synchrotron x-ray techniques (e.g., single crystal diffraction, inelastic scattering); however, synchrotron beamtime access is limited.

Given the well-known photoluminescent behavior of RE^{3+} ions, which are intrinsic to (or easily doped into) $REPO_4$s, photoluminescence (PL) spectroscopy is a potentially

promising technique for characterizing the xenotime-monazite transformation due to the high sensitivity of RE^{3+} PL to local bonding environment [25, 110, 111]. Most PL of RE^{3+} ions stems from transitions between 4f configurational states, which are sensitive to changes in local environment. Local environment changes can cause changes in the number of peaks, intensities, and broadness in PL spectra [40]. In the case of xenotime $REPO_4$s, Lösch et al. discovered PL from Eu^{3+} dopants changed with the presence of non-xenotime $REPO_4$ phases in the host [37]. Lösch et al. attribute those PL changes to the impurity phases yielding different Eu^{3+} site symmetries. In addition, Yang et al. reported ambient pressure PL spectra of $TbPO_4$ powder synthesized in the xenotime and metastable monazite phases, and the clearest difference between these spectra is the profile of the green emission band ($\sim$543 nm) [38]. In monazite, this band has a broader and weaker low-energy shoulder and lacks the multiple local maxima seen in xenotime. More detailed analysis of this band is precluded by the limited spectral resolution. The sensitivity of RE^{3+} PL to the local environment has also been observed at HP by Runowski et al., who performed *in situ* DAC PL spectroscopy on an up-converting composition: YPO_4 doped with Yb^{3+} and Tm^{3+} [39]. Runowski et al. note PL band centroids and band intensity ratios (BIRs) of the emitting dopants exhibit continuous changes during loading and discontinuities at pressures consistent with the xenotime-monazite transformation of YPO_4 [39]. In addition to probing RE^{3+} local environment, PL provides stronger signal than RS and greater accessibility than synchrotron x-ray techniques [109].

This *in situ* DAC PL spectroscopy study exploits the PL of intrinsic Tb^{3+} ions in $TbPO_4$ to detect the pressure-induced xenotime-monazite transformation. $TbPO_4$ is the $REPO_4$ chosen for this study as it undergoes the pressure-induced xenotime-monazite transformation, and it has visible PL under UV excitation. Unlike the Runowski et al. study, this work involves direct excitation rather than up-conversion and requires no dopants to generate visible PL [39]. Furthermore, the findings of this HP study are particularly valuable as the direct excitation PL of $TbPO_4$ – or of any other xenotime

$REPO_4$ – has only been reported at ambient pressure [37, 38]. Irreversible pressure-induced changes observed in PL spectra may also serve as indicators of stress history, which may be advantageous in potential ceramic composite applications.

Each $TbPO_4$ PL spectrum contains four bands representing 4f intraconfigurational transitions of Tb^{3+} ($^5D_4 \rightarrow {}^7F_6$, $^5D_4 \rightarrow {}^7F_5$, $^5D_4 \rightarrow {}^7F_4$, and $^5D_3 \rightarrow {}^7F_6$) as shown in Figure 6.2 [29]. Hyperfine splitting ($\sim 10^2$ cm^{-1}) of the energy levels involved in these transitions is induced primarily by crystal field effects and causes each band to consist of multiple peaks [27, 40]. For simplicity in the text, the PL bands generated by the $^5D_4 \rightarrow {}^7F_6$, $^5D_4 \rightarrow {}^7F_5$, $^5D_4 \rightarrow {}^7F_4$, and $^5D_3 \rightarrow {}^7F_6$ emissions are denoted as Bands 1, 2, 3, and 4, respectively.

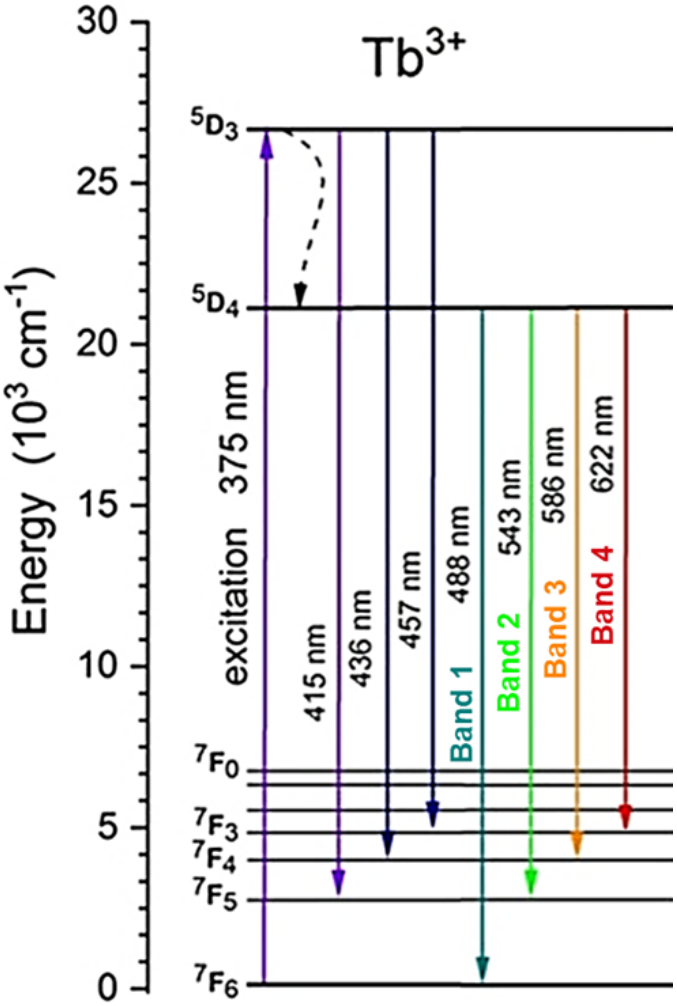

Figure 6.2 Dieke diagram showing the 4f intraconfigurational energy levels of Tb^{3+}. Excitation is shown with the upward arrow and emissions are shown with downward arrows. The dashed and solid downward arrows represent phonon and photon emission, respectively. Adapted from Khan et al [29].

6.5 Materials and Methods

Five DAC experiments (named Exps. 1, 2, 3, 4, and 5) were conducted at room temperature, and they all involved xenotime $TbPO_4$ powder sample, ruby pressure calibrant, 16:3:1 methanol-ethanol-water (MEW) pressure-transmitting medium, and 301 stainless steel gaskets [44]. Exps. 4 and 5 are limited to pressures below the xenotime-monazite P_{onset}, while Exps. 1, 2, and 3 include P_{onset}. In addition, Exps. 3 and 4 do not include PL spectra of the recovered sample (upon returning to 1 atm), while Exps. 1, 2, and 5 do. In each experiment, a 375 nm pulsed laser (290 W/cm^2 average intensity) is used to excite the sample through a 10x objective lens via the $^7F_6 \rightarrow {}^5D_3$ transition. The emitted light from the sample is then focused and collected via a monochromator, where the PL spectra are recorded on a CCD (charge-coupled device) camera. Additional details on sample synthesis, phase purity, and experimental details including DAC configuration and PL measurement are provided in the Supporting Information. In addition, the number in parentheses after a pressure value represents the standard deviation of the last digit of the pressure.

6.6 Results and Discussion

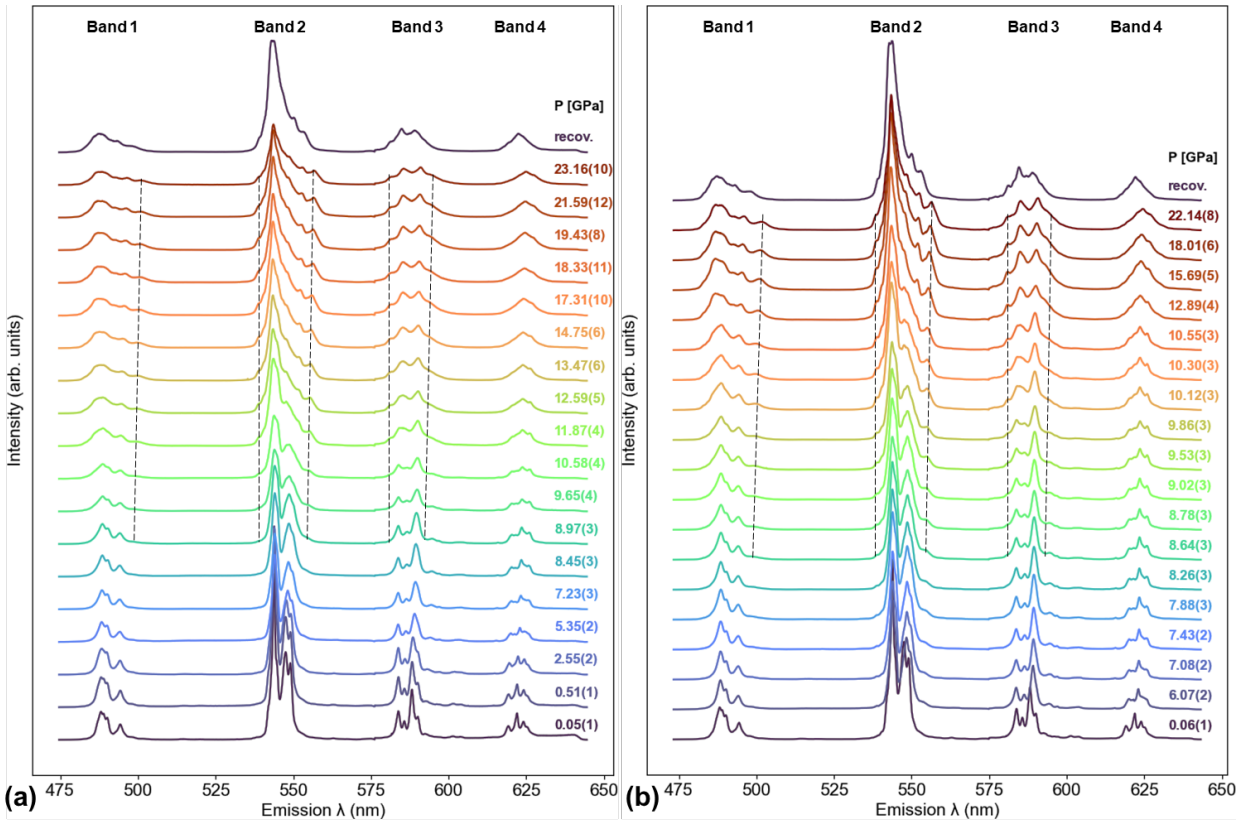

Figure 6.3 Pressure evolution of $TbPO_4$ PL spectra from (a) Exp. 1 and (b) Exp. 2. Both experiments show pressures above P_{onset} as well as the spectrum of the recovered sample (at 1 atm). Numbers in parentheses after pressure values represent the standard deviation in the last digit of the pressure. Dashed lines are visual guides for peaks emerging at HP.

Figure 6.3 shows increasing pressure induces a centroid red-shift, broadening, and intensity loss in all four PL bands. The red-shift is due to the stronger crystal field generated by shrinking Tb-O bonds, while the broadening can be attributed to strain, local symmetry distortion, and defect generation [39, 108, 112]. The intensity loss is likely attributable to pressure-induced increases in electron-phonon coupling, phonon energy, and modified selection rules [39, 40]. In the spectra collected after decompression (recov.), the red shift is largely reversible, while the broadening is largely maintained; these effects are exemplified by Band 4 in Figure 6.3 (a) and Figure 6.3 (b). However, some broadening is reversed upon pressure release as revealed by the full-width at half-maximum (FWHM) values of Band 4 (see Figure F3). The partial reversibility of PL FWHM is likely attributable to residual strain, distortion, and defects as well as metastable monazite remaining in the sample after decompression. Intensity increases upon pressure release; however, intensity is not quantitatively analyzed because it varies with optical focus, which is manually adjusted at each pressure step in the experiments. Quantitative band centroid data and additional reversibility analysis are presented later in the text. Across three separate experiments (including Exp. 3 shown in Figure F4), PL peaks newly emerge or grow at pressures near the XRD-based xenotime-monazite P_{onset} of 8.7(6) GPa (as shown in Figure 6.3(a) and Figure 6.3(b)). Such peaks are located in Band 1 at ∼500 nm, in Band 2 at ∼535 nm and ∼555 nm, and in Band 3 at ∼580 nm and ∼590 nm. The presence of additional peaks suggests the local environment loses symmetry, which is consistent with the Tb^{3+} point group change ($D_{2d} \rightarrow C_1$) during the xenotime-monazite transformation. The evolution of the overall shape of Band 2 above 10 GPa is also consistent with the PL spectrum of monazite $TbPO_4$ reported by Yang et al. [38]. The shape of Bands 1, 3, and 4 are not compared to those in Yang et al. because these bands are not markedly different between the xenotime and monazite phases. Nevertheless, the emergence and growth of PL peaks at pressures consistent with the XRD-based xenotime-monazite P_{onset} of 8.7(6) GPa strongly indicates that the PL of Tb^{3+} reveal the onset of xenotime-monazite phase

transformation in $TbPO_4$. PL spectra from Exp. 3, as shown in Figure F4, also included pressures above P_{onset} and yielded findings consistent with those of Exps. 1 and 2. PL spectra from Exps. 4 and 5 (see Figures F5 and F6) did not exceed P_{onset} but did show the red-shift, broadening, and intensity loss observed in Exps. 1 and 2 below P_{onset}. Exp. 5 also shows residual broadening in the recovered sample, which is consistent with Exps. 1 and 2 and indicates residual broadening is not caused exclusively by phase transformation.

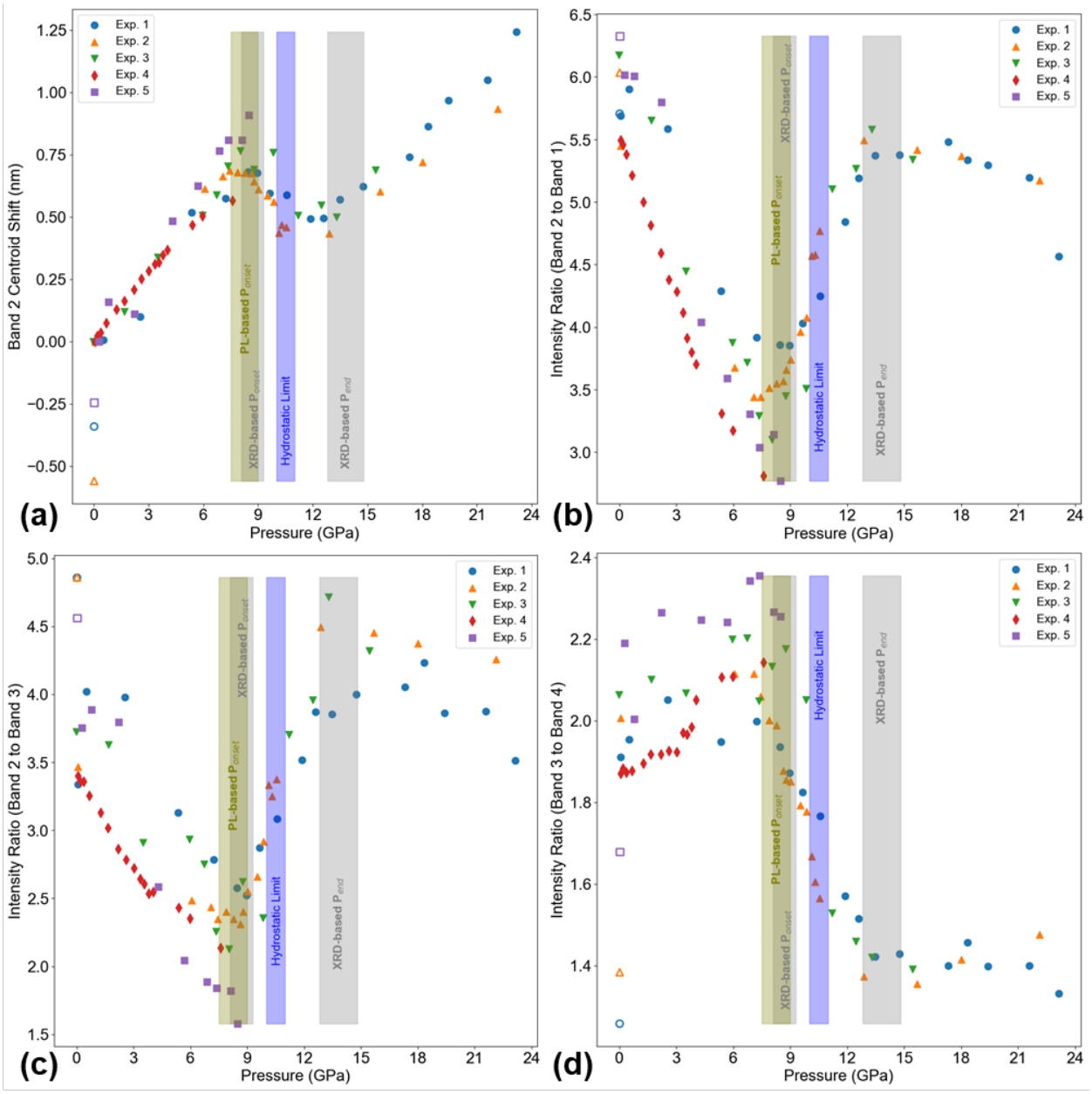

Figure 6.4 Pressure evolution of selected $TbPO_4$ PL band metrics compiled from all experiments. The olive, blue, and two grey rectangles represent pressure ranges corresponding to the PL-based P_{onset}, the hydrostatic limit of MEW, the XRD-based P_{onset}, and the XRD-based P_{end} (as reported in Chapter 5), respectively. Open symbols represent data from recovered sample at 1 atm. Pressure error bars are within the symbols. (a) Band 2 centroid shift (with respect to its initial value in each experiment). (b) Ratio of the intensity of Band 2 to that of Band 1. (c) Ratio of the intensity of Band 2 to that of Band 3. (d) Ratio of the intensity of Band 3 to that of Band 4.

Figure 6.4 shows the pressure dependence of selected PL band metrics, which appear to be indicators of the xenotime-monazite transformation. These band metrics are also placed in context with the hydrostatic limit of MEW (10.5(5) GPa) and the XRD-based $TbPO_4$ xenotime-monazite coexistence range during phase transformation (8.7(6) GPa – 13.7(10) GPa) as reported in Chapter 5 [46]. The pressure-dependence of other PL band metrics with weaker changes around P_{onset} are shown in Figures F7 and F8. Figure 6.4 (a) shows shifts in the Band 2 centroid (i.e., change from its initial value at ∼0 GPa). The Band 2 centroid red-shifts until ∼8 GPa (as marked by the olive bar), which is statistically significantly lower than the hydrostatic limit and consistent with the XRD-based P_{onset}). After ∼8 GPa, the Band 2 centroid begins to blue-shift and then red-shifts again at ∼13.5 GPa (consistent with the XRD-based P_{end}). The blue-shift may be understood as a weakening of the crystal field due to Tb-O bond reconfiguration during the xenotime-monazite transformation. Figure 6.4 (a) also shows the Band 2 centroid does not return to its initial value in the recovered sample (open data points at ∼1 atm), and this residual centroid shift is noticeably greater in experiments in which phase transformation occurred. The Band 3 centroid behaves similarly to the Band 2 centroid in the aforementioned ways and is shown in Figure F7(b). Band centroid hysteresis suggests some irreversible pressure-induced changes (i.e., material stress history) are detectable using PL band metrics.

In Figure 6.4, panels (b), (c), and (d) show the pressure dependence of selected BIRs. Similar to the Band 2 centroid, these BIRs exhibit clear trend changes prior to P_{onset} and at P_{end}. Figure 6.4(b) shows the 2:1 BIR decreases until ∼8 GPa, starts increasing steeply, then appears to stabilize or slightly decrease at P_{end}. Figure 6.4 (c) shows a nearly identical behavior in the 2:3 BIR. Figure 6.4(d) shows the 3:4 BIR undergoes less dramatic trend changes in the opposite directions of the trend changes in the previous BIRs. The first 3:4 BIR trend change also occurs at a slightly lower pressure of ∼7.5 GPa. Across all three BIRs, the pressure range in which the first trend change occurs (i.e., the inferred

PL-based P_{onset} shown as an olive rectangle) is always lower than the hydrostatic limit and coincides with the XRD-based P_{onset}. Figure 6.4 also shows the inferred PL-based P_{onset} varies between band metrics for a given experiment. Such variation between band metrics is also observed during the xenotime-monazite transformation of YPO_4:Yb^{3+},Tm^{3+} and is likely caused by variation in the symmetry-sensitivity of the various emissions involved [39, 40]. When considering the data points from the recovered samples, the 2:3 BIR (Figure 6.4(c)) appears to have a larger residual hysteresis than the 2:1 and 3:4 BIRs (Figure 6.4(b) and Figure 6.4(d)). In addition, the 3:1 BIR shown in Figure F8(a) exhibits a residual hysteresis in the recovered sample, and this hysteresis is greater in experiments in which phase transformation occurred. Overall, the magnitude of the pressure-induced changes of the 2:1, 2:3, and 3:4 BIRs and the magnitude of their hystereses make them better potential indicators of stress history than band centroids.

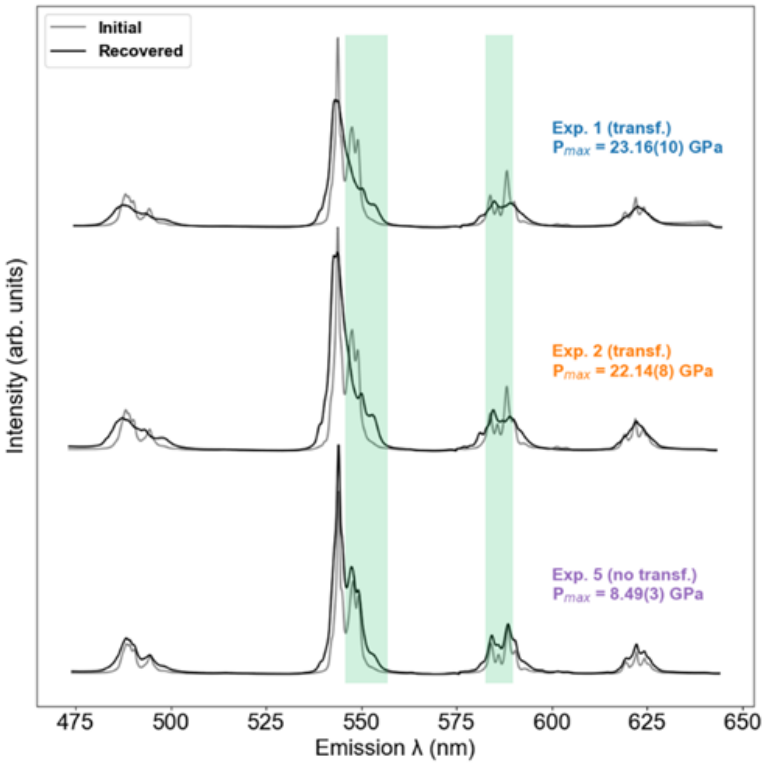

Figure 6.5 Initial and recovered $TbPO_4$ PL spectra overlaid for comparison from Exps. 1, 2, and 5. Sections of the spectra which most clearly indicate a history of phase transformation are highlighted in green.

Figure 6.5 overlays initial and recovered $TbPO_4$ PL spectra from Exps. 1, 2, and 5, showing pressure-induced PL changes are more reversible in the absence of phase transformation (Exp. 5). When phase transformation does not occur (Exp. 5), residual broadening is still present in the recovered spectrum, indicating pressure-induced strain, distortion, and defect generation are not fully reversible. When phase transformation occurs (Exps. 1 and 2), the recovered spectra show residual broadening as well as additional peaks indicative of metastable monazite. The clearest indicators of phase transformation history in Figure 6.5 are the sections of Bands 2 and 3 highlighted in green.

6.7 Conclusions

In conclusion, this study demonstrates the pressure-induced xenotime-monazite phase transformation of $TbPO_4$ can be probed using direct excitation PL spectroscopy. Under UV excitation, the intrinsic Tb^{3+} ions generate four PL emission bands in the visible range, and these bands shift and broaden with pressure. Qualitative analysis of PL spectra shows additional peaks emerging at HP, which is consistent with the Tb^{3+} site symmetry loss during transformation. Quantitative analysis shows the Band 2 centroid and the 2:1, 2:3, and 2:4 BIRs undergo clear trend changes at pressures coinciding with the XRD-based P_{onset} and P_{end}. The close agreement between the inferred PL-based P_{onset} and the XRD-based P_{onset} shows changes in the RE^{3+} crystal field as observed in PL spectroscopy can be used to detect the xenotime-monazite transformation. In addition, PL spectra of the recovered samples indicate metastable monazite exists after decompression, confirming the irreversibility of the xenotime-monazite phase transformation. Hysteresis in certain PL band metrics also serves as potential gauges of the stress history of the sample. Given the ease of RE substitution in $REPO_4$s and other materials, the analysis of direct excitation (down-conversion) RE^{3+} PL in this work can potentially be extended beyond $TbPO_4$ to other RE-containing oxide compounds (e.g., $REXO_4$s where X = V, As, Sb, W, Nb, or Mo).

6.8 Acknowledgments

The authors thank Dr. Ivar Reimanis for lending his Diacell Helios DAC. This research was supported by the National Science Foundation under Award No. DMR-1352499 and (M.J.C.) by start-up funds from the Colorado School of Mines. J.S. was supported by the Department of Defense through the National Defense Science & Engineering Graduate Fellowship Program.

6.9 Supporting Information

Appendix F contains additional details on sample synthesis, phase purity, powder morphology, PL measurement, and a table showing experiment specific details. Additional figures in Appendix F show Band 4 FWHM data, stacked PL spectra from Exps. 3-5, pressure evolution of other centroids (Bands 1, 3, and 4) and other BIRs (3:1, 1:4, and 2:4), as well as loading rates from all experiments.

CHAPTER 7
SUMMARY AND FUTURE WORK

This chapter provides a summary of the work presented in this dissertation as well as potential future research directions.

7.1 Thesis Summary

Rare earth orthophosphates ($REPO_4$s) are an increasingly relevant class of ceramics attracting multi-disciplinary interest from research fields ranging from geoscience to optics to ceramic matrix composite (CMC) engineering [1]. The last of these fields is a key motivator for this dissertation and seeks to exploit the refractory nature of $REPO_4$s for fiber coating applications in oxide-oxide CMCs relevant to aerospace components (e.g., combustors, fuel injection nozzles). The extreme conditions associated with application environments motivate the consideration of $REPO_4$s (like $LaPO_4$), which are more oxidation-resistant than traditional fiber coating candidates (e.g., graphite, hexagonal boron nitride) [5, 14]. Among $REPO_4$ compositions, those that transform under pressure offer the unique possibility of additional plasticity and toughening mechanisms. In fact, compositions which undergo the xenotime-monazite phase transformation result in lower fiber push-out stresses than non-transforming $LaPO_4$ [7, 15]. Unfortunately, the kinetics of $REPO_4$ xenotime-monazite phase transformations are not fully established, and the shear-dependence of phase transformation even less so. Moreover, the excellent photoluminescence (PL) characteristics of RE^{3+} ions have yet to be fully exploited in mechanically-motivated, high-pressure $REPO_4$ research. PL spectroscopy offers stronger signal than Raman spectroscopy and more directly probes the RE^{3+} local environment (where the most dramatic changes occur during phase transformation) [107–109]. PL spectroscopy is also significantly more accessible than synchrotron beamtime, and has the potential to accelerate high-pressure research. Developing a clear understanding of the

relationship between stress and PL emissions can further enable remote, optical stress-sensing or stress history-sensing functionalities in $REPO_4$s. This dissertation aims to elucidate the kinetics, shear-dependence, and composition-dependence of the xenotime-monazite phase transformation using *in situ* diamond anvil cell (DAC) XRD and PL experiments.

First, the $DyPO_4$ xenotime-monazite phase transformation and its shear-dependence were investigated using *in situ* DAC synchrotron XRD. This work was published in *Physical Review B* and is presented in Chapter 3 [81]. The high-pressure monazite phase of $DyPO_4$ was crystallographically confirmed, and the xenotime-monazite transformation onset pressure (P_{onset}) was found to be 9.1 GPa, which is dramatically lower than previously reported values based on Raman spectroscopy (RS). Further analysis of the RS data reported by Musselman et al. showed RS is insufficient for accurately determining the the P_{onset} of the xenotime-monazite transformation in $DyPO_4$ [20]. The new, XRD-based P_{onset} of $DyPO_4$ also shows the xenotime-monazite P_{onset} is not linear with RE^{3+} ionic radius (as is commonly assumed in literature); rather, it is discontinuous at some critical ionic radius between those of Y^{3+} and Dy^{3+}. Moreover, this study was the first to systematically interrogate the effect of shear on the xenotime-monazite phase transformation and used KCl as a pressure-transmitting medium (PTM) to enable compression with a significant shear component. With KCl as the PTM, the xenotime-monazite P_{onset} dropped to 7.0 GPa, showing transformation onset is sensitive to stress state. Furthermore, the wide pressure range ($\geq$ 5.7 GPa) of xenotime-monazite phase coexistence suggests this transformation is diffusional rather than martensitic. Connecting back to potential CMC fiber coating applications, previously reported $REPO_4$ P_{onset} values (determined under hydrostatic conditions) were too high to merit consideration for this application. This study shows P_{onset} values measured under hydrostatic compression are not sufficient for screening $REPO_4$ fiber coating candidates because these materials could potentially transform at lower pressures in a high-shear environment like a CMC

fiber-matrix interface. The reduction of P_{onset} under non-hydrostatic conditions also suggests a wider range of $REPO_4$ compositions (i.e., those with higher P_{onset} values under hydrostatic compression) could be considered for CMC fiber coating applications.

Second, knowledge of the phase transformation pathway of $DyPO_4$ was extended to previously untested pressures using *in situ* DAC synchrotron x-ray diffraction. This work was published in *Crystals* and is presented in Chapter 4 [93]. The pressure range of the $DyPO_4$ xenotime-monazite phase coexistence is determined to be 7.6(15) GPa; this value was not obtained in Chapter 3 because those experiments did not go to high enough pressures. The phase coexistence range determined in Chapter 4 also confirms the sluggish nature of the xenotime-monazite phase transformation and provides further evidence that transformation proceeds via a diffusional, nucleation and growth-based mechanism. In addition, this study shows a post-monazite $DyPO_4$ phase emerges at 13.9(10) GPa, and this phase likely adopts the scheelite structure. The determination of scheelite is consistent with the phase transformation pathways reported in experimental and computational literature [12, 13, 18, 80]. The experiment in this study also compresses $DyPO_4$ at a rate that is an order of magnitude higher than the rates tested in Chapter 3, yet the xenotime-monazite P_{onset} does not increase to a statistically significant extent. Additionally, this study compiles the latest XRD-based DAC studies of single-RE $REPO_4$s (under hydrostatic media) into one figure (Figure 4.2) and is the first of its kind to show phase coexistence ranges in addition to phase transformations.

Third, *in situ* DAC synchrotron XRD was performed to evaluate the shear-dependence of the $TbPO_4$ xenotime-monazite phase transformation and extend the $DyPO_4$ shear study presented in Chapter 3. This work is soon to be submitted to *Solids* and is presented in Chapter 5. The experiments performed in this study involve three PTMs: neon, KCl, and "none" (i.e., the cell packed with sample, pressure markers, and no PTM material). In the "none" PTM condition, the sample is effectively the PTM. Each step in the neon-KCl-none PTM sequence represents an order of magnitude increase in the PTM bulk modulus. The

$TbPO_4$ experiment using neon PTM shows a xenotime-monazite P_{onset} of 8.7(6) GPa, which is statistically significantly lower than the previously reported XRD-based P_{onset} of 9.9 GPa (also measured with neon PTM) [18]. Furthermore, experiments show a systematic and statistically significant lowering of the $TbPO_4$ xenotime-monazite P_{onset} going from neon (8.7(6) GPa) to KCl (5.6(4) GPa) to "none" (4.4(3) GPa). For each of the three aforementioned PTMs, the P_{onset} values of $TbPO_4$ are consistently lower than those of $DyPO_4$; this discrepancy is likely due to the monazite phase being more enthalpically favorable in $TbPO_4$ than in $DyPO_4$. $TbPO_4$ experiments also show the xenotime-monazite phase coexistence range widens with increasing non-hydrostaticity; this effect has been observed in other materials and may be caused by inhomogeneous transformation progression in a given volume of material [22, 47]. The $TbPO_4$ experiment with no medium shows the lowest P_{onset} reported for any $REPO_4$ to date, provides potential experimental proof of scheelite as the post-monazite phase, and corroborates Hay et al.'s *ex situ* observations of phase transformation in indented xenotime $TbPO_4$ [7]. Taking a step back, this study shows the benefits of $REPO_4$ phase transformation (i.e., transformation plasticity and transformation toughening) can be exploited at lower pressures and over a wider range of pressures than was previously understood.

Fourth, the $TbPO_4$ xenotime-monazite phase transformation was probed using *in situ* DAC PL spectroscopy. This work is presented in Chapter 6 and will soon be submitted to *ACS Materials Letters*. These experiments demonstrate PL spectroscopy, a technique with stronger signal than Raman spectroscopy and greater accessibility than synchrotron techniques, can be employed to detect the pressure-induced xenotime-monazite phase transformation of $TbPO_4$. At pressures consistent with the XRD-based P_{onset} reported in Chapter 5, additional $TbPO_4$ PL peaks emerge, and PL band metrics (centroid and intensity ratios) show clear trend changes. The same band metrics also exhibit trend changes at pressures consistent with the end of transformation (P_{end}) as determined in Chapter 5. PL spectra of $TbPO_4$ recovered after decompression confirm the irreversibility

of the xenotime-monazite transformation and exhibit residual broadening. Importantly, this residual broadening and other irreversible pressure-induced PL changes can indicate stress history in $TbPO_4$. In addition, pressure-induced PL changes appear to be more reversible when $TbPO_4$ has not experienced pressures high enough to induce phase transformation. More broadly, this work provides the first high-pressure direct excitation (down-conversion) PL dataset of $TbPO_4$ or any other xenotime $REPO_4$, and the PL band metric analysis shown here can be extended beyond $TbPO_4$ to other RE-based oxide compounds (e.g., REXO4s, X = V, As, Sb, W, Nb, or Mo). The PL dataset generated in this study also offers unprecedented spectral resolution, enabling more detailed, fundamental analysis of the effect of pressure and phase transformation on 4f orbitals.

7.2 Future Work

This dissertation provides a basis for assessing the shear-dependence of the pressure-induced $REPO_4$ xenotime-monazite phase transformation and for exploiting RE^{3+} PL to characterize this transformation. To gain more fundamental insight and enable new applications, additional research avenues can be pursued.

The XRD experiments show strategic choice of PTM can enable DAC testing with varying degrees of non-hydrostatic stress; however, further exploration is necessary to quantify the shear generated by solid PTMs at high pressure. Quantification may be achieved by probing shear wave propagation (via acoustic techniques) or by analyzing XRD peaks of gold or other well-calibrated DAC pressure standards without significant overlap from other phases in the DAC. Gauging shear strains directly from the sample requires analyzing XRD spots collected via single crystal XRD and relaxing unit cell symmetry constraints. *In situ* DAC single crystal XRD with hydrostatic PTMs or density functional theory (DFT) calculations are also necessary to determine the stiffness tensor constants for xenotime compositions (only the tensors for $HoPO_4$ and $TmPO_4$ have been reported to date) [19]. Knowing stiffness tensor constants may also aid in determining atomic displacements under non-hydrostatic stress states, which can be challenging even with

single crystal XRD [108].

Promising future research also includes further *in situ* DAC PL experiments. Because PL emissions are particularly sensitive to symmetry distortions, performing PL experiments with non-hydrostatic media can shed light on the effect of shear on the RE^{3+} crystal field. Successfully collecting high-quality PL spectra with non-hydrostatic PTMs can also enable systematic shear studies without the need for synchrotron beamtime. In addition, testing non-luminescent $REPO_4$ compositions doped with luminescent RE^{3+}s like Tb^{3+} would further accelerate the progress of pressure-induced phase transformation research. Moreover, DFT simulations at high pressure can help in clarifying and assigning specific 4f intraconfigurational transitions to the several PL peaks that exist within a given PL band. Fundamental understanding of the individual PL peaks then enables experimental PL data to be reliably fit, and in turn, more material detail can be extracted from a given spectrum. Such insight may be valuable for more quantitatively assessing the stress-sensing and stress history-sensing capability of $REPO_4$s. Quantitative assessment of these mechano-optical phenomena may open the door to optical sensing functions in CMC fiber coatings or other extreme environment applications.

REFERENCES

[1] Lynn A. Boatner. Synthesis, structure, and properties of monazite, pretulite, and xenotime. *Reviews in Mineralogy and Geochemistry*, 48:87–121, 1 2002. ISSN 1529-6466. doi: 10.2138/rmg.2002.48.4. URL https://pubs.geoscienceworld.org/rimg/article/48/1/87-121/110613.

[2] N. M. Vielreicher, D. I. Groves, I. R. Fletcher, N. J. McNaughton, and B. Rasmussen. Hydrothermal monazite and xenotime geochronology: A new direction for precise dating of orogenic gold mineralization. *SEG Discovery*, 70:1–16, 4 2003. ISSN 2694-0655. doi: 10.5382/SEGnews.2003-53.fea. URL https://pubs.geoscienceworld.org/segdiscovery/article/doi/10.5382/SEGnews.2003-53.fea/607608/Hydrothermal-Monazite-and-Xenotime-Geochronology-A.

[3] A A Kaminskii, M Bettinelli, A Speghini, H Rhee, H J Eichler, and G Mariotto. Tetragonal ypo ¡sub¿4¡/sub¿ – a novel srs-active crystal. *Laser Physics Letters*, 5: 367–374, 5 2008. ISSN 1612-2011. doi: 10.1002/lapl.200810005. URL https://iopscience.iop.org/article/10.1002/lapl.200810005.

[4] U. Sasum, M. Kloss, A. Rohmann, L. Schwarz, and D. Haberland. Optical properties of some rare earth and alkaline rare earth orthophosphates. *Journal of Luminescence*, 72-74:255–256, 6 1997. ISSN 0022-2313. doi: 10.1016/S0022-2313(96)00381-X.

[5] Peter E.D. Morgan and David B. Marshall. Functional interfaces for oxide/oxide composites. *Materials Science and Engineering A*, 162:15–25, 1993. ISSN 09215093. doi: 10.1016/0921-5093(90)90026-Y.

[6] Emmanuel E. Boakye, Pavel Mogilevsky, Randall S. Hay, and Geoff E. Fair. Synthesis and phase composition of lanthanide phosphate nanoparticles lnpo4 (ln=la, gd, tb, dy, y) and solid solutions for fiber coatings. *Journal of the American Ceramic Society*, 91:3841–3849, 2008. ISSN 00027820. doi: 10.1111/j.1551-2916.2008.02737.x.

[7] R. S. Hay, P. Mogilevsky, and E. Boakye. Phase transformations in xenotime rare-earth orthophosphates. *Acta Materialia*, 61:6933–6947, 2013. ISSN 13596454. doi: 10.1016/j.actamat.2013.08.005. URL http://dx.doi.org/10.1016/j.actamat.2013.08.005.

[8] Julia M. Heuser, Stefan Neumeier, Lars Peters, Hartmut Schlenz, Dirk Bosbach, and Guido Deissmann. Structural characterisation of metastable tb- and dy-monazites. *Journal of Solid State Chemistry*, 273:45–52, 2019. ISSN 1095726X. doi: 10.1016/j.jssc.2019.02.028. URL https://doi.org/10.1016/j.jssc.2019.02.028.

[9] Yunxiang Ni, John M Hughes, Anthony N Mariano, N I Et, and A L Crystal. Crystal chemistry of the monazite and xenotime structures. *American Mineralogist*, 80:21–26, 1995.

[10] Nicolas Clavier, Renaud Podor, and Nicolas Dacheux. Crystal chemistry of the monazite structure. *Journal of the European Ceramic Society*, 31:941–976, 2011. ISSN 09552219. doi: 10.1016/j.jeurceramsoc.2010.12.019. URL http://dx.doi.org/10.1016/j.jeurceramsoc.2010.12.019.

[11] R. Lacomba-Perales, D. Errandonea, Y. Meng, and M. Bettinelli. High-pressure stability and compressibility of a po4 (a=la, nd, eu, gd, er, and y) orthophosphates: An x-ray diffraction study using synchrotron radiation. *Physical Review B - Condensed Matter and Materials Physics*, 81:1–38, 2010. ISSN 10980121. doi: 10.1103/PhysRevB.81.064113.

[12] F. X. Zhang, M. Lang, R. C. Ewing, J. Lian, Z. W. Wang, J. Hu, and L. A. Boatner. Pressure-induced zircon-type to scheelite-type phase transitions in ybpo4 and lupo4. *Journal of Solid State Chemistry*, 181:2633–2638, 2008. ISSN 1095726X. doi: 10.1016/j.jssc.2008.06.042.

[13] F. X. Zhang, J W Wang, M Lang, J M Zhang, R C Ewing, and L A Boatner. High-pressure phase transitions of scpo4 and ypo4. *Physical Review B - Condensed Matter and Materials Physics*, 80, 2009. ISSN 10980121. doi: 10.1103/PhysRevB.80.184114.

[14] Peter E.D. Morgan and David B. Marshall. Ceramic composites of monazite and alumina. *Journal of the American Ceramic Society*, 78:1553–1563, 6 1995. ISSN 1551-2916. doi: 10.1111/J.1151-2916.1995.TB08851.X. URL https://onlinelibrary.wiley.com/doi/full/10.1111/j.1151-2916.1995.tb08851.xhttps://onlinelibrary.wiley.com/doi/abs/10.1111/j.1151-2916.1995.tb08851.xhttps://ceramics.onlinelibrary.wiley.com/doi/10.1111/j.1151-2916.1995.tb08851.x.

[15] R. S. Hay, E. E. Boakye, P. Mogilevsky, G. E. Fair, T. A. Parthasarathy, and J. E. Davis. Transformation plasticity in (gdx dy1-x) po 4 fiber coatings during fiber push out. *Journal of the American Ceramic Society*, 96:1586–1595, 2013. ISSN 00027820. doi: 10.1111/jace.12301.

[16] Matthew A. Musselman. In situ raman spectroscopy of pressure-induced phase transformations in dypo4 and gdxdy(1-x)po4. *Mines Theses and Dissertations*, 2017.

[17] A. Tatsi, E. Stavrou, Y. C. Boulmetis, A. G. Kontos, Y. S. Raptis, and C. Raptis. Raman study of tetragonal tbpo4 and observation of a first-order phase transition at high pressure. *Journal of Physics Condensed Matter*, 20, 2008. ISSN 09538984. doi: 10.1088/0953-8984/20/42/425216.

[18] J. López-Solano, P. Rodríguez-Hernández, A. Muñoz, O. Gomis, D. Santamaría-Perez, D. Errandonea, F. J. Manjón, R. S. Kumar, E. Stavrou, and C. Raptis. Theoretical and experimental study of the structural stability of tbpo4 at high pressures. *Physical Review B - Condensed Matter and Materials Physics*, 81:1–9, 2010. ISSN 10980121. doi: 10.1103/PhysRevB.81.144126.

[19] O. Gomis, B. Lavina, P. Rodríguez-Hernández, A Muñoz, R Errandonea, D. Errandonea, and M. Bettinelli. High-pressure structural, elastic, and thermodynamic properties of zircon-type hopo 4 and tmpo 4. *Journal of Physics: Condensed Matter*, 29:095401, 3 2017. ISSN 0953-8984. doi: 10.1088/1361-648X/aa516a. URL https://iopscience.iop.org/article/10.1088/1361-648X/aa516a.

[20] Matthew A. Musselman, Taylor M. Wilkinson, Bianca Haberl, and Corinne E. Packard. In situ raman spectroscopy of pressure-induced phase transformations in polycrystalline tbpo4, dypo4, and gdxdy(1-x)po4. *Journal of the American Ceramic Society*, 101:2562–2570, 2018. ISSN 15512916. doi: 10.1111/jace.15374.

[21] E. Stavrou, A. Tatsi, C. Raptis, I. Efthimiopoulos, K. Syassen, † A Muñoz, P. Rodríguez-Hernández, J. López-Solano, M. Hanfland, A. Muñoz, P. Rodríguez-Hernández, J. López-Solano, and M. Hanfland. Effects of pressure on the structure and lattice dynamics of tmpo4: Experiments and calculations. *Physical Review B - Condensed Matter and Materials Physics*, 85:24117, 2012. ISSN 10980121. doi: 10.1103/PhysRevB.85.024117.

[22] D. Santamaría-Pérez, L. Gracia, G. Garbarino, A. Beltrán, R. Chuliá-Jordán, O. Gomis, D. Errandonea, Ch Ferrer-Roca, D. Martínez-García, and A. Segura. High-pressure study of the behavior of mineral barite by x-ray diffraction. *Physical Review B - Condensed Matter and Materials Physics*, 84:1–8, 2011. ISSN 10980121. doi: 10.1103/PhysRevB.84.054102.

[23] S. V. Ushakov, K. B. Helean, A. Navrotsky, and L. A. Boatner. Thermochemistry of rare-earth orthophosphates. *Journal of Materials Research*, 16:2623–2633, 2001. ISSN 08842914. doi: 10.1557/JMR.2001.0361.

[24] Pavel Mogilevsky. On the miscibility gap in monazite-xenotime systems. *Physics and Chemistry of Minerals*, 34:201–214, 2007. ISSN 03421791. doi: 10.1007/s00269-006-0139-1.

[25] Suchinder Sharma, Thomas Behm, Thomas Köhler, Jan Beyer, Richard Gloaguen, and Johannes Heitmann. Library of uv-visible absorption spectra of rare earth orthophosphates, lnpo4 (ln = la-lu, except pm). *Crystals*, 10:593, 2020. ISSN 2073-4352. doi: 10.3390/cryst10070593.

[26] Robert Withnall and Jack Silver. Physics of light emission from rare-earth doped phosphors. *Handbook of Visual Display Technology*, pages 1019–1028, 2012. doi: 10.1007/978-3-540-79567-4_68. URL https://link.springer.com/referenceworkentry/10.1007/978-3-540-79567-4_68.

[27] GH Dieke, HM Crosswhite, and B Dunn. Emission spectra of the doubly and triply ionized rare earths. *Journal of the Optical Society of America (US)*, 51, 1961.

[28] Xian Qin, Xiaowang Liu, Wei Huang, Marco Bettinelli, and Xiaogang Liu. Lanthanide-activated phosphors based on 4f-5d optical transitions: Theoretical and experimental aspects. *Chemical Reviews*, 117:4488–4527, 3 2017. ISSN 15206890. doi: 10.1021/ACS.CHEMREV.6B00691. URL https://pubs.acs.org/doi/full/10.1021/acs.chemrev.6b00691.

[29] D. T. Khan, N. T. Dang, S. H. Jabarov, T. G. Naghiyev, R. M. Rzayev, T. Q. Nguyen, H. V. Tuyen, N. T. Thanh, and L. V.T. Son. Study on luminescent properties of tb3+ and sm3+ co-doped casio3 phosphors for white light emitting diodes. *Materials Research Express*, 7:016507, 12 2019. ISSN 2053-1591. doi: 10.1088/2053-1591/AB5AB8. URL https://iopscience.iop.org/article/10.1088/2053-1591/ab5ab8https://iopscience.iop.org/article/10.1088/2053-1591/ab5ab8/meta.

[30] Franziska Steudel, Sebastian Loos, Bernd Ahrens, and Stefan Schweizer. Quantum efficiency and energy transfer processes in rare-earth doped borate glass for solid-state lighting. *Journal of Luminescence*, 170:770–777, 2 2016. ISSN 0022-2313. doi: 10.1016/J.JLUMIN.2015.07.032.

[31] A. J. Wojtowicz, D. Wisniewski, A. J. Wojtowicz, D. Wisniewski, A. Lempicki, and L. A. Boatner. Scintillation mechanisms in rare earth orthophosphates. *Radiation Effects and Defects in Solids*, 135:305–310, 1995. ISSN 10294953. doi: 10.1080/10420159508229856.

[32] Matthew J. Dejneka, Alexander Streltsov, Santona Pal, Anthony G. Frutos, Christy L. Powell, Kevin Yost, Po Ki Yuen, Uwe Müller, and Joydeep Lahiri. Rare earth-doped glass microbarcodes. *Proceedings of the National Academy of Sciences of the United States of America*, 100:389–393, 1 2003. ISSN 00278424. doi: 10.1073/PNAS.0236044100/ASSET/4939EF12-6004-47E6-898D-4172C0BAA713/ASSETS/GRAPHIC/PQ0236044004.JPEG. URL https://www.pnas.org.

[33] Vineet Kumar, Sukhvir Singh, and Santa Chawla. Fabrication of dual excitation, dual emission nanophosphor with broad uv and ir excitation through simultaneous doping of triple rare earth ions er3+, yb3+, eu3+ in gdpo4. *Superlattices and Microstructures*, 79:86–95, 3 2015. ISSN 0749-6036. doi: 10.1016/J.SPMI.2014.12.003.

[34] Christoph Lenz, Gordon Thorogood, Robert Aughterson, Mihail Ionescu, Daniel J. Gregg, Joel Davis, and Gregory R. Lumpkin. The quantification of radiation damage in orthophosphates using confocal µ-luminescence spectroscopy of nd3+. *Frontiers in Chemistry*, 7:13, 2019. ISSN 22962646. doi: 10.3389/FCHEM.2019.00013/BIBTEX.

[35] Robert Krewinkel, Jens Farber, Ulrich Orth, Dirk Frank, Martin Lauer, Christopher Pilgrim, Alvaro Yañez Gonzalez, Jorg Feist, Raffaele Saggese, Stephane Berthier, and Silvia Araguas-Rodriguez. Validation of surface temperature measurements on a combustor liner under full-load conditions using a novel thermal history paint. *Journal of Engineering for Gas Turbines and Power*, 139:41508–41509, 4 2017. ISSN 15288919. doi: 10.1115/1.4034724/444268. URL https://asmedigitalcollection.asme.org/gasturbinespower/article/139/4/041508/444268/Validation-of-Surface-Temperature-Measurements-on.

[36] A. Rabhiou, J. Feist, A. Kempf, S. Skinner, and A. Heyes. Phosphorescent thermal history sensors. *Sensors and Actuators A: Physical*, 169:18–26, 9 2011. ISSN 0924-4247. doi: 10.1016/J.SNA.2011.04.022.

[37] H Lösch, A Hirsch, J Holthausen, L Peters, S Neumeier, and N Huittinen. Site-selective fluorescence spectroscopy investigations of lnpo 4 xenotime ceramics for radioactive waste disposal. *Radiochim. Acta*, 13:267–272, 2016.

[38] Mei Yang, Hongpeng You, Yanhua Song, Yeju Huang, Guang Jia, Kai Liu, Yuhua Zheng, Lihui Zhang, and Hongjie Zhang. Synthesis and luminescence properties of sheaflike tbpo4 hierarchical architectures with different phase structures. *Journal of Physical Chemistry C*, 113:20173–20177, 2009. ISSN 19327447. doi: 10.1021/jp908697t.

[39] Marcin Runowski, Andrii Shyichuk, Artur Tymiński, Tomasz Grzyb, Víctor Lavín, and Stefan Lis. Multifunctional optical sensors for nanomanometry and nanothermometry: High-pressure and high-temperature upconversion luminescence of lanthanide-doped phosphates—lapo 4 /ypo 4 :yb 3+ –tm 3+. *ACS Applied Materials & Interfaces*, 10:17269–17279, 5 2018. ISSN 1944-8244. doi: 10.1021/acsami.8b02853. URL https://pubs.acs.org/doi/10.1021/acsami.8b02853.

[40] Marcin Runowski. Pressure and temperature optical sensors: luminescence of lanthanide-doped nanomaterials for contactless nanomanometry and nanothermometry. In *Handbook of Nanomaterials in Analytical Chemistry*, pages 227–273. Elsevier, 2020. ISBN 9780128166994. doi: 10.1016/B978-0-12-816699-4.00010-4. URL http://dx.doi.org/10.1016/B978-0-12-816699-4.00010-4https://linkinghub.elsevier.com/retrieve/pii/B9780128166994000104.

[41] Brian H. Toby. R factors in rietveld analysis: How good is good enough? *Powder Diffraction*, 21:67–70, 2006. ISSN 0885-7156. doi: 10.1154/1.2179804.

[42] Thomas Degen, Mustapha Sadki, Egbert Bron, Uwe König, and Gwilherm Nénert. The high score suite. *Powder Diffraction*, 29:S13–S18, 2014. ISSN 19457413. doi: 10.1017/S0885715614000840.

[43] William A. Bassett. Diamond anvil cell, 50th birthday. *High Pressure Research*, 29: 163–186, 6 2009. ISSN 0895-7959. doi: 10.1080/08957950802597239. URL https://www.tandfonline.com/doi/abs/10.1080/08957950802597239https://www.tandfonline.com/doi/full/10.1080/08957950802597239.

[44] Guoyin Shen, Yanbin Wang, Agnes Dewaele, Christine Wu, Dayne E. Fratanduono, Jon Eggert, Stefan Klotz, Kamil F. Dziubek, Paul Loubeyre, Oleg V. Fat'yanov, Paul D. Asimow, Tsutomu Mashimo, and Renata M.M. Wentzcovitch. Toward an international practical pressure scale: A proposal for an ipps ruby gauge (ipps-ruby2020). *High Pressure Research*, pages 299–314, 2020. ISSN 14772299. doi: 10.1080/08957959.2020.1791107.

[45] Agnès Dewaele, Paul Loubeyre, and Mohamed Mezouar. Equations of state of six metals above 94 gpa. *Physical Review B - Condensed Matter and Materials Physics*, 70:1–8, 2004. ISSN 01631829. doi: 10.1103/PhysRevB.70.094112.

[46] S. Klotz, J-C Chervin, P. Munsch, and G. Le Marchand. Hydrostatic limits of 11 pressure transmitting media. *Journal of Physics D: Applied Physics*, 42:075413, 4 2009. ISSN 0022-3727. doi: 10.1088/0022-3727/42/7/075413. URL https://iopscience.iop.org/article/10.1088/0022-3727/42/7/075413.

[47] Daniel Errandonea, Y. Meng, M. Somayazulu, and D. Häusermann. Pressure-induced $\rightarrow \omega$ transition in titanium metal: A systematic study of the effects of uniaxial stress. *Physica B: Condensed Matter*, 355:116–125, 2005. ISSN 09214526. doi: 10.1016/j.physb.2004.10.030.

[48] Stanislav V. Sinogeikin, Jesse S. Smith, Eric Rod, Chuanlong Lin, Curtis Kenney-Benson, and Guoyin Shen. Online remote control systems for static and dynamic compression and decompression using diamond anvil cells. *Review of Scientific Instruments*, 86, 2015. ISSN 10897623. doi: 10.1063/1.4926892.

[49] Clemens Prescher and Vitali B. Prakapenka. Dioptas: A program for reduction of two-dimensional x-ray diffraction data and data exploration. *High Pressure Research*, 35:223–230, 2015. ISSN 14772299. doi: 10.1080/08957959.2015.1059835.

[50] Armel Le Bail. Whole powder pattern decomposition methods and applications: A retrospection. *Powder diffraction*, 20(4):316–326, 2005.

[51] Eric O. Lebigot. Uncertainties: a python package for calculations with uncertainties. 2018. URL https://uncertainties-python-package.readthedocs.io.

[52] Peter Joel Meschter. Rare earth phosphate bonded ceramics, March 18 2010. US Patent App. 12/232,432.

[53] E. Stavrou, A. Tatsi, E. Salpea, Y. C. Boulmetis, A. G. Kontos, Y. S. Raptis, and C. Raptis. Raman study of zircon-structured rpo4 (r = y, tb, er, tm) phosphates at high pressures. *Journal of Physics: Conference Series*, 121, 2008. ISSN 17426596. doi: 10.1088/1742-6596/121/4/042016.

[54] Karina M Heffernan, Nancy L. Ross, Elinor C. Spencer, and Lynn A. Boatner. The structural response of gadolinium phosphate to pressure. *Journal of Solid State Chemistry*, 241:180–186, 9 2016. ISSN 00224596. doi: 10.1016/j.jssc.2016.06.009. URL https://linkinghub.elsevier.com/retrieve/pii/S0022459616302365.

[55] Rostislav Hrubiak, Stanislav Sinogeikin, Eric Rod, and Guoyin Shen. The laser micro-machining system for diamond anvil cell experiments and general precision machining applications at the high pressure collaborative access team. *Review of Scientific Instruments*, 86, 2015. ISSN 10897623. doi: 10.1063/1.4926889. URL http://dx.doi.org/10.1063/1.4926889.

[56] Mark Rivers, Vitali B. Prakapenka, Atsushi Kubo, Clayton Pullins, Christopher M. Holl, and Steven D. Jacobsen. The compres/gsecars gas-loading system for diamond anvil cells at the advanced photon source. *High Pressure Research*, 28:273–292, 2008. ISSN 08957959. doi: 10.1080/08957950802333593.

[57] Francis Birch. The effect of pressure upon the elastic parameters of isotropic solids, according to murnaghan's theory of finite strain. *Journal of Applied Physics*, 9(4): 279–288, 1938.

[58] HK Mao, J-A Xu, and PM Bell. Calibration of the ruby pressure gauge to 800 kbar under quasi-hydrostatic conditions. *Journal of Geophysical Research: Solid Earth*, 91 (B5):4673–4676, 1986.

[59] Javier Gonzalez-Platas, Matteo Alvaro, Fabrizio Nestola, and Ross Angel. Eosfit7-gui: a new graphical user interface for equation of state calculations, analyses and teaching. *Journal of Applied Crystallography*, 49(4):1377–1382, 2016.

[60] Jai Sharma, Matthew Musselman, Bianca Haberl, and Corinne E Packard. Supplemental information: Figs. s1–s7 (additional xrd- and raman-based plots) as well as table s1 (axial compressibilities)., 2021. URL http://link.aps.org/supplemental/10.1103/PhysRevB.103.184105.

[61] W. O. Milligan, D. F. Mullica, G. W. Beall, and L. A. Boatner. The structures of three lanthanide orthophosphates. *Inorganica Chimica Acta*, 70:133–136, 1983. ISSN 00201693. doi: 10.1016/S0020-1693(00)82791-7.

[62] R. J. Hemley, C. S. Zha, A. P. Jephcoat, H. K. Mao, L. W. Finger, and D. E. Cox. X-ray diffraction and equation of state of solid neon to 110 gpa. *Physical Review B*, 39:11820–11827, 1989. ISSN 01631829. doi: 10.1103/PhysRevB.39.11820.

[63] Sverre Froyen and Marvin L. Cohen. Structural properties of nacl and kc1 under pressure. *Journal of Physics C: Solid State Physics*, 19:2623–2632, 1986. ISSN 00223719. doi: 10.1088/0022-3719/19/15/009.

[64] L. W. Finger, R. M. Hazen, G. Zou, H. K. Mao, and P. M. Bell. Structure and compression of crystalline argon and neon at high pressure and room temperature. *Applied Physics Letters*, 39:892–894, 1981. ISSN 00036951. doi: 10.1063/1.92597.

[65] Josiah Willard Gibbs. *Scientific Papers: Thermodynamics*, volume 1. Dover Publications, 1961.

[66] M. Kizilyalli and A. J. E. Welch. Crystal data for lanthanide orthophosphates. *Journal of Applied Crystallography*, 9:413–414, 1976. ISSN 0021-8898. doi: 10.1107/s0021889876011746.

[67] Yasuo Hikichi, Toshio Sasaki, Suguru Suzuki, Kyouhei Murayama, and Masaaki Miyamoto. Thermal reactions of hydrated hexagonal rpo4·nh2o (r=tb or dy, n=0.5 to 1). *Journal of the American Ceramic Society*, 71:C-354–C-355, 1988. ISSN 15512916. doi: 10.1111/j.1151-2916.1988.tb05940.x.

[68] Ariadna Blanca Romero, Piotr M Kowalski, George Beridze, Hartmut Schlenz, and Dirk Bosbach. Performance of dft+ u method for prediction of structural and thermodynamic parameters of monazite-type ceramics. *Journal of computational chemistry*, 35(18):1339–1346, 2014.

[69] Huaiyong Li, Siyuan Zhang, Shihong Zhou, and Xueqiang Cao. Bonding characteristics, thermal expansibility, and compressibility of rxo4 (r = rare earths, x = p, as) within monazite and zircon structures. *Inorganic Chemistry*, 48:4542–4548, 2009. ISSN 00201669. doi: 10.1021/ic900337j.

[70] Taylor M. Wilkinson, Dong Wu, Matthew A. Musselman, Nan Li, Nathan Mara, and Corinne E. Packard. Mechanical behavior of rare-earth orthophosphates near the monazite/xenotime boundary characterized by nanoindentation. *Materials Science and Engineering A*, 691:203–210, 2017. ISSN 09215093. doi: 10.1016/j.msea.2017.03.041. URL http://dx.doi.org/10.1016/j.msea.2017.03.041.

[71] Piotr M. Kowalski and Yan Li. Relationship between the thermodynamic excess properties of mixing and the elastic moduli in the monazite-type ceramics. *Journal of the European Ceramic Society*, 36:2093–2096, 2016. ISSN 1873619X. doi: 10.1016/j.jeurceramsoc.2016.01.051. URL http://dx.doi.org/10.1016/j.jeurceramsoc.2016.01.051.

[72] Morgan A. Cox, Aaron J Cavosie, Michael Poelchau, Thomas Kenkmann, Phil A. Bland, and Katarina Miljković. *Shock deformation microstructures in xenotime from the Spider impact structure, Western Australia*. Geological Society of America, 8 2021. doi: 10.1130/2021.2550(19). URL http://pubs.geoscienceworld.org/gsa/books/book/2312/chapter-pdf/5457532/spe550-19.pdfhttps://pubs.geoscienceworld.org/gsa/books/book/2312/chapter/130209454/Extreme-plastic-deformation-and-subsequent-Pb-losshttps://pubs.geoscienceworld.org/gsa/books/book.

[73] Koichi Momma and Fujio Izumi. Vesta 3 for three-dimensional visualization of crystal, volumetric and morphology data. *Journal of Applied Crystallography*, 44: 1272–1276, 12 2011. ISSN 0021-8898. doi: 10.1107/S0021889811038970. URL http://scripts.iucr.org/cgi-bin/paper?db5098https://journals.iucr.org/j/issues/2011/06/00/db5098/https://scripts.iucr.org/cgi-bin/paper?S0021889811038970.

[74] Daniel Errandonea and Francisco Javier Manjón. Pressure effects on the structural and electronic properties of abx4 scintillating crystals. *Progress in Materials Science*, 53:711–773, 5 2008. ISSN 00796425. doi: 10.1016/j.pmatsci.2008.02.001.

[75] Manickam Minakshi, David R.G. Mitchell, Christian Baur, Johann Chable, Anders J. Barlow, Maximilian Fichtner, Amitava Banerjee, Sudip Chakraborty, and Rajeev Ahuja. Phase evolution in calcium molybdate nanoparticles as a function of synthesis temperature and its electrochemical effect on energy storage. *Nanoscale Advances*, 1: 565–580, 2 2019. ISSN 25160230. doi: 10.1039/C8NA00156A. URL https://pubs.rsc.org/en/content/articlehtml/2019/na/c8na00156ahttps://pubs.rsc.org/en/content/articlelanding/2019/na/c8na00156a.

[76] Brett Jarrod Macey. *The crystal chemistry of MTO4 compounds with the zicron, scheelite, and monazite structure types*. PhD thesis, Virginia Tech, 1995.

[77] O. Tschauner, S. V. Ushakov, A. Navrotsky, and L. A. Boatner. Phase transformations and indications for acoustic mode softening in tb-gd orthophosphate. *Journal of Physics Condensed Matter*, 28, 2016. ISSN 1361648X. doi: 10.1088/0953-8984/28/3/035403.

[78] Uwe Kolitsch and Dan Holtstam. Crystal chemistry of reexo4 compounds (x = p,as, v). ii. review of reexo4 compounds and their stability fields. *European Journal of Mineralogy*, 16:117–126, 2 2004. ISSN 0935-1221. doi: 10.1127/0935-1221/2004/0016-0117. URL http://pubs.geoscienceworld.org/eurjmin/article-pdf/16/1/117/3121628/117.pdfhttp://www.schweizerbart.de/papers/ejm/detail/16/55816/Crystal_chemistry_of_REEXO4_compounds_X__P_As_V_II?af=crossref.

[79] Robert J. Finch. Structure and chemistry of zircon and zircon-group minerals. *Reviews in Mineralogy and Geochemistry*, 53:1–25, 1 2003. ISSN 1529-6466. doi: 10.2113/0530001. URL https://pubs.geoscienceworld.org/rimg/article/53/1/1-25/87465.

[80] Preyoshi P. Bose, R. Mittal, S. L. Chaplot, C. K. Loong, and L. A. Boatner. Inelastic neutron scattering, lattice dynamics, and high-pressure phase stability of zircon-structured lanthanide orthophosphates. *Physical Review B - Condensed Matter and Materials Physics*, 82, 2010. ISSN 10980121. doi: 10.1103/PhysRevB.82.094309.

[81] Jai Sharma, Matthew Musselman, Bianca Haberl, and Corinne E Packard. In situ synchrotron diffraction of pressure-induced phase transition in dypo4 under variable hydrostaticity. *Physical Review B*, 103:184105, 5 2021. ISSN 2469-9950. doi: 10.1103/PhysRevB.103.184105. URL https://link.aps.org/doi/10.1103/PhysRevB.103.184105.

[82] J M Heuser, R I Palomares, J D Bauer, M J Lozano Rodriguez, J Cooper, M Lang, A C Scheinost, H Schlenz, B Winkler, D Bosbach, S Neumeier, and G Deissmann. Journal of the european ceramic society structural characterization of (sm , tb) po 4 solid solutions and pressure- induced phase transitions. *Journal of the European Ceramic Society*, 38:1–12, 2018. ISSN 0955-2219. doi: 10.1016/j.jeurceramsoc.2018.04.030. URL https://doi.org/10.1016/j.jeurceramsoc.2018.04.030.

[83] Tony Huang, Jiann Shing Lee, Jennifer Kung, and Chih Ming Lin. Study of monazite under high pressure. *Solid State Communications*, 150:1845–1850, 10 2010. ISSN 00381098. doi: 10.1016/j.ssc.2010.06.042. URL http://dx.doi.org/10.1016/j.ssc.2010.06.042.

[84] D. Errandonea, O. Gomis, P. Rodriguez-Hernández, A. Munz, J. Ruiz-Fuertes, M. Gupta, S. N. Achary, A. Hirsch, F. J. Manjon, L. Peters, G. Roth, A. K. Tyagi, and M. Bettinelli. High-pressure structural and vibrational properties of monazite-type bipo4, lapo4, cepo4, and prpo4. *Journal of Physics: Condensed Matter*, 30:065401, 1 2018. ISSN 0953-8984. doi: 10.1088/1361-648X/AAA20D. URL https://iopscience.iop.org/article/10.1088/1361-648X/aaa20dhttps://iopscience.iop.org/article/10.1088/1361-648X/aaa20d/meta.

[85] James R. Rustad. Density functional calculations of the enthalpies of formation of rare-earth orthophosphates. *American Mineralogist*, 97:791–799, 2012. ISSN 19453027. doi: 10.2138/am.2012.3948.

[86] J Ruiz-Fuertes, A Hirsch, A Friedrich, B Winkler, L Bayarjargal, W Morgenroth, L Peters, G Roth, and V Milman. High-pressure phase of lapo 4 studied by x-ray diffraction and second harmonic generation. *Physical Review B*, 94(13):134109, 2016.

[87] Orson L. Anderson, Donald G. Isaak, and Shigeru Yamamoto. Anharmonicity and the equation of state for gold. *Journal of Applied Physics*, 65:1534–1543, 1989. ISSN 00218979. doi: 10.1063/1.342969.

[88] J J Couderc, G Garigue, L Lafourcade, and Q T Nguyen. Standard x-ray diffraction powder patterns. *Zeitschrift für Metallkunde*, 50:708–716, 1959.

[89] A. P. Jephcoat, R. J. Hemley, and H. K. Mao. X-ray diffraction of ruby (al2o3:cr3+) to 175 gpa. *Physica B+C*, 150:115–121, 5 1988. ISSN 0378-4363. doi: 10.1016/0378-4363(88)90112-X.

[90] Alka B. Garg, K. V. Shanavas, B. N. Wani, and Surinder M. Sharma. Phase transition and possible metallization in cevo4 under pressure. *Journal of Solid State Chemistry*, 203:273–280, 7 2013. ISSN 0022-4596. doi: 10.1016/J.JSSC.2013.04.036.

[91] A. M. Seydoux-Guillaume, T. de Resseguier, G. Montagnac, S. Reynaud, H. Leroux, B. Reynard, and A. J. Cavosie. Bridging the shocked monazite gap – Deformation microstructures in natural and laser shock-loaded samples. *Earth Planet. Sci. Lett.*, 595:117727, 2022. ISSN 0012821X. doi: 10.1016/j.epsl.2022.117727. URL https://doi.org/10.1016/j.epsl.2022.117727.

[92] Timmons M. Erickson, Nicholas E. Timms, Mark A. Pearce, Cyril Cayron, Alex Deutsch, Lindsay P. Keller, and David A. Kring. Shock-produced high-pressure (la, ce, th)po4 polymorph revealed by microstructural phase heritage of monazite. *Geology*, 47:504–508, 2019. ISSN 19432682. doi: 10.1130/G46008.1.

[93] Jai Sharma, Henry Q. Afful, and Corinne E. Packard. Phase transformation pathway of dypo4 to 21.5 gpa. *Crystals 2023, Vol. 13, Page 249*, 13:249, 2 2023. ISSN 2073-4352. doi: 10.3390/CRYST13020249. URL https://www.mdpi.com/2073-4352/13/2/249/htmhttps://www.mdpi.com/2073-4352/13/2/249.

[94] Ilya Uts, Konstantin Glazyrin, and Kanani K.M. Lee. Effect of laser annealing of pressure gradients in a diamond-anvil cell using common solid pressure media. *Review of Scientific Instruments*, 84:103904, 10 2013. ISSN 0034-6748. doi: 10.1063/1.4821620. URL https://aip.scitation.org/doi/abs/10.1063/1.4821620.

[95] Agnès Dewaele, Frédéric Datchi, Paul Loubeyre, and Mohamed Mezouar. High pressure-high temperature equations of state of neon and diamond. *Physical Review B - Condensed Matter and Materials Physics*, 77:1–9, 2008. ISSN 10980121. doi: 10.1103/PhysRevB.77.094106.

[96] A. Dewaele, A. B. Belonoshko, G. Garbarino, F. Occelli, P. Bouvier, M. Hanfland, and M. Mezouar. High-pressure-high-temperature equation of state of kcl and kbr. *Physical Review B - Condensed Matter and Materials Physics*, 85:1–7, 2012. ISSN 10980121. doi: 10.1103/PhysRevB.85.214105.

[97] Henry Lösch, Antje Hirsch, Jacqueline Holthausen, Lars Peters, Bin Xiao, Stefan Neumeier, Moritz Schmidt, and Nina Huittinen. A Spectroscopic Investigation of Eu3+ Incorporation in LnPO4 (Ln = Tb, Gd1-xLux, X = 0.3, 0.5, 0.7, 1) Ceramics. *Front. Chem.*, 7(FEB):94, feb 2019. ISSN 2296-2646. doi: 10.3389/fchem.2019.00094. URL https://www.frontiersin.org/article/10.3389/fchem.2019.00094/full.

[98] Yaqi Ji, Piotr M. Kowalski, Philip Kegler, Nina Huittinen, Nigel A. Marks, Victor L. Vinograd, Yulia Arinicheva, Stefan Neumeier, and Dirk Bosbach. Rare-Earth Orthophosphates From Atomistic Simulations. *Front. Chem.*, 7(APR):436276, apr 2019. ISSN 2296-2646. doi: 10.3389/fchem.2019.00197. URL https://www.frontiersin.org/article/10.3389/fchem.2019.00197/full.

[99] Christopher J. Van Hoozen, Alexander P. Gysi, and Daniel E. Harlov. The solubility of monazite (lapo4, prpo4, ndpo4, and eupo4) endmembers in aqueous solutions from 100 to 250c. *Geochimica et Cosmochimica Acta*, 280:302–316, jul 2020. ISSN 0016-7037. doi: 10.1016/J.GCA.2020.04.019.

[100] Junhai Liu, Wenjuan Han, Xiaowen Chen, Degao Zhong, Bing Teng, Chao Wang, and Yuyi Li. Spectroscopic properties and continuous-wave laser operation of yb:lupo4 crystal. *Optics Letters*, 39:5881, 10 2014. ISSN 0146-9592. doi: 10.1364/OL.39.005881. URL http://dx.doi.org/10.1364/OL.39.005881https://www.osapublishing.org/abstract.cfm?URI=ol-39-20-5881.

[101] Justyna Zeler, Eugeniusz Zych, and Joanna Jedoń. Lupo4:yb phosphor with concerted uv and ir thermoluminescent emissions by quantum cutting at high temperatures. *Physical Chemistry Chemical Physics*, 21:23826–23832, 11 2019. ISSN 14639076. doi: 10.1039/c9cp03169c. URL https://pubs.rsc.org/en/content/articlehtml/2019/cp/c9cp03169chttps://pubs.rsc.org/en/content/articlelanding/2019/cp/c9cp03169c.

[102] Lynn A. Boatner, L. A. Keefer, J. M. Farmer, Dariusz Wisniewski, and Andrjez J. Wojtowicz. Cerium-activated rare-earth orthophosphate and double-phosphate scintillators for x- and gamma-ray detection. *Hard X-Ray and Gamma-Ray Detector Physics VI*, 5540:73, 10 2004. ISSN 0277786X. doi: 10.1117/12.562220. URL https://www.spiedigitallibrary.org/terms-of-use.

[103] Pooja Gangwar, Mohnish Pandey, Sri Sivakumar, Raj Ganesh S. Pala, and G. Parthasarathy. Increased loading of Eu3+ ions in monazite LaVO4 nanocrystals via pressure-driven phase transitions. *Crystal Growth and Design*, 13(6):2344–2349, jun 2013. ISSN 15287483. doi: 10.1021/CG3018908/ASSET/IMAGES/LARGE/CG-2012-018908_0008.JPEG. URL https://pubs.acs.org/doi/full/10.1021/cg3018908.

[104] Mansoor Sheik-Bahae and Richard I. Epstein. Laser cooling of solids. *Laser & Photonics Reviews*, 3(1-2):67–84, feb 2009. ISSN 1863-8899. doi: 10.1002/LPOR.200810038. URL https://onlinelibrary.wiley.com/doi/full/10.1002/lpor.200810038https://onlinelibrary.wiley.com/doi/abs/10.1002/lpor.200810038https://onlinelibrary.wiley.com/doi/10.1002/lpor.200810038.

[105] Evan Miyazono, Tian Zhong, Ioana Craiciu, Jonathan M Kindem, and Andrei Faraon. Coupling of erbium dopants to yttrium orthosilicate photonic crystal cavities for on-chip optical quantum memories. *Applied Physics Letters*, 108(1):11111, jan 2016. ISSN 0003-6951. doi: 10.1063/1.4939651. URL http://dx.doi.org/10.1063/1.4939651]https://pubs.aip.org/apl/article/108/1/011111/30725/Coupling-of-erbium-dopants-to-yttrium.

[106] Jonathan M Kindem, John G Bartholomew, Philip J T Woodburn, Tian Zhong, Ioana Craiciu, Rufus L Cone, Charles W Thiel, and Andrei Faraon. Characterization of Yb3+:YVO4 for photonic quantum technologies. *Physical Review B*, 98(2):024404, jul 2018. ISSN 2469-9950. doi: 10.1103/PhysRevB.98.024404. URL https://link.aps.org/doi/10.1103/PhysRevB.98.024404.

[107] C. C. Zhang, Z. M. Zhang, R. C. Dai, Z. P. Wang, J. W. Zhang, and Z. J. Ding. High-pressure raman and luminescence study on the phase transition of gdvo4:eu3+ microcrystals. *Journal of Physical Chemistry C*, 114:18279–18282, 10 2010. doi: 10.1021/JP106063C. URL https://pubs.acs.org/doi/abs/10.1021/jp106063c.

[108] Zhi Zhao, Jian Zuo, and Zejun Ding. Pressure effect on optical properties and structure stability of lapo 4:eu3+ hollow spheres. *Journal of Rare Earths*, 28: 254–257, 2010. ISSN 10020721. doi: 10.1016/S1002-0721(10)60343-2. URL http://dx.doi.org/10.1016/S1002-0721(10)60343-2.

[109] Christoph Lenz, Lutz Nasdala, Dominik Talla, Christoph Hauzenberger, Roland Seitz, and Uwe Kolitsch. Laser-induced ree3+ photoluminescence of selected accessory minerals - an "advantageous artefact" in raman spectroscopy. *Chemical Geology*, 415:1–16, 2015. ISSN 00092541. doi: 10.1016/j.chemgeo.2015.09.001. URL http://dx.doi.org/10.1016/j.chemgeo.2015.09.001.

[110] Margret C Fuchs, Jan Beyer, Sandra Lorenz, Suchinder Sharma, Axel D Renno, Johannes Heitmann, and Richard Gloaguen. A spectral library for laser-induced fluorescence analysis as a tool for rare earth element identification. *Earth System Science Data*, 13(9):4465–4483, sep 2021. ISSN 1866-3516. doi: 10.5194/essd-13-4465-2021. URL https://doi.org/10.5194/essd-13-4465-2021https://essd.copernicus.org/articles/13/4465/2021/.

[111] Joo Yeon D. Roh, Matthew D Smith, Matthew J Crane, Daniel Biner, Tyler J Milstein, Karl W Krämer, and Daniel R Gamelin. Yb3+ speciation and energy-transfer dynamics in quantum-cutting Yb3+-doped CsPbCl3 perovskite nanocrystals and single crystals. *Physical Review Materials*, 4(10):105405, oct 2020. ISSN 2475-9953. doi: 10.1103/PhysRevMaterials.4.105405. URL https://link.aps.org/doi/10.1103/PhysRevMaterials.4.105405.

[112] Szymon Goderski, Marcin Runowski, Przemysław Woźny, Víctor Lavín, and Stefan Lis. Lanthanide upconverted luminescence for simultaneous contactless optical thermometry and manometry-sensing under extreme conditions of pressure and temperature. *ACS Applied Materials and Interfaces*, 12:40475–40485, 2020. ISSN 19448252. doi: 10.1021/acsami.0c09882.

APPENDIX A

COPYRIGHT PERMISSIONS

Permission to include previously published materials in this dissertation is shown below.

Parts of Figure 1.1 are reprinted from Julia M. Heuser, Stefan Neumeier, Lars Peters, Hartmut Schlenz, Dirk Bosbach, and Guido Deissmann. Structural characterisation of metastable tb- and dy-monazites. *Journal of Solid State Chemistry*, 273:45–52, (2019), and permission from the publisher is shown in the supplemental file J-SSC-Heuser.pdf.

Figure 1.2 is reprinted from R. S. Hay, E. E. Boakye, P. Mogilevsky, G. E. Fair, T. A. Parthasarathy, and J. E. Davis. Transformation plasticity in (gdx dy1-x) po 4 fiber coatings during fiber pushout. *Journal of the American Ceramic Society*, 96:1586–1595, (2013), and permission from the publisher is shown in the supplemental file J-ACerS-Hay.pdf.

Figure 1.3 is reprinted from Matthew A. Musselman, Taylor M. Wilkinson, Bianca Haberl, and Corinne E. Packard. In situ raman spectroscopy of pressure-induced phase transformations in polycrystalline tbpo4, dypo4, and gdxdy(1-x)po4. *Journal of the American Ceramic Society*, 101:2562–2570, (2018), and permission from the publisher is shown in the supplemental file J-ACerS-Musselman.pdf.

Figure 1.4 is reprinted from Withnall, R., Silver, J. Physics of Light Emission from Rare-Earth Doped Phosphors. *Handbook of Visual Display Technology.* Springer, Berlin, Heidelberg, (2012), and permission from the publisher is shown in the supplemental file Springer-Withnall.pdf.

Figure 1.6 is reprinted from Marcin Runowski, Andrii Shyichuk, Artur Tyminski, Tomasz Grzyb, Vıctor Lavın, and Stefan Lis. Multifunctional optical sensors for nanomanometry and nanothermometry: High-pressure and high-temperature upconversion luminescence of lanthanide-doped phosphates—lapo4/ypo4:yb3+–tm3+. *ACS Applied Materials & Interfaces*, 10:17269–17279, 5 (2018), and permission from the publisher is shown in the supplemental file ACS-Runowski.pdf.

A.1 Journal Article in Chapter 3

Figure A.1 shows the American Physical Society (APS), on their website (https://journals.aps.org/copyrightFAQ.html), states:

As the author of an APS-published article, may I include my article or a portion of my article in my thesis or dissertation?

Yes, the author has the right to use the article or a portion of the article in a thesis or dissertation without requesting permission from APS, provided the bibliographic citation and the APS copyright credit line are given on the appropriate pages.

Figure A.1 Copy right terms stated on the APS website.

The content in Chapter 3 is reprinted from the article cited below:

Sharma, J., Musselman, M., Haberl, B., and Packard, C. E. (2021). "In situ synchrotron diffraction of pressure-induced phase transition in DyPO4 under variable hydrostaticity." Physical Review B, 103(18), 184105.

The APS copyright credit line is given below:

I have also obtained permission from my non-committee co-authors (Matthew Musselman and Dr. Bianca Haberl) in Figure A.2 and in Figure A.3:

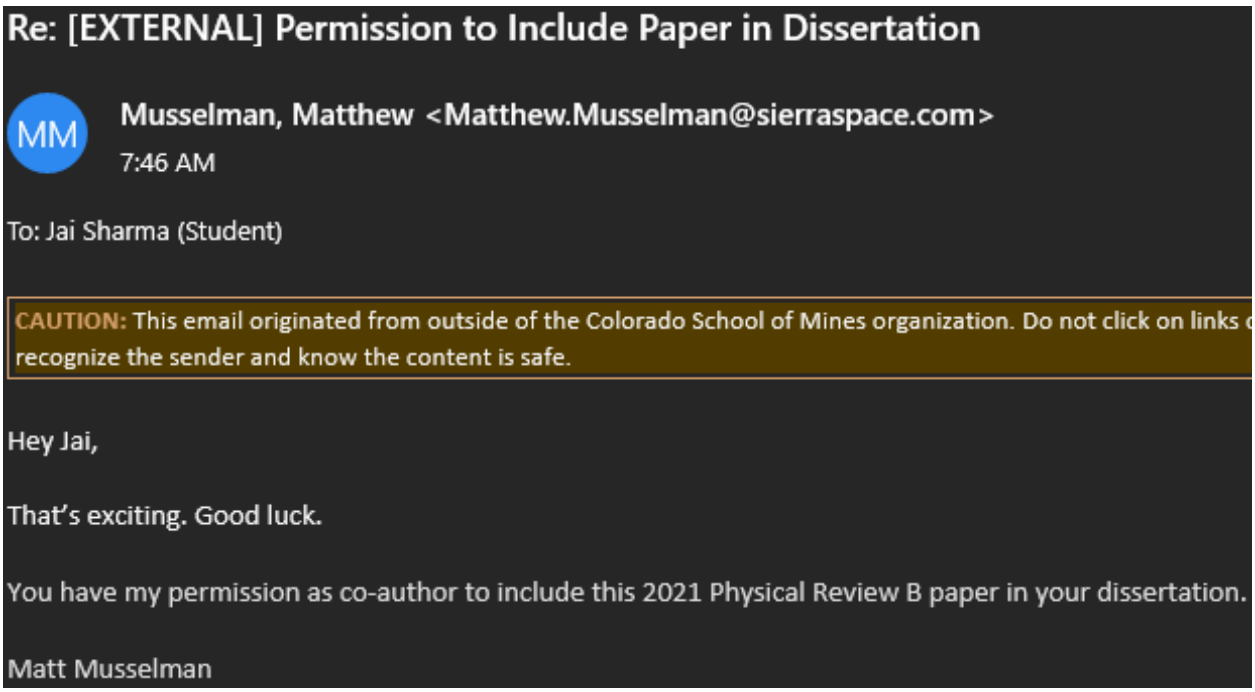

Figure A.2 Copy right permission from Matthew Musselman

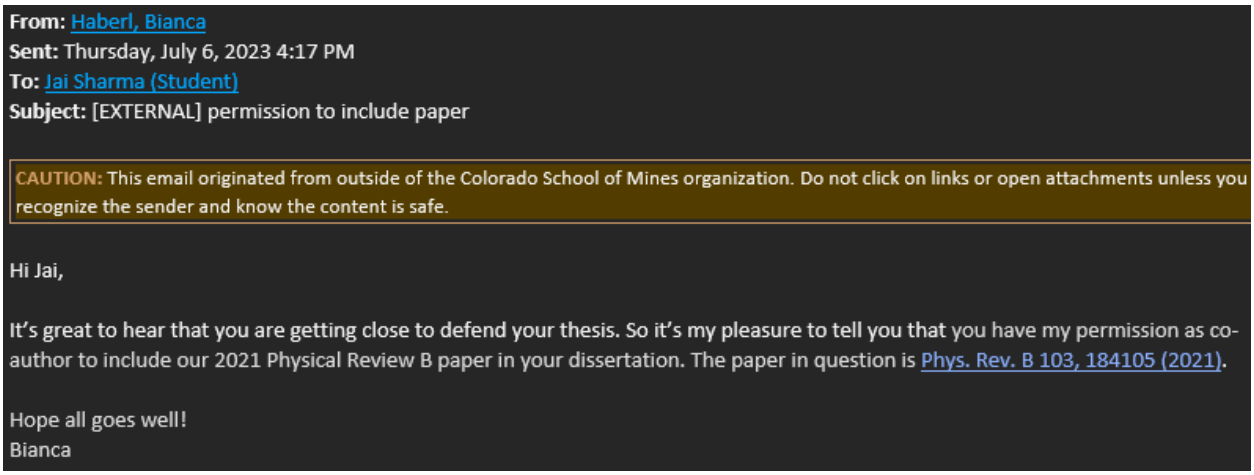

Figure A.3 Copy right permission from Dr. Bianca Haberl

A.2 Journal Article in Chapter 4

On their website (https://www.mdpi.com/authors/rights), MDPI states:

For all articles published in MDPI journals, copyright is retained by the authors. Articles are licensed under an open access Creative Commons CC BY 4.0 license, meaning that anyone may download and read the paper for free. In addition, the article may be reused and quoted provided that the original published version is cited. These conditions allow for maximum use and exposure of the work, while ensuring that the authors receive proper credit.

The content in Chapter 4 is reprinted from the article cited below:

Sharma, J., Afful, H. Q., and Packard, C. E. (2023). Phase Transformation Pathway of DyPO4 to 21.5 GPa. *Crystals*, 13(2), 249.

I have also obtained permission from my non-committee co-author as shown in Figure A.4:

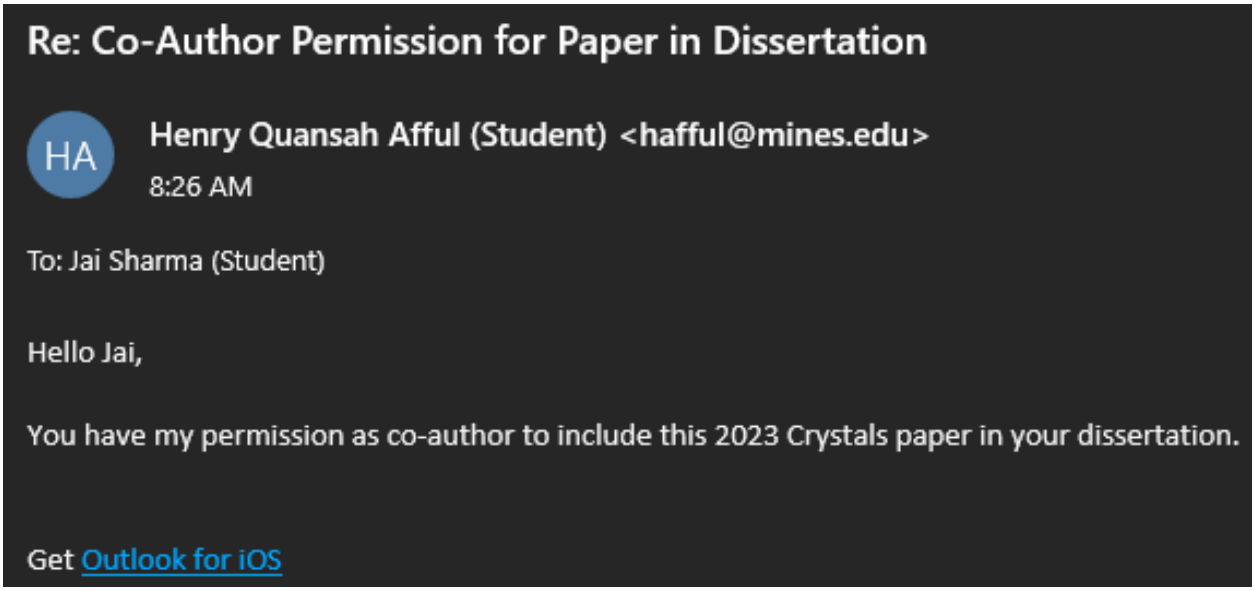

Figure A.4 Copy right permission from Henry Afful

APPENDIX B

PYTHON CODE

Listing B.1: Python code written to process $REPO_4$ lattice parameter data, calculate pressure from the gold lattice parameter, calculate pressure from ruby fluorescence, and extract metrics from PL peaks.

```
import numpy as np
import pandas as pd
import math
import peakutils
from scipy import sparse
from scipy.optimize import *
from scipy.odr import ODR, Model, Data, RealData
from scipy.sparse.linalg import spsolve
from uncertainties import unumpy, umath, ufloat
from lmfit.models import LinearModel, GaussianModel, LorentzianModel,
    PseudoVoigtModel

#This method converts monazite lattice parameters from the P21/c cell
    setting to the P21/n cell setting and calculates lattice parameter
    ratios. Data is read from a pandas dataframe (generated by reading a
     csv output file from HighScore Plus), and processed data is
    inserted into new columns in the same dataframe. 'sd' refers to
    estimated standard deviation, which is also output by HighScore Plus
    . The uncertainties package is used to propagate error in these
    calculations.

def processLatticeParameters(df):
    #Xenotime parameters
        temparray = unumpy.uarray(df['X a'],df['X asd'])**2*unumpy.
            uarray(df['X c'],df['X csd'])
    df.insert(1,'X vol',unumpy.nominal_values(temparray))
    df.insert(1,'X volsd',unumpy.std_devs(temparray))
        temparray = unumpy.uarray(df['X c'],df['X csd'])/unumpy.uarray(
            df['X a'],df['X asd'])# X c/a ratio
    df.insert(1,'X c/a',unumpy.nominal_values(temparray))
    df.insert(1,'X c/asd',unumpy.std_devs(temparray))
    #Monazite parameters
        temparray = unumpy.uarray(df['M a'],df['M asd'])*unumpy.uarray(
            df['M b'],df['M bsd'])*unumpy.uarray(df['M c'],df['M csd'])*
```

```
            unumpy.sin(unumpy.uarray(df['M beta'],df['M betasd'])*math.
            pi/180)
        df.insert(1,'M vol',unumpy.nominal_values(temparray))# calculate M
            volume
        df.insert(1,'M volsd',unumpy.std_devs(temparray))
        c2n = np.linalg.inv(np.array([[1,0,0],[0,-1,0],[-1,0,-1]]))
        for i in range(0,df.shape[0]): #each row
            a, b, c, beta = unumpy.uarray(df['M a'][i],df['M asd'][i]),
                unumpy.uarray(df['M b'][i],df['M bsd'][i]), unumpy.uarray(df
                ['M c'][i],df['M csd'][i]), unumpy.uarray(df['M beta'][i],df
                ['M betasd'][i])
            orig = [[a*a,0,a*c*umath.cos(beta*math.pi/180)],[0,b*b,0],[a*c*
                umath.cos(beta*math.pi/180),0,c*c]]#g matrix of P21/c cell
                setting
            new = np.matmul(np.matmul(c2n,orig),np.transpose(c2n))#g matrix
                 of P21/n cell setting
            a, b, c, beta = umath.sqrt(new[0][0]), umath.sqrt(new[1][1]),
                umath.sqrt(new[2][2]), umath.acos(new[0][2]/(umath.sqrt(new
                [0][0])*umath.sqrt(new[2][2])))*180/math.pi
            df['M a'][i], df['M asd'][i] = unumpy.nominal_values(a), unumpy
                .std_devs(a)
            df['M b'][i], df['M bsd'][i] = unumpy.nominal_values(b), unumpy
                .std_devs(b)
            df['M c'][i], df['M csd'][i] = unumpy.nominal_values(c), unumpy
                .std_devs(c)
            df['M beta'][i], df['M betasd'][i] = unumpy.nominal_values(beta
                ), unumpy.std_devs(beta)
        temparray = unumpy.uarray(df['M c'],df['M csd'])/unumpy.uarray(df['
            M a'],df['M asd'])# M c/a ratio
        df.insert(1,'M c/a',unumpy.nominal_values(temparray))
        df.insert(1,'M c/asd',unumpy.std_devs(temparray))
        temparray = unumpy.uarray(df['M b'],df['M bsd'])/unumpy.uarray(df['
            M a'],df['M asd'])# M c/a ratio
        df.insert(1,'M b/a',unumpy.nominal_values(temparray))
        df.insert(1,'M b/asd',unumpy.std_devs(temparray))
        temparray = unumpy.uarray(df['M c'],df['M csd'])/unumpy.uarray(df['
            M b'],df['M bsd'])# M c/b ratio
        df.insert(1,'M c/b',unumpy.nominal_values(temparray))
        df.insert(1,'M c/bsd',unumpy.std_devs(temparray))

#This method uses the gold Birch-Murnaghan EOS to calculate pressure
    from the gold lattice parameter
def PfromAu(df):
        temp=unumpy.uarray(df['Au a'],df['Au asd'])
        k=unumpy.uarray(167,11)#bulk modulus
        kp=unumpy.uarray(5.5,0.8)#pressure derivative of bulk modulus
            a0=4.0786#gold lattice parameter at 0 GPa
```

```
    temparray = 1.5*k*((4.0786/temp)**7-(4.0786/temp)**5)*(1+0.75*(kp
        -4)*((4.0786/temp)**2-1))
    df.insert(1,'P',unumpy.nominal_values(temparray))
    df.insert(1,'Psd',unumpy.std_devs(temparray))

#This method uses the ruby EOS to calculate pressure from the
    wavelength of the ruby R1 peak
def pruby(lam):
    A,B,lam0 = ufloat(1.87,0.01),ufloat(5.63,0.03),ufloat(694.25,0)
    delta = (lam-lam0)/lam0
    p = A*1000.0*delta*(1.0+B*delta)
    return [round(p.n,1),round(p.s,1)]

#This method fits the ruby spectrum (containing the R1 and R2 peaks) to
    report the center wavelength of the R1 peak. That wavelength is
    then input into the pruby() function to calculate the pressure.
def getP(df):
    bkg = LinearModel()
    r1 = PseudoVoigtModel(prefix='r1_') # taller peak at higher
        wavelength
    r2 = PseudoVoigtModel(prefix='r2_') # shorter peak at lower
        wavelength
    mod = bkg + r1 + r2

    maxloc = df.iloc[:,0][df.iloc[:,1].idxmax()]
    rang = max(df.iloc[:,1]) - min(df.iloc[:,1])

    pars = mod.make_params(
        r1_center=maxloc,
        r1_amplitude=rang,
        r1_sigma=0.25,
        r1_fraction=0.8,

        r2_center=maxloc - 1.5,
        r2_amplitude=rang/1.5,
        r2_sigma=0.25,
        r2_fraction=0.8,

        intercept=min(df.iloc[:,1]),
        slope=(df.iloc[-1,1]-df.iloc[0,1])/(df.iloc[-1,0]-df.iloc[0,0])
    )

    out = mod.fit(df.iloc[:,1],pars,x=df.iloc[:,0])
    out.plot()
    lam = ufloat(out.params['r1_center'].value,out.params['r1_center'].
        stderr)
    print(pruby(lam))
```

```
#This method subtracts a linear baseline from a spectrum.
def bkgSubtract(intensity):
    bkg = peakutils.baseline(intensity)
    return (intensity-bkg)-min(intensity-bkg)

#This method extracts band centroids and maximum intensities from the 4
    bands (defined as ROIs) seen in PL spectra. The input is a PL
   spectrum stored in a dataframe. The peakutils centroid() method
   performs a "center of mass" calculation, which does not require
   fitting bands.
def PLpeakStats(df):
        roi1=slice(25,350)
        roi2=slice(550,900)
        roi3=slice(1000,1275)
        roi4=slice(1350,1700)
    return [peakutils.peak.centroid(df[roi1][0],df[roi1][1]),max(df[
       roi1][1]),
            peakutils.peak.centroid(df[roi2][0],df[roi2][1]),max(df[
               roi2][1]),
            peakutils.peak.centroid(df[roi3][0],df[roi3][1]),max(df[
               roi3][1]),
            peakutils.peak.centroid(df[roi4][0],df[roi4][1]),max(df[
               roi4][1])]
```

APPENDIX C

SUPPLEMENTAL INFORMATION FOR CHAPTER 3

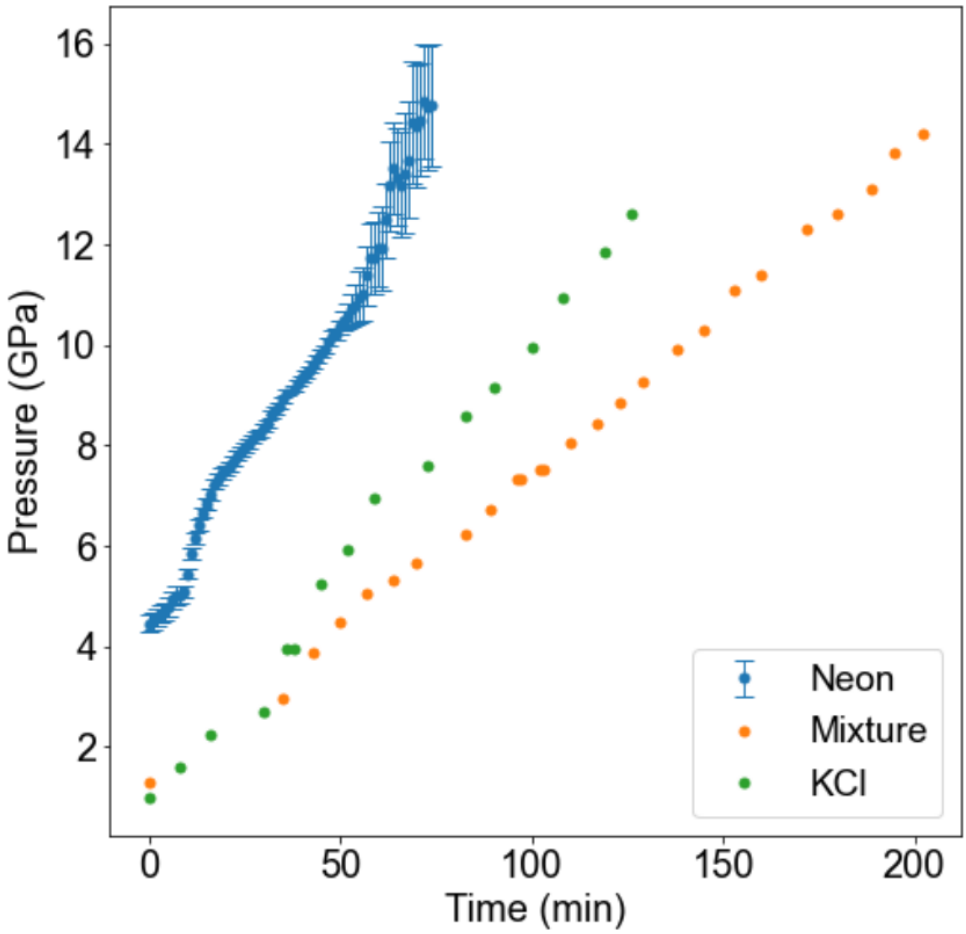

Figure C.1 Loading rates of the three experiments conducted. All rates are of the same order of magnitude. Error bars represent standard deviation. In mixture and KCl datasets, pressure was recorded as a nominal value.

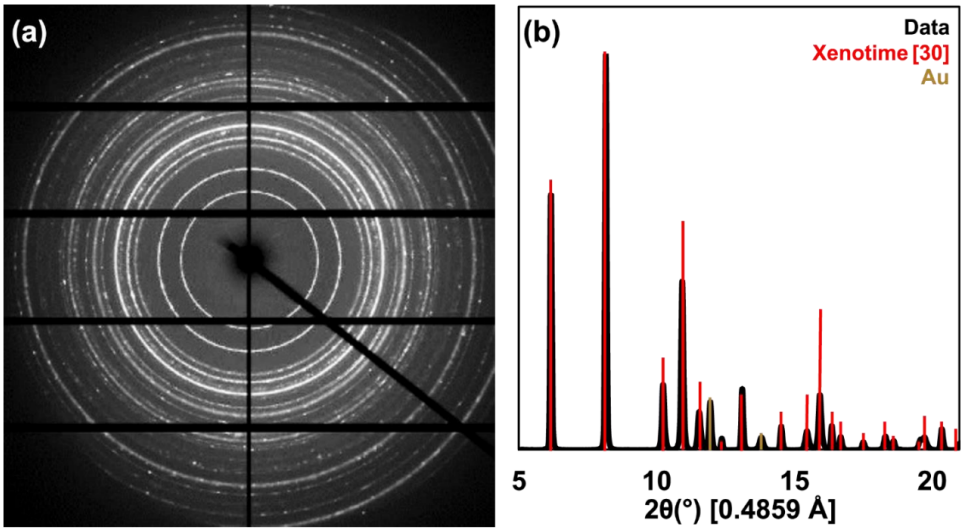

Figure C.2 (a) CCD image of first diffraction pattern from neon experiment. (b) Integrated pattern of CCD image. This 2D diffraction pattern was then calibrated, masked, and integrated using Dioptas [49]. Our data is shown in black and powder patterns of xenotime DyPO4 and Au are shown with red and gold bars, respectively. Observed xenotime peaks clearly do not have the same relative peak intensities as the xenotime powder reference pattern – consistent with preferred orientation in our pattern. This effect is observed in all scans of all experiments and is likely due to the microfocus of the beam (sampling a finite number of grains) rather than any preferred orientation inherent to the polycrystalline sample.

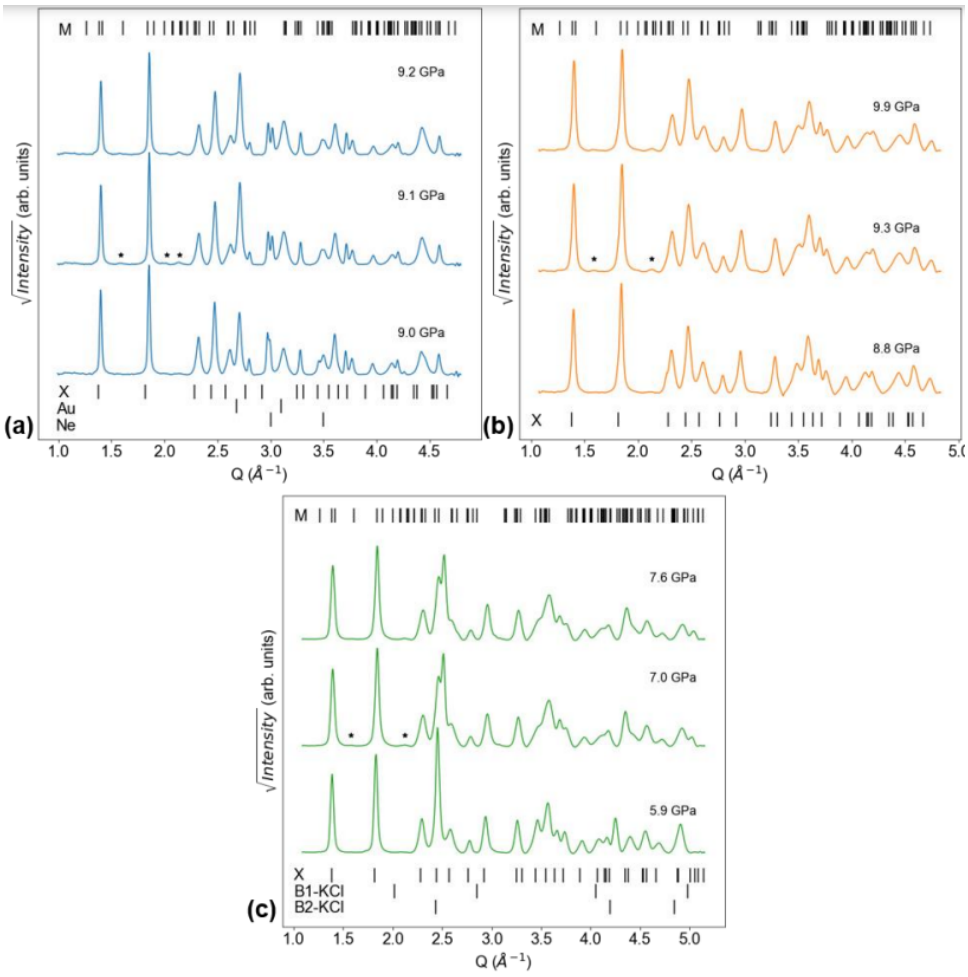

Figure C.3 Raw XRD patterns (before Ponset, at Ponset, and after Ponset) for each of the three PTM experiments. Asterisks mark new monazite peaks that are used to determine Ponset. 'X' ticks show a low-pressure xenotime reference pattern [30], while the 'M' ticks show a monazite pattern. The y-axes are square root of intensity to identify the extremely weak monazite signal at Ponset. (a) Neon experiment. Gold pressure marker and neon PTM peaks are also shown with ticks. (b) Mixture experiment. (c) KCl experiment. The B1 and B2 phases of the KCl PTM are also shown with ticks.

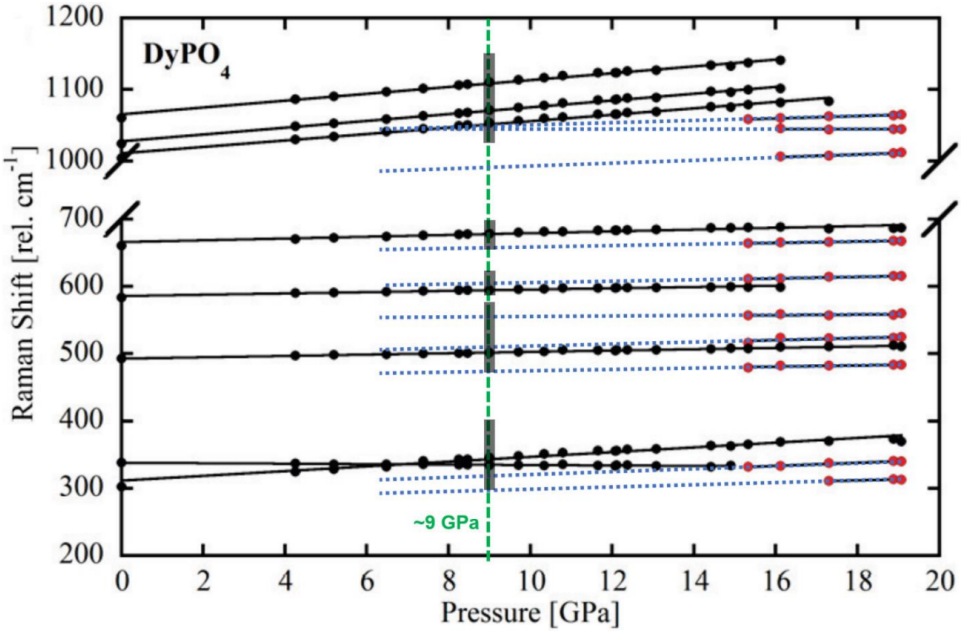

Figure C.4 Raman modes are plotted as a function of pressure during compression. Adapted with permission from Musselman et al. [20]. Initial xenotime phase modes are shown in black and new high-pressure phase modes are shown in red. Black lines represent linear fits for each mode of each phase. Blue, horizontal dotted lines represent extrapolations of the existing monazite mode linear fits. The vertical, green dotted line represents (approximately) the transition pressure determined by XRD in this work. The grey rectangles along this line represent Raman shift (cm-1) ranges of non-zero intensity around the xenotime peaks. Most monazite mode extrapolations fall within the grey rectangles at 9 GPa, suggesting that monazite signal appeared as weak shoulders or tails of stronger xenotime peaks. The poor RS signal-to-noise ratio, however, prevented Musselman et al. from interpreting those weak features as monazite signal.

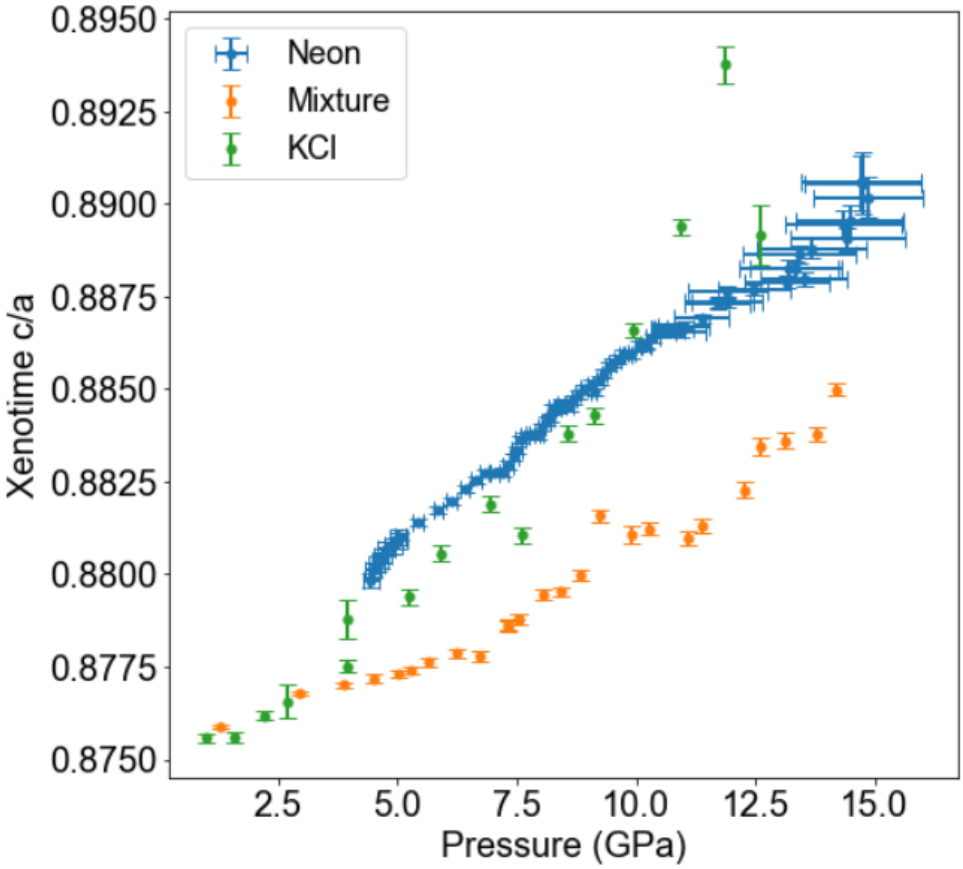

Figure C.5 Xenotime c/a ratio of DyPO4 from the three experiments conducted. Error bars represent standard deviation. In mixture and KCl datasets, pressure was recorded as a nominal value.

Table C.1 Axial compressibility values for each lattice parameter of each phase under each pressure-transmitting medium (PTM). Negative values indicate compression while positive values indicate expansion. Numbers in parentheses after a value represent the standard deviation of the last digit of the value. Monazite fits are poorer than xenotime fits due to XRD signal degradation upon compression.

Lattice Parameter (Å,°)	PTM	Axial Compressibility (Å/GPa) x10^3	Lattice Parameter at 0 GPa (Å,°)	Linear Fit R^2
a_X	Neon	-14.12(18)	6.892(1)	0.997
	Mixture	-13.12(20)	6.911(1)	0.9963
	KCl	-16.16(26)	6.930(1)	0.9943
c_X	Neon	-5.26(7)	6.035(1)	0.9927
	Mixture	-8.35(29)	6.049(1)	0.966
	KCl	-7.64(63)	6.059(2)	0.9246
a_M	Neon	-4.88(34)	6.189(4)	0.9022
	Mixture	-13.60(10)	6.291(12)	0.9606
	KCl	-0.03(40)	6.162(4)	0.0141
b_M	Neon	-5.84(64)	6.680(7)	0.7789
	Mixture	-1.39(30)	6.623(4)	0.6988
	KCl	0.06(7)	6.668(1)	0.0985
c_M	Neon	-9.65(36)	6.471(4)	0.9358
	Mixture	3.22(179)	6.386(20)	0.4851
	KCl	-0.09(8)	6.407(1)	0.0128
β_M	Neon	39.84(380)	99.24(4)	0.7539
	Mixture	75.07(914)	98.76(10)	0.9169
	KCl	-10.64(413)	102.0(0)	0.4127

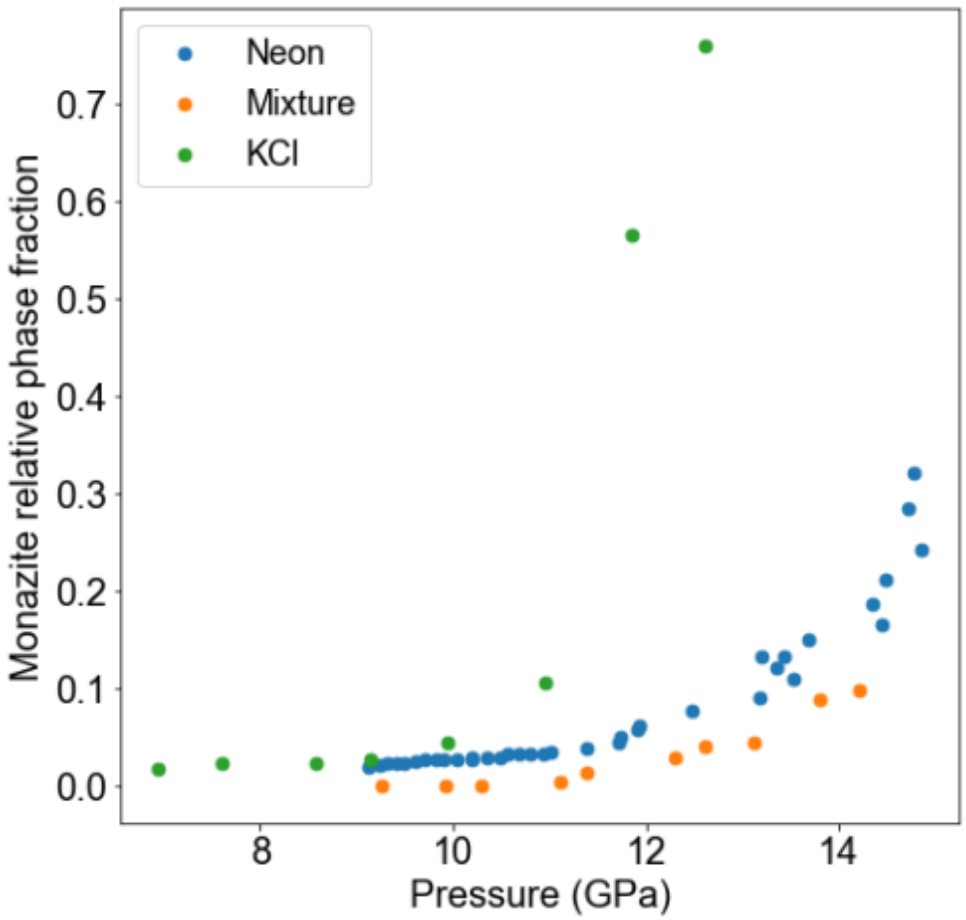

Figure C.6 The relative phase fraction of monazite is plotted against pressure (at P ¿ Ponset) for the three PTMs used. We note that these quantitative values obtained via Rietveld refinement are impacted by significant preferred orientation.

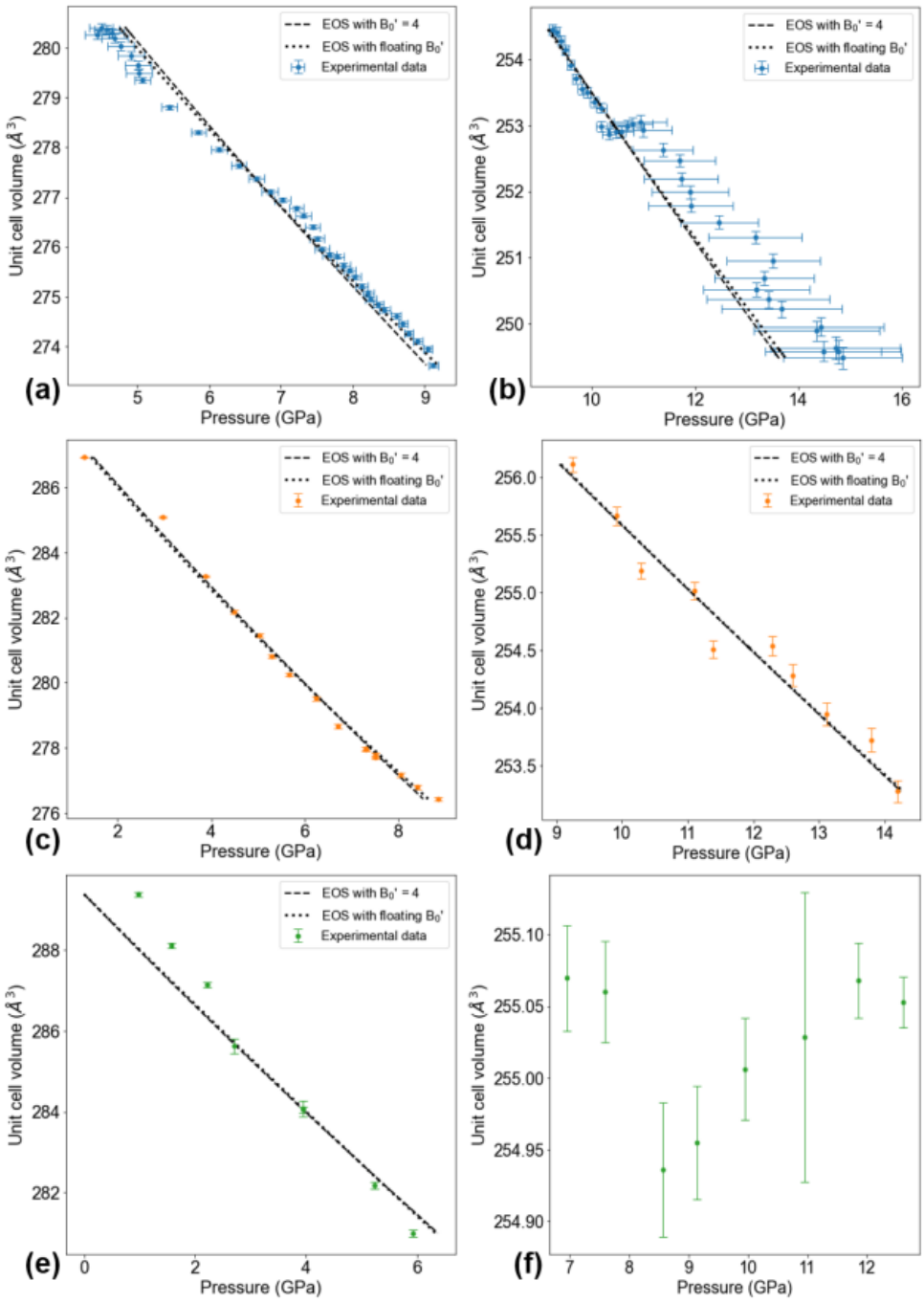

Figure C.7 Plots showing 3rd order Birch-Murnaghan EoS fits to DyPO4 volume vs pressure data.Floating B0' means $2 \leq$ B0' ≤ 7. (a) Xenotime and (b) monazite from neon experiment. (c) Xenotime and (d) monazite from mixture experiment. (e) Xenotime and (f) monazite from KCl experiment. KCl monazite EoS fits did not converge.

APPENDIX D

SUPPLEMENTAL INFORMATION FOR CHAPTER 4

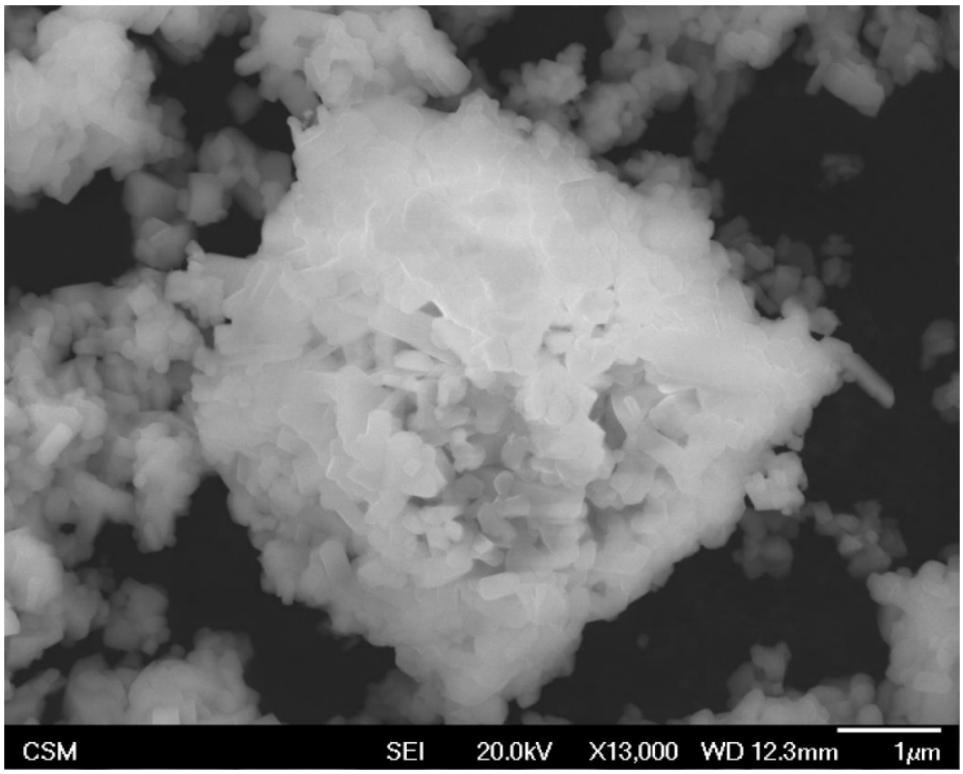

Figure D.1 Scanning electron microscope (SEM) image of the xenotime DyPO4 sample powder. The powder has a sub-micron grain size (100-800 nm). The grains are often clustered into larger particles and exhibit the anisotropic shape expected of tetragonal crystals. This image was obtained using a JEOL 7000F SEM.

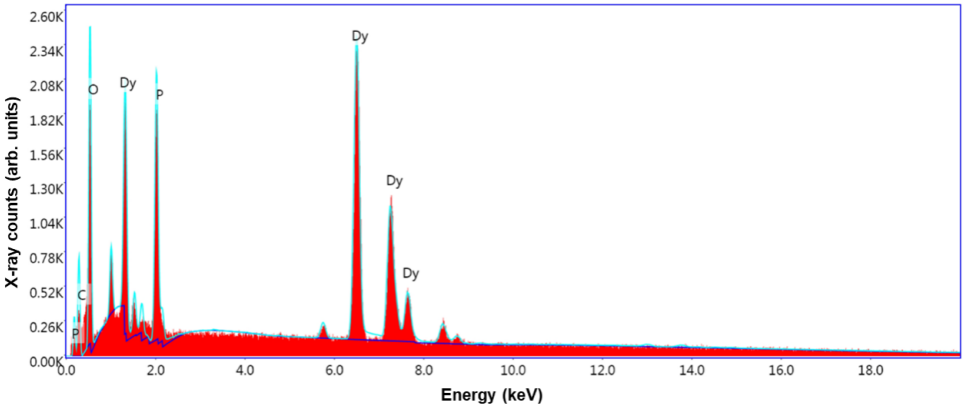

Figure D.2 Energy-dispersive x-ray (EDX) spectrum of the xenotime DyPO4 sample powder. All peaks in the spectrum can be attributed to the elements Dy, P, O, and C. The C signal comes from a deposited carbon coating (to reduce charging) and carbon tape under the sample. This spectrum was obtained using a JEOL 7000F SEM operating at 30.0 kV.

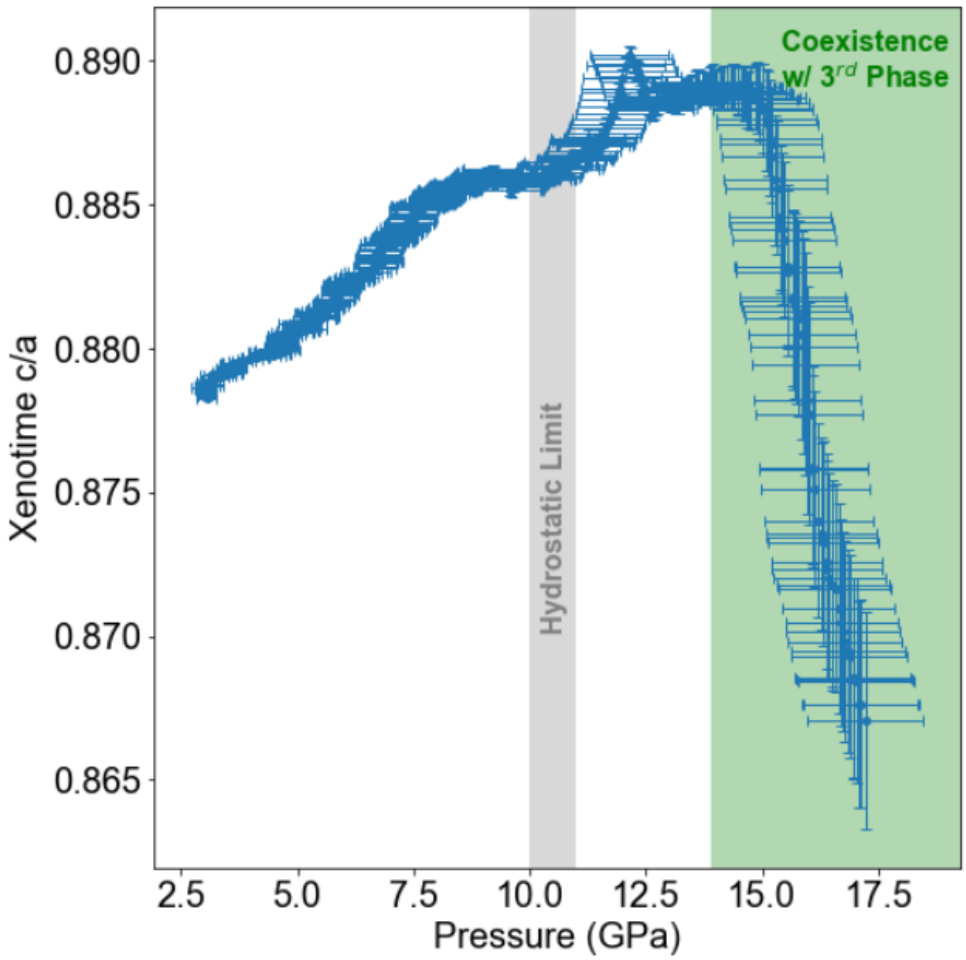

Figure D.3 Pressure dependence of the axial ratio (c_X/a_X) of the xenotime unit cell. The green, shaded area represents the pressure range in which a 3rd (post-monazite) phase of DyPO4 exists. The axial ratio begins a dramatic downturn at ∼14 GPa, coinciding with the emergence of the 3rd (post-monazite) phase of DyPO4.

APPENDIX E

SUPPLEMENTAL INFORMATION FOR CHAPTER 5

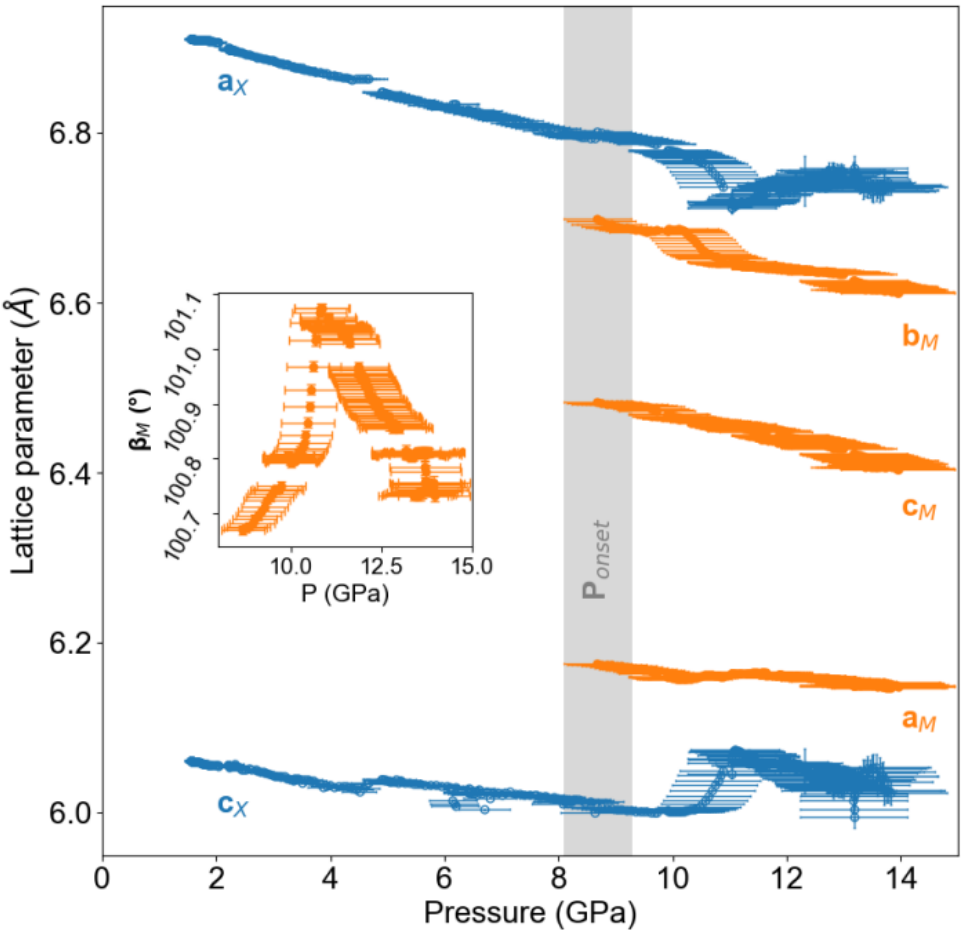

Figure E.1 Pressure dependence of xenotime and monazite lattice parameters from the Tb-neon experiment with standard deviation error bars. The grey rectangle indicates Ponset. The inset shows the monazite beta angle with standard deviation error bars. Lattice parameters shown in blue and orange belong to the xenotime and monazite phases, respectively.

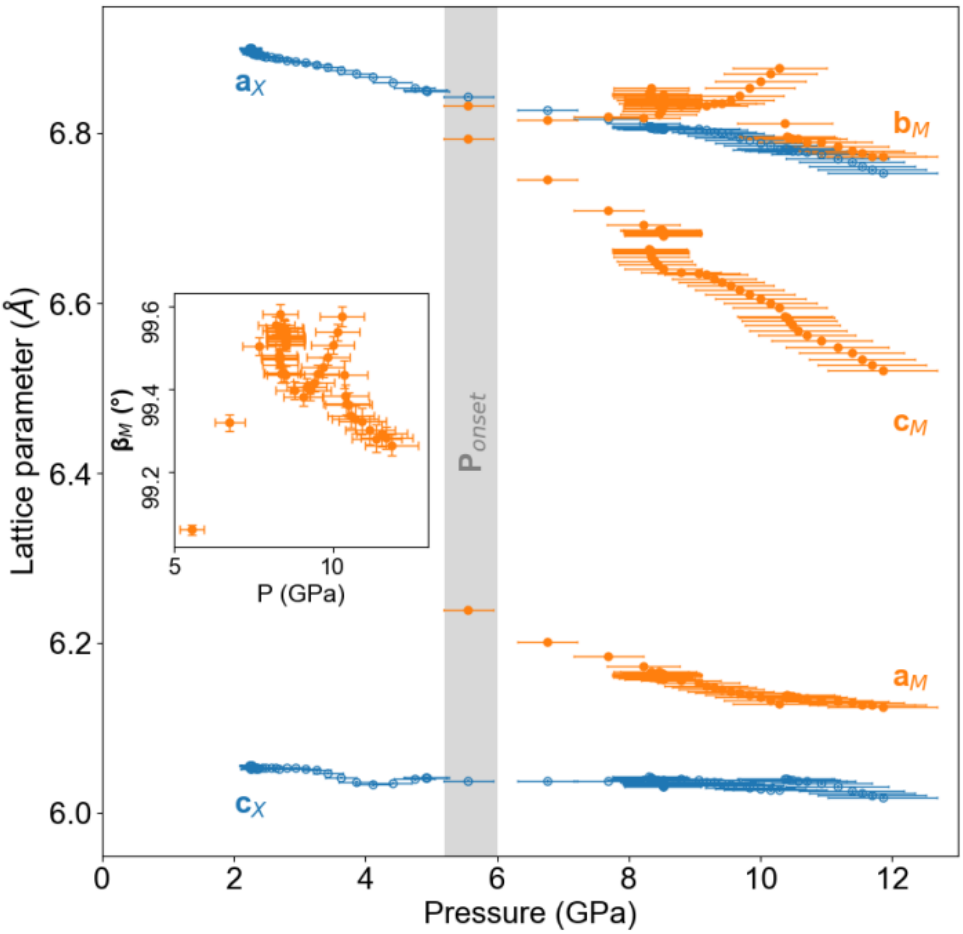

Figure E.2 Pressure dependence of xenotime and monazite lattice parameters from the Tb-KCl experiment with standard deviation error bars. The grey rectangle indicates Ponset. The inset shows the monazite beta angle with standard deviation error bars. Lattice parameters shown in blue and orange belong to the xenotime and monazite phases, respectively.

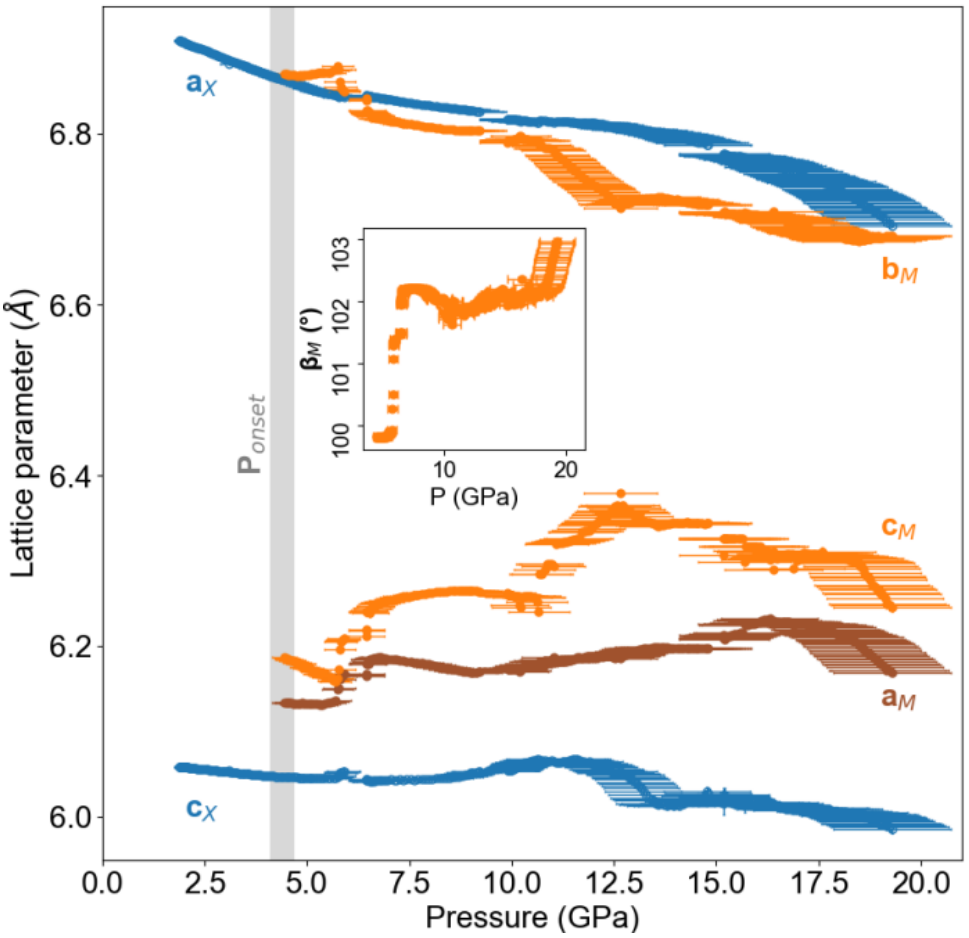

Figure E.3 Pressure dependence of xenotime and monazite lattice parameters from the Tb-none experiment with standard deviation error bars. The grey rectangle indicates Ponset. The inset shows the monazite beta angle with standard deviation error bars. Lattice parameters shown in blue and orange/brown belong to the xenotime and monazite phases, respectively.

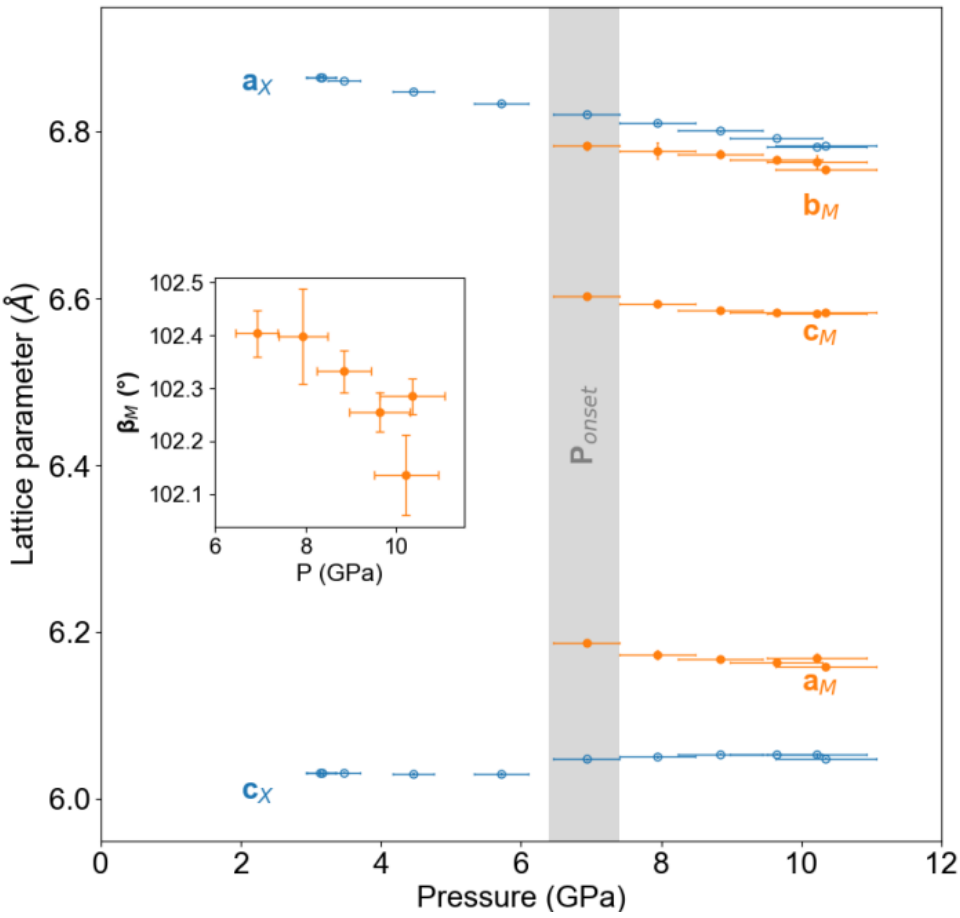

Figure E.4 Pressure dependence of xenotime and monazite lattice parameters from the Dy-none experiment with standard deviation error bars. The grey rectangle indicates Ponset. The inset shows the monazite beta angle with standard deviation error bars. Lattice parameters shown in blue and orange belong to the xenotime and monazite phases, respectively.

Table E.1 Axial compressibility values for each lattice parameter of each phase under each pressure-transmitting medium (PTM) for TbPO4 and DyPO4. Negative values indicate compression while positive values indicate expansion. Numbers in parentheses after a value represent the standard deviation of the last digit of the value. 'X' indicates xenotime, while 'M' indicates monazite. Compressibilities are determined using pressure ranges in which the data is monotonic, making a linear fit suitable. When a linear fit is not suitable or a phase does not have a certain lattice parameter, no compressibility is reported.

RE	Phase	PTM	a	b	c	β
Tb	X	Neon	-16.95(11)	-	-7.06(9)	-
		KCl	-14.30(9)	-	-	-
		None	-17.66(6)	-	-4.44(5)	-
	M	Neon	-13.7(7)	-7.1(12)	-11.6(11)	-
		KCl	-14.7(7)	-	-44.3(16)	-
		None	-	-15.9(2)	-	
Dy	X	Neon	-14.12(18)	-	-5.26(7)	-
		KCl	-16.16(26)	-	-8.35(29)	-
		None	-11.35(11)	-	-3.3(4)	-
	M	Neon	-4.88(34)	-5.84(64)	-9.65(36)	-
		KCl	-0.03(40)	0.06(7)	-0.09(8)	-
		None	-7.7(11)	-5.3(12)	-8.1(13)	-45.8(16)

APPENDIX F

SUPPLEMENTAL INFORMATION FOR CHAPTER 6

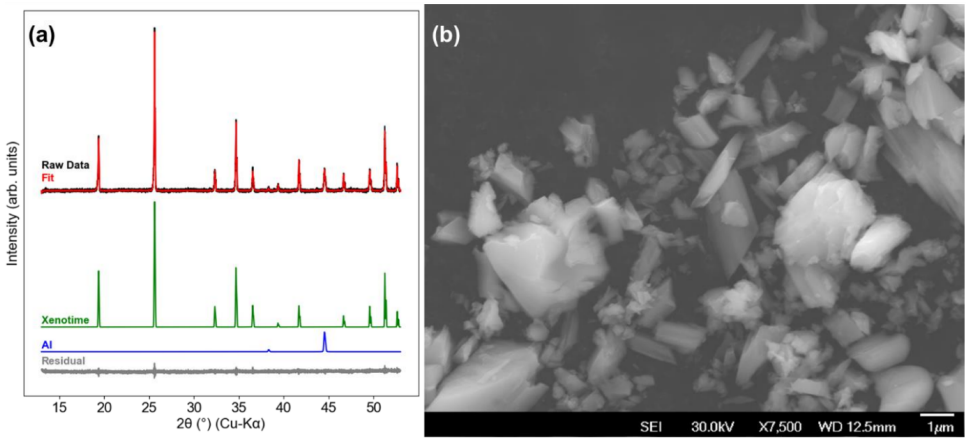

Figure F.1 (a) TbPO4 sample powder XRD pattern obtained using a PANalytical PW3040 diffractometer.(b) Scanning electron microscope (SEM) image showing the expected tetragonal crystal habit of xenotime TbPO4 grains with sizes ranging from sub-micrometer to several micrometers. Rietveld refinement is performed using HighScore Plus. The Al is from the sample holder. The SEM image was obtained using a JEOL 7000F SEM.

Table F.1 Additional details of the DAC experiments. For pressure values followed by a number in parentheses, the number in parentheses represents the standard deviation of the last digit of the pressure.

Experiment	1	2	3	4	5
Almax DAC type (mechanism)	HeliosDAC (membrane)	HeliosDAC (membrane)	HeliosDAC (membrane)	plateDAC (screw)	HeliosDAC (membrane)
P_{max} (GPa)	23.16(10)	22.14(8)	15.45(6)	7.59(3)	8.49(3)
Sample exposure time (s)	12.5	15	14	40	15
Culet diameter (μm)	600	600	600	500	600
Gasket hole thickness (μm)	80	80	80	110	80
Gasket hole diameter (μm)	300	300	300	250	300

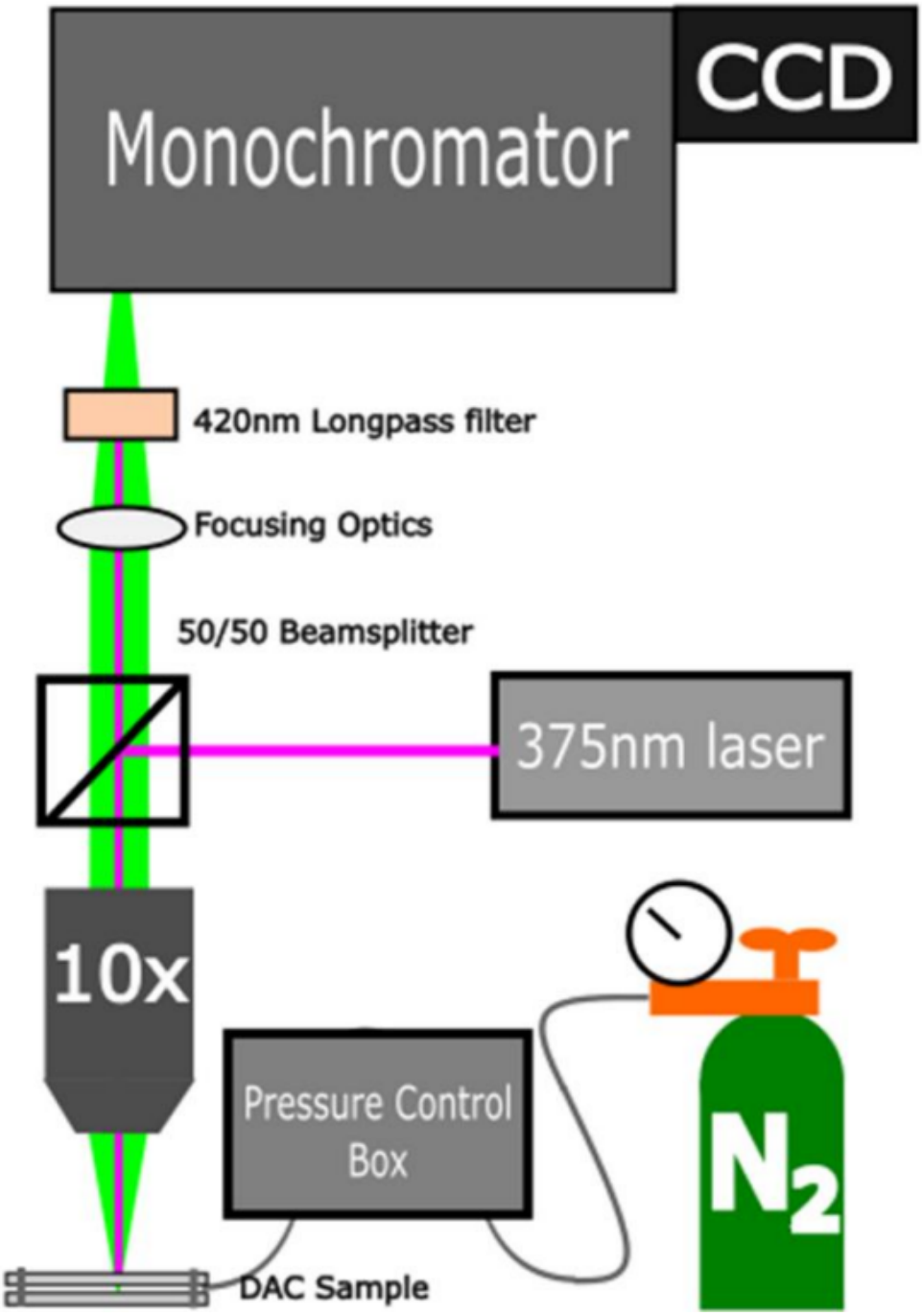

Figure F.2 Photoluminescence setup for excitation of TbPO4 under controllable pressure.

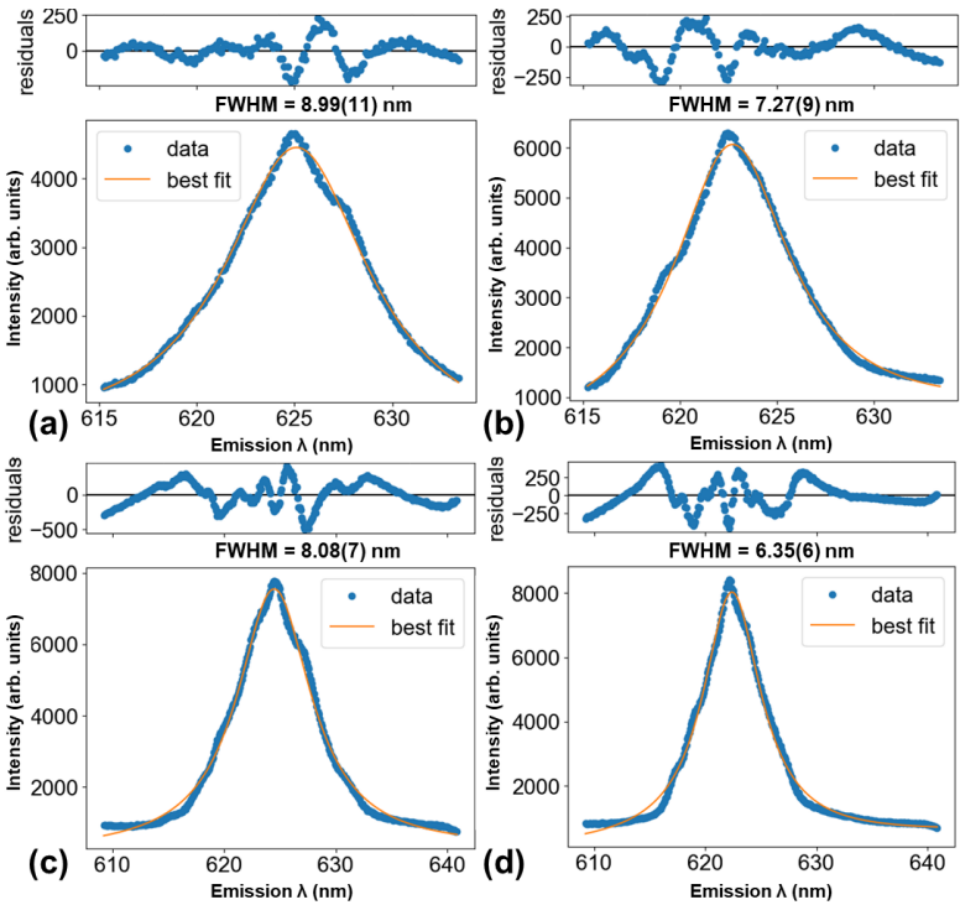

Figure F.3 Lorentzian fits of Band 4. (a) Exp. 1 at Pmax. (b) Exp. 1 after decompression. (c) Exp. 2 at Pmax. (d) Exp. 2 after decompression. For FWHM values, the number in parentheses represents the standard deviation of the last digit of the FWHM.

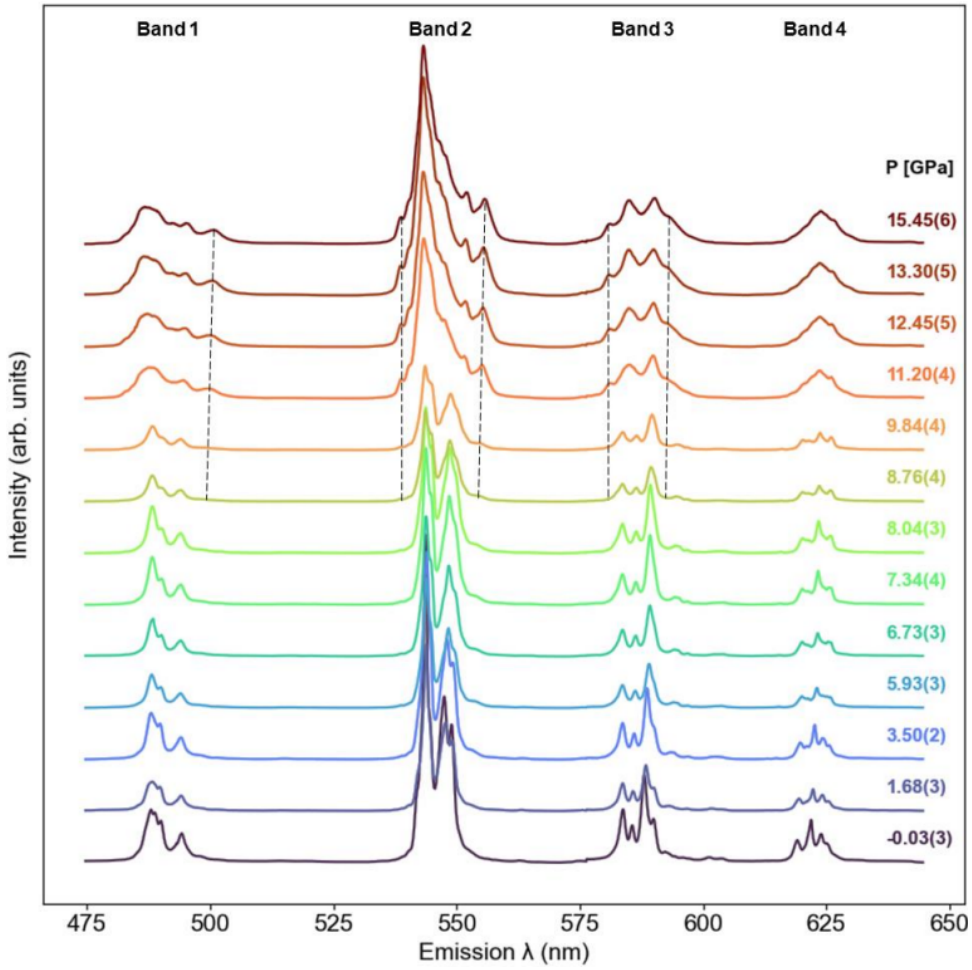

Figure F.4 Pressure evolution of TbPO4 PL spectra from Exp. 3.

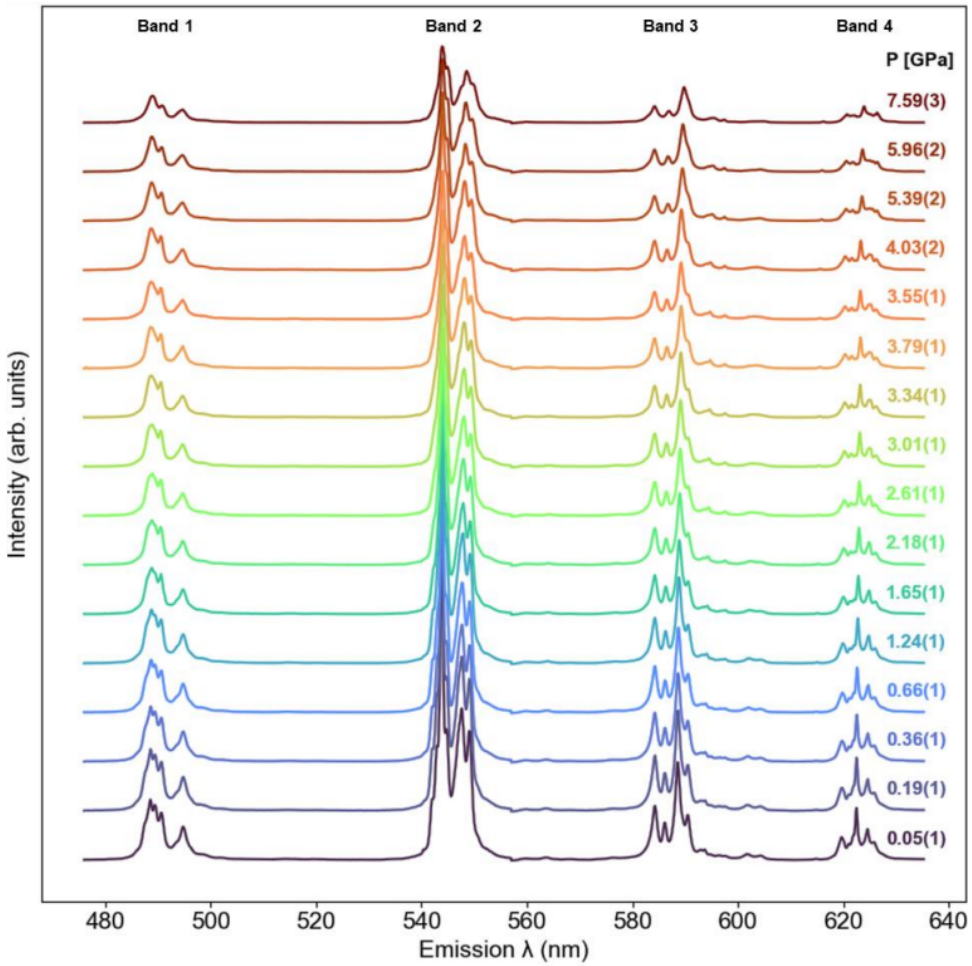

Figure F.5 Pressure evolution of TbPO4 PL spectra from Exp. 4.

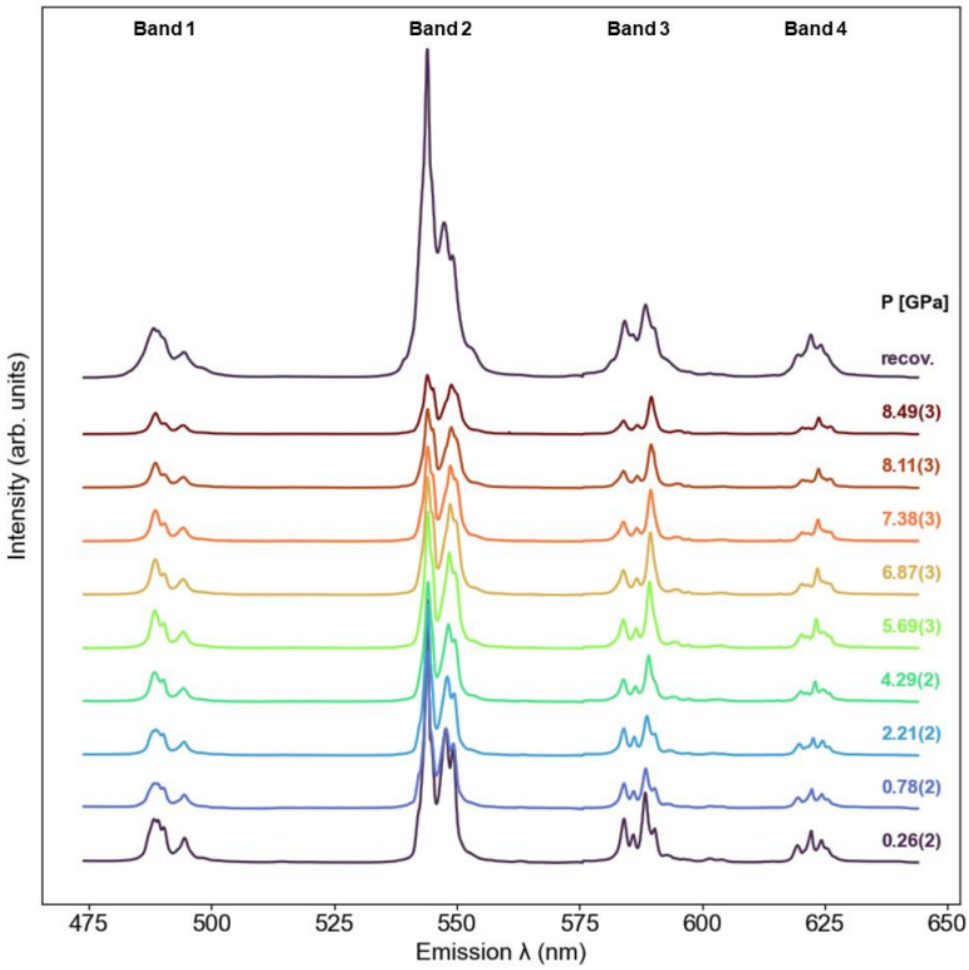

Figure F.6 Pressure evolution of TbPO4 PL spectra from Exp. 5.

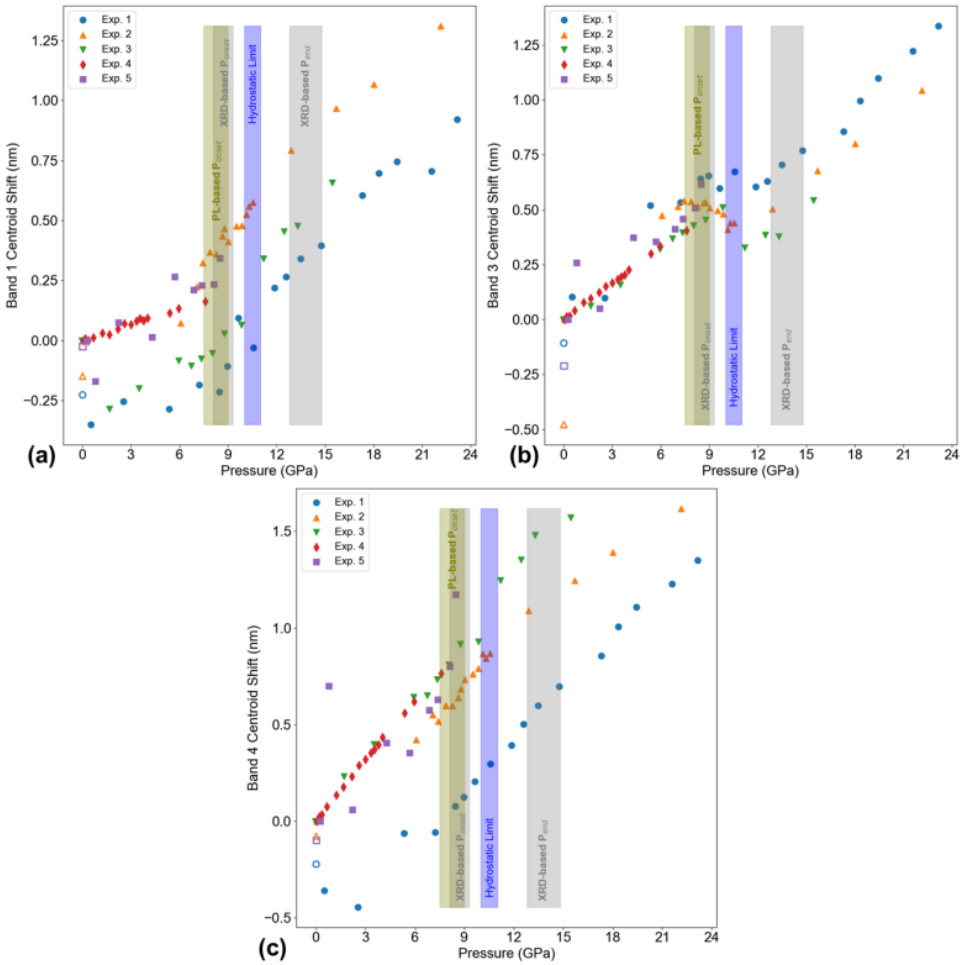

Figure F.7 Pressure evolution of the centroids of (a) Band 1, (b) Band 3, and (c) Band 4. Blue and grey rectangles represent the pressure ranges corresponding to the hydrostatic limit of MEW and the xenotime-monazite phase coexistence range (as reported by Lopez-Solano et al. [18]),respectively. Open symbols represent data from recovered sample at 1 atm. Pressure error bars are within the symbols.

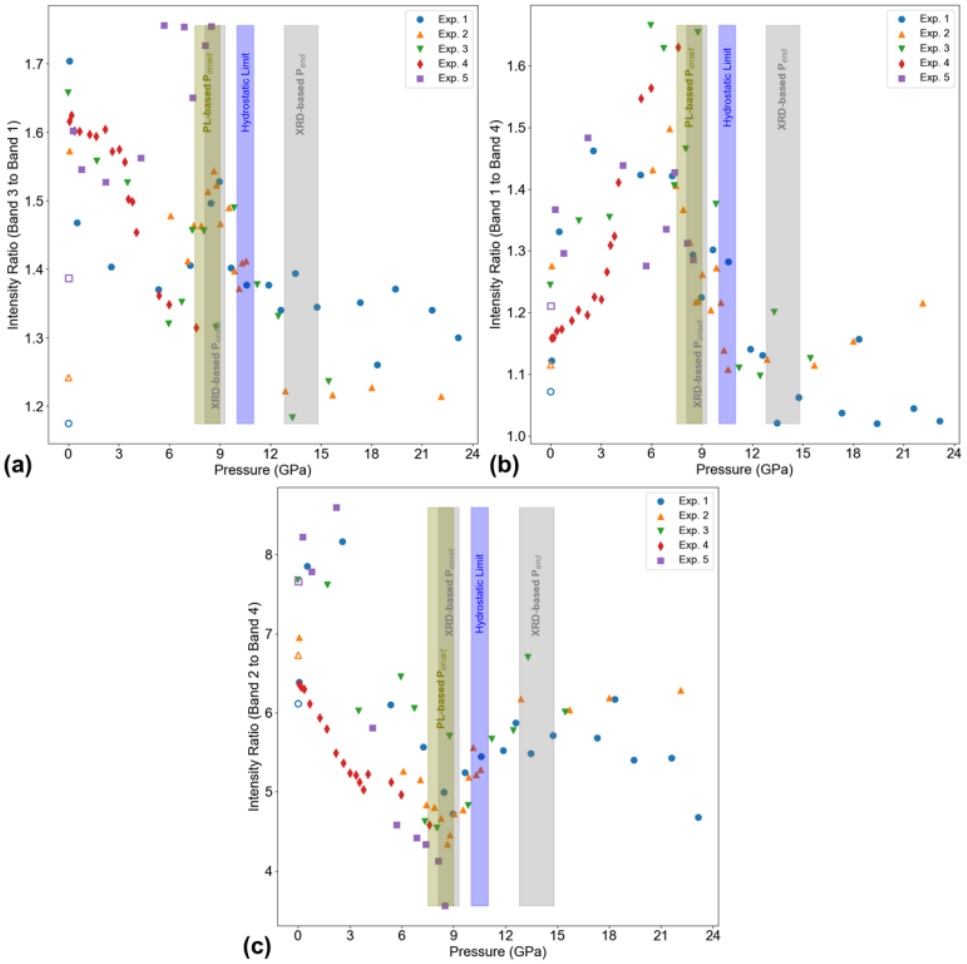

Figure F.8 Pressure evolution of the following BIRs: (a) 3:1, (b) 1:4, and (c) 2:4. Blue and grey rectangles represent the pressure ranges corresponding to the hydrostatic limit of MEW and the xenotime-monazite phase coexistence range (as reported by Lopez-Solano et al. [18]), respectively. Open symbols represent data from recovered sample at 1 atm. Pressure error bars are within the symbols.

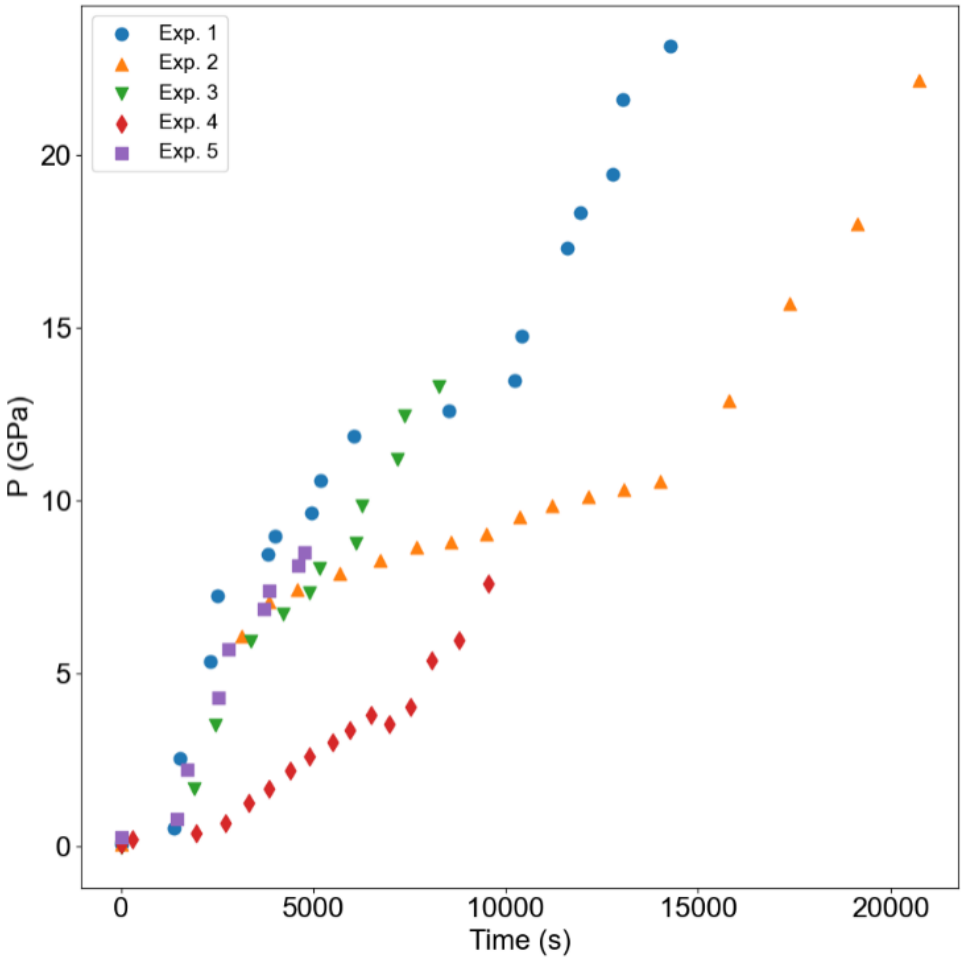

Figure F.9 Pressure vs time from all 5 experiments. Pressure error bars are within the symbols. All loading rates are within one order of magnitude (ranging from ∼0.3 MPa/s to ∼1.5 MPa/s).